Chatter Vibrations in Robotic Milling Considering Structural Nonlinearity

by

Yaser Mohammadi
B.Sc., University of Tabriz, 2015
M.Sc., Sabanci University, 2017

A Dissertation Submitted in Partial Fulfillment of the
Requirements for the Degree of

DOCTOR OF PHILOSOPHY

in the Department of Mechanical Engineering

Chatter Vibrations in Robotic Milling Considering Structural Nonlinearity

by

Yaser Mohammadi
B.Sc., University of Tabriz, 2015
M.Sc., Sabanci University, 2017

Supervisory Committee

Dr. Keivan Ahmadi, Supervisor
(Department of Mechanical Engineering, University of Victoria, Canada)

Dr. Yang Shi, Departmental Member
(Department of Mechanical Engineering, University of Victoria, Canada)

Dr. Panajotis Agathoklis, Outside Member
(Department of Electrical and Computer Engineering, University of Victoria, Canada)

Dr. Tony Schmitz, External Examiner
(Department of Mechanical, Aerospace, and Biomedical Engineering, University of Tennessee, USA)

ABSTRACT

The application of robotic manipulators in machining systems has gained a great interest in manufacturing because of their lower prices, higher kinematic flexibility and larger workspace compared to conventional CNC machine tools. However, their performance is limited due to the much lower structural rigidity which makes them more susceptible to excessive and unstable vibrations, known as chatter, during the machining process. Highly effective chatter modeling and avoidance methods that have been developed for CNC machining in the past decades are now being used by the industry to design high-performance chatter-free machining operations. The available methods, however, face major difficulties when applied to robotic machining, mainly due to the high flexibility and pose-dependency of the vibration response in robots. High flexibility leads to high-amplitude vibrations which affect the process dynamics and excite structural nonlinearities. The existing approaches to modeling machining vibrations assume linearity of the structural dynamics of the robotic manipulator. This assumption, considering the inherent nonlinearities in the robot's revolute joints, may cause considerable inaccuracies in predicting the stability of vibrations during the process.

This thesis studies the high flexibility and nonlinearity of the robot's structural dynamics and their effects on chatter vibrations. The research starts with investigating the effects of high flexibility of robot's structure in the process dyamics by considering the modulation of cutting forces by axial vibrations, which is normally ignored in CNC milling due to high rigidity of the machine in this direction. The results of chatter prediction considering this effect are shown and discussed. The rest of the thesis focuses on the structural nonlinearity. Firstly, an experimental study is presented to investigate the extent of nonlinearity in structural dynamics of the robot. The results confirm that structural nonlinearities in robotic machining systems can be effectively excited in the presence of high-amplitude vibrations due to milling forces, such that they cause remarkable differences in chatter prediction. The following step is modeling the structural nonlinearities. For this purpose, the variation of restoring forces with the dynamic response (displacement and velocity) are observed when the robot is subjected to harmonic excitation. Based on the experimental observations, the nonlinear effects are modeled by cubic stiffness and damping characteristics. Parameters of the nonlinear model are then identified using Higher-order Frequency Response Functions (HFRF) extracted from measurements. The identified model

can predict the vibration behavior of the robotic machining system when subjected to periodic loads such as milling forces. The developed model of nonlinear structural dynamics is then coupled with the chatter model. Consequently, the system is described by nonlinear Delay Differential Equations (DDE) with periodic coefficients. Bifurcation diagrams for the forced vibrations in the described system are developed using the numerical continuation method. The effects of cutting parameters such as feedrate as well as the nonlinear parameters are studied.

The thesis is concluded by proposing the use of in-process FRF in the linear model of chatter stability for quick prediction of stability limits. In this approach, the exact characteristics of the nonlinear mechanisms are not studied; instead, the measured FRF during the milling process are used, which are assumed to represent the nonlinear structural dynamics that are linearized about the applied operational conditions. Two methods of measuring in-process FRF are proposed and employed in the robotic milling system. The measured FRF are then used in the linear chatter model to develop the Stability Lobes Diagram (SLD) which shows the combination of cutting parameters that lead to stable or unstable vibrations. Experimental chatter tests show that better agreement with predictions can be achieved by using in-process FRF instead of FRF measured at the idle state of the system.

The results of this thesis contribute to better characterization of vibrations in robotic machining with high-amplitude forces and selecting suitable strategies to enhance productivity of the operation.

Contents

List of Tables

List of Figures

ACRONYMS

TCP Tool Centre Point

FRF Frequency Response Functions

HFRF Higher-order Frequency Response Functions

SLD Stability Lobes Diagram

LTI Linear Time Invariant

DDE Delay Differential Equations

MBD Multi Body Dynamic

ZOA Zero Order Approximation

MFS Multi Frequency Solution

SDM Semi Discretization Method

FDM Full Discretization Method

OMA Operational Modal Analysis

EMA Experimental Modal Analysis

CCT Conservative Congruence Transformation

SDOF Single Degree of Freedom

MDOF Multi Degrees of Freedom

SISO Single Input Single Output

MIMO Multi Input Multi Output

CNC Computer Numerical Control

ACKNOWLEDGEMENTS

I wish to show my appreciation to everyone who supported me during my Ph.D. studies.

I would like to express my sincere gratitude to my supervisor, Dr. Keivan Ahmadi, for his mentorship throughout these years. Also, many thanks to all my fellow labmates for their help and friendship. Lastly, my special and deepest thanks to my family for their endless support and love.

This research was financially supported by the Natural Sciences and Engineering Research Council of Canada (NSERC) through the Discovery Grant Program.

DEDICATION

To my family

Chapter 1

Thesis Overview

In this chapter, a brief summary of the thesis is provided, including an introduction, the research problem, the methodology, and key findings.

1.1 Introduction

Machining processes (e.g. drilling and milling) of metal or composite materials are traditionally performed using Computer Numerical Control (CNC) machine tools (Fig. 1.1(a)). To meet the tight surface finish and dimensional tolerances required in machined parts, the structure of CNC machine tools is designed to be as stiff as possible in all directions to avoid excessive vibrations or deflections of the cutting tool (e.g. endmill or drill bit). For the past decades, industrial robotic manipulators such as the system shown in Fig. 1.1(b) have been regarded as an alternative to CNC machine tools. As shown in Fig. 1.1(b), a typical machining robot consists of an industrial robotic manipulator with a spindle and a cutting tool (e.g. milling, drilling, or polishing) as the end effector. Robotic manipulators are considerably cheaper than CNC machine tools, provide a much larger workspace, and one robot can perform several tasks in a single setup, which further reduces the production cost. However, the high structural compliance of the robots causes excessive vibrations and deflections. Therefore, the application of robots to perform machining has been limited to low-force operations such as polishing and deburring. In recent years, robots are becoming more and more accurate, owning to advanced control strategies, and the cutting forces become smaller and smaller, owing to the implementation of high-performance machining technologies. Therefore, the application of robots to perform

milling and drilling operations has gained extensive attention in various industries such as aircraft, wind turbines, and automotive manufacturing. This industrial interest has inspired a new field of research with the overarching objective of enhancing the performance of machining robots to conduct tasks that are typically done by CNC machine tools.

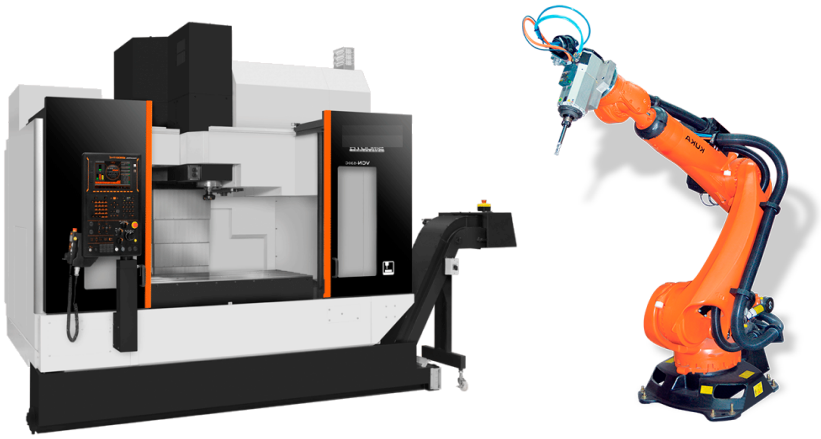

(a) (b)

Figure 1.1: (a) A conventional CNC machine tool [1] and (b) a robotic machining system [2].

1.2 Motivation and Problem statement

There have been many studies focusing on improving robots' performance for machining purposes [11, 12, 13, 14, 15]. Although promising improvements have been reported, there are yet major barriers to overcome in robotic machining operations. The main challenge in the application of industrial robots to perform high-force machining operations is their low rigidity due to the high compliance of their revolute joints [11]. The high structural flexibility makes robotic machining systems highly prone to unstable vibrations during machining processes, known as chatter vibrations, which consequently leads to the poor surface quality (see Fig. 1.2) and, in extreme conditions, critical damages to the machining system. The common solution to avoiding such damages is to use conservative machining parameters (e.g. feedrate and depth of cut), which greatly reduces productivity and defeats the primary purpose of replacing CNC machine tools with industrial robots, i.e. cost saving.

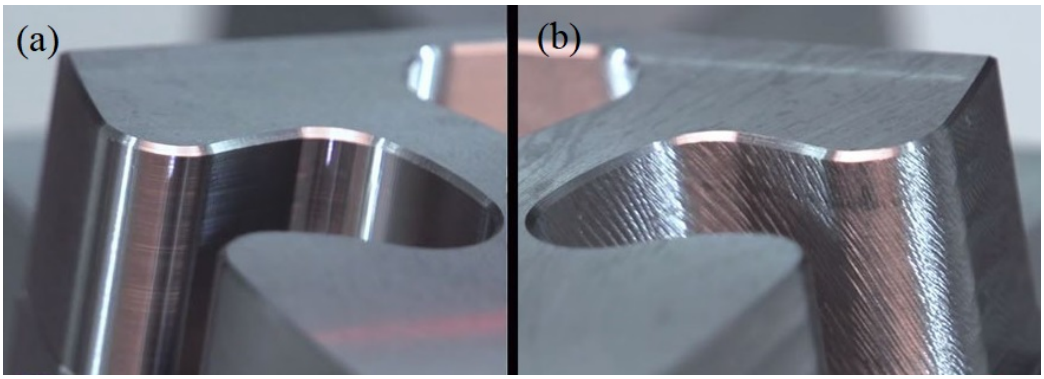

Figure 1.2: (a) Smooth surface finish after machining without chatter vibrations, (b) unacceptable surface finish due to chatter vibrations [3].

Modeling and suppression of chatter vibrations in CNC machining are well-studied subjects and the developments in this area have led to significant improvements in the productivity of machining processes. The available studies, however, are not suitable for robotic machining because of the fundamental differences between the dynamics of a machining robot and conventional CNC machine tools. Figure. 1.3 shows the direct Frequency Response Functions (FRF) measured at the Tool Centre Point (TCP) of a milling tool mounted on a conventional CNC machine tool, and the direct TCP FRF of a milling tool mounted on a machining robot. The FRF quantify the dynamic response of the system to excitation in the frequency domain. As shown in this figure, the static compliance at the TCP is an order of magnitude higher in the machining robot. In addition, the TCP dynamics in CNC machine tools is mainly dominated by high-frequency (typically >500Hz) vibration modes that are originated from the stiffness of the spindle shaft, toolholder, and the tool; however, the TCP dynamics in robotic machining systems is primarily dominated by highly flexible low-frequency (<100Hz) modes that are attributed to the compliance of the robot joints. In the presence of high-amplitude vibrations due to such high compliance, nonlinear effects can potentially be amplified and alter the dynamic response of the system. It is worth mentioning that the robot FRF shown in Fig. 1.3 is measured at a given posture of the robotic manipulator, while the robot dynamics is pose-dependent because the dynamic flexibility is originated from the joints' flexibility. The pose dependency of dynamics is another challenge in robotic machining operations. However, regardless of the posture, the fundamental differences mentioned earlier exist between the dynamics of conventional CNC machine tools and machining robots. Such differences may lead to fundamental distinctions between the nature of vibrations arising in CNC

machining and robotic machining. As a result, new vibration models need to be developed by considering the distinct characteristics of machining robots. Such models are essential to selecting optimum machining parameters and suitable vibration reduction strategies, thus enhancing productivity of the process.

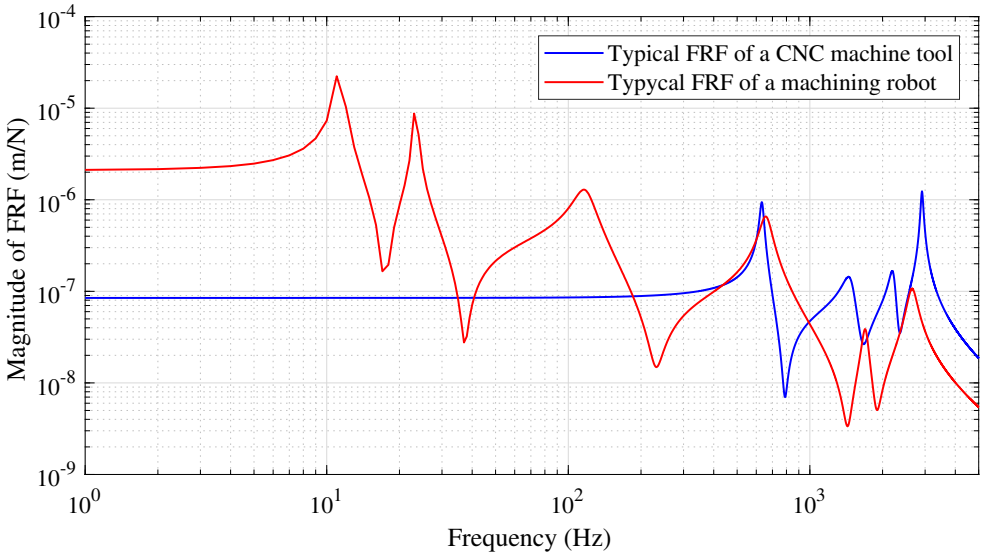

Figure 1.3: Comparison of FRFs of a conventional CNC machine tool (DECKEL MAHO DMU 50e 5-axis milling center) and a machining robot (KUKA KR210).

As will be discussed in detail in the literature review provided in Chapter 2, there have been several studies on static compliance modeling and compensation of static errors, as well as the pose-dependency of robots' dynamics. However, fewer studies have considered the variation of robot dynamics under machining conditions (in a given posture) due to structural nonlinearities and its effects on chatter vibrations. Most, if not all, of the existing models in the literature are developed based on the assumption of linearity of structural dynamics. To address this gap, the following objectives are considered in this thesis:

- Investigating the effect of robots' high compliance on the cutting forces model (Chapter 3),
- Developing a model of the robot's structural dynamics, with focus on its nonlinearities, to accurately predict the system's dynamic response under high-amplitude milling forces (Chapters 4 and 5),

- Bifurcation analysis of the robot's nonlinear vibrations under milling forces (Chapter 6),
- Developing a practical procedure to accurately predict chatter during robotic milling (Chapter 7).

1.3 Summary of the methodology and key outcomes

The research objectives of this thesis are accomplished through literature review, followed by a combination of numerical simulations, analysis of experimental data, and analytical modeling.

In **Chapter 2**, a background on machining vibrations is provided. Then, state-of-the-art in robotic milling is reviewed with focus on the structural dynamics of the system and chatter vibrations.

In **Chapter 3**, the effect of robot compliance on milling forces is investigated. A new three-dimensional cutting force model is developed. The model shows that flexibility in the axial direction, which is normally low in CNC milling, introduces additional components to the cutting forces. The conditions in which the additional components can affect the chatter stability limit are discussed.

In **Chapter 4**, linearity of the structural dynamics, which is a widely-used assumption in the literature, is examined by analyzing experimental data. The data are collected while the robot is excited with harmonic forces with different amplitudes. The analysis reveals significant nonlinearities in the dynamic response of the robot's structure which can significantly alter the chatter prediction.

In **Chapter 5**, after detection of nonlinearity, a new procedure is developed to model the structural nonlinearities and identify the parameters of the model based on the concept of higher-oder FRF. The identified model consists of cubic stiffness and damping characteristics, and it can predict the dynamic response of the robot when subjected to different excitation conditions.

In **Chapter 6**, the developed model of structural dynamics is combined with a milling force model. The resulting equations are used to generate bifurcation diagrams for the vibrations of the nonlinear robotic milling system. For this purpose,

the numerical continuation method is used. The governing equations of motion include non-smoothness because of the intermittent engagement of the rotating milling tool and loss of contact between the tool and the workpiece at high-amplitude vibrations. Smoothing techniques are applied to enable simulations with the numerical continuation method. The effects of nonlinear parameters on bifurcation diagrams are studied.

In **Chapter 7**, two new methods are proposed for in-process measurement of FRF. In-process FRF represent the nonlinear dynamics linearized about the operation conditions. The in-process FRF are used in the linear chatter model to determine the chatter stability limits. The modeling and identification of nonlinear structural dynamics, and then using them in the nonlinear chatter model to develop bifurcation diagrams, require not only tremendous time and effort, but also deep knowledge and expertise in nonlinear dynamics. However, the measured in-process FRF can be used in commercialized chatter prediction softwares which use the linear chatter model for quick prediction of stability limits in an industrial environment.

In **Chapter 8**, a summary of the thesis along with main contributions and recommendations for future work is provided.

Chapter 2

Background and Literature Review

Industrial robots are used in modern industries in a wide range of applications such as part handling, material transfer, spray painting, assembly, and welding, to mention a few. In the manufacturing industry, the involvement of robots started initially for non-machining jobs such as machine tending and later for machining purposes as well. This involvement has widely developed the context of automation in manufacturing. An example of successful application of robots in the manufacturing industry is polishing [16] where robots sometimes even outperform CNC machines [14]. Successful implementation of robots in deburring and grinding has also been reported in many studies [17, 18]. Because of the flexible kinematics and reconfigurability of robots compared to CNC machines, the attention of manufacturing engineers and researchers has been attracted to involvement of robots in other machining processes such as drilling and milling [11]. The flexible kinematics of robots provide a large workspace which can be of great advantage in milling or drilling large pieces or parts with complex shapes and hard-to-access areas. These advantages make them more favorable over CNC machine tools in aerospace, marine, and automotive industries (see Fig. 2.1). For example, the application of robotic machining has been rapidly growing in aircraft fuselage assembly and wind turbine manufacturing processes. Machining robots are also used in the development of hybrid processes, where they alternate between additive (i.e. 3D printing) and subtractive (i.e. machining) operations to manufacture parts with complex shapes and internal channels [19]. Many robot suppliers such as ABB, Kuka, Stäubli, and Motoman have developed robotic arms that are specialized in machining. Although the low rigidity of robots cannot cause big problems in operations such as polishing, it leads to significant machining errors when subjected to large cutting loads in milling or drilling. Contact forces in polishing are

mainly small and high accuracy in positioning of the polishing tool can be achieved. However, the cutting forces in milling or drilling operations are considerably higher. The highly dynamic cutting forces generated at the tool and workpiece interface can cause severe vibrations, which undermine the dimensional accuracy and finish quality of the workpiece and accelerate the wear and breakage of the tool. The consequences are more damaging when those vibrations become unstable and cause chatter [20]. Modeling vibrations during the machining process and implementing effective control and optimization strategies to reduce them are critical challenges in the development of robotic machining systems.

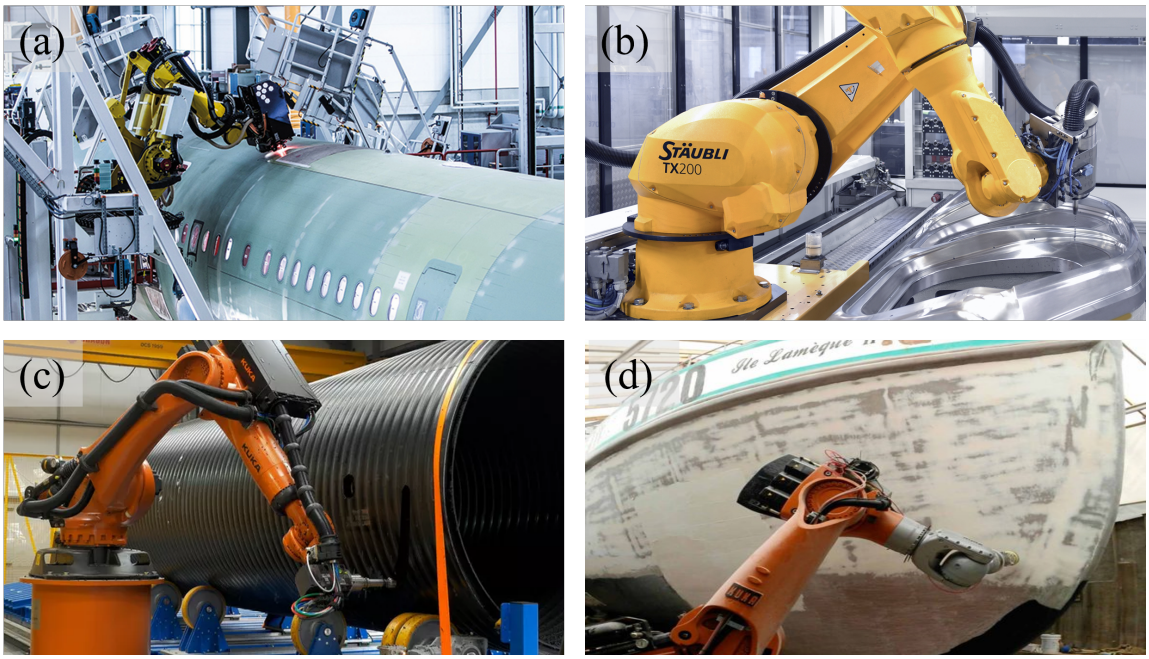

Figure 2.1: Applications of robotic machining systems in (a) aerospace [4], (b) automotive [5], (c) infrastructure [6] and (d) marine [7] industries.

The focus of this thesis is on robotic milling, though similar approaches can be applied to robotic drilling as well. To better understand the dynamics of robotic milling, the dynamics of the milling process, the robot's structural dynamics, and the coupling between them must be studied. In the following subsections, the literature review on machining vibrations, structural dynamics of machining robots, robotic milling dynamics, and nonlinear vibrations in the milling process are presented, respectively.

2.1 Vibrations in milling

2.1.1 Dynamics of milling process

A schematic of a two-dimensional milling process with a flat end mill is shown in Fig. 2.2(a). The tool is assumed to be flexible in feed (X) and normal (Y) directions. The cutting tool moves in the feed direction while rotating at the spindle speed Ω. The total chip thickness removed by the cutting tooth shown in the zoomed view includes a part generated by the feed motion of the machine (shown as h_{st}) and a dynamic part. The feed-generated component h_{st} varies periodically with the rotation angle of the cutting tooth. The dynamic part is due to the current vibrations of the tool (shown by $r(t)$) and the past vibrations of the tool when the preceding tooth was passing the same angular position (shown by $r(t-\tau)$). According to the mechanistic model of cutting forces [21, 22], the cutting forces projected to the tangential (t) and radial (r) directions, as shown in the zoomed area of Fig. 2.2(a), are related to the total chip thickness (h_{tot}) and axial cutting depth (a):

$$F_t = K_{te}a + K_{tc}ah_{tot} \;\;,\;\; F_r = K_{re}a + K_{rc}ah_{tot} \tag{2.1}$$

where the cutting force coefficients K_{te}, K_{tc}, K_{re} and K_{rc} are determined experimentally. The described dynamics in the milling process can be shown by the block diagram in Fig. 2.2-b. The inherent delayed feedback of the vibrations into the machining forces forms a natural closed-loop system as illustrated in the diagram. The delay is constant and depends on the rotational speed and number of cutting teeth. In CNC machining, due to the high rigidity of machine tools, their structural dynamics is usually assumed Linear-Time-Invariant (LTI). Based on this assumption, and using the mechanistic force model in Eq. 2.1, the block diagram in Fig. 2.2-b can be described, in Cartesian coordinates, by non-autonomous linear Delay Differential Equations (DDE) with time-periodic coefficients as follows:

$$\mathbf{M}\ddot{\mathbf{X}}(t) + \mathbf{C}\dot{\mathbf{X}}(t) + \mathbf{K}\mathbf{X}(t) = \mathbf{F}_p(t) + aK_{tc}\left[\alpha(t)\right]\left\{\mathbf{X}(t) - \mathbf{X}(t-\tau)\right\} \tag{2.2}$$

where $\mathbf{M}$, $\mathbf{C}$ and $\mathbf{K}$ are mass, damping and stiffness matrices, respectively. $\mathbf{F}_p(t) = \mathbf{F}_p(t+\tau)$ are the periodic forces, generated by h_{st} and also the first term of forces in Eq. 2.1, with tooth-passing period τ as the principal period. $\mathbf{X}(t) = [x(t) \;\; y(t)]^T$ is

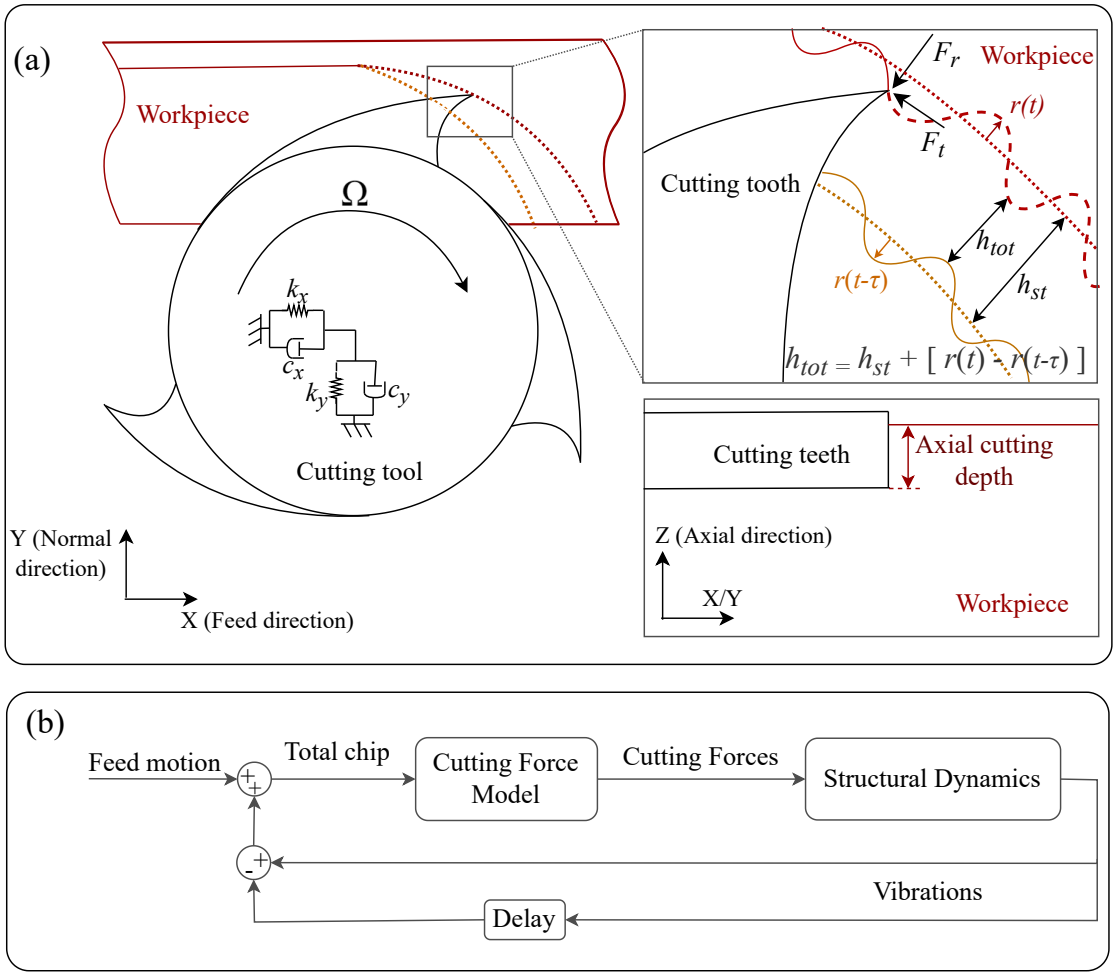

Figure 2.2: (a) Chip formation during milling process, (b) Block diagram of milling process.

the vector of displacement, and $\mathbf{X}(t-\tau)$ is the vector of delayed displacement. The second term on the right side of Eq. 2.2 shows the forces due to the dynamic part of the chip thickness. The entries of the matrix $[\alpha(t)]$ are the directional coefficients which depend on cutting force coefficients and the rotation angle of the tool. The directional coefficients are periodic at the tooth-passing period, that is equal to the time delay τ, i.e. $[\alpha(t)] = [\alpha(t+\tau)]$.

2.1.2 Regenerative chatter

The milling system experiences both forced and transient vibrations during the cutting process. Forced vibrations are due to $\mathbf{F}_p(t)$ and thus, are periodic at the tooth passing frequency. The transient vibrations may grow or decay depending on stabil-

ity of the closed-loop system shown in Fig. 2.2-b. In a stable system, the amplitude of transient vibrations decay due to damping of the system; thus, steady-state TCP oscillations only include forced vibrations. However, when the system is unstable, the transient vibrations cannot be suppressed by the system's damping. Theoretically, the amplitude of transient vibrations grows to infinity in a linear system, and new dynamic motions such quasi-periodic or chaotic motions appear in a nonlinear system. The vibrations developed in unstable conditions are normally called regenerative chatter. The term 'regenerative' refers to the feedback of vibrations into the cutting forces in the closed-loop system.

The early research studies on chatter in milling were developed based on the studies on stability of the turning process. Dynamics of the turning process can be also shown by the block diagram in Fig. 2.2-b; the difference with milling process is the cutting force model: the direction of cutting forces in turning is time invariant and therefore the coefficients of the governing DDE are constant, not periodic. The first stabiliy laws for turning process were developed by Tobias and Fishwick [23], Tlusty and Polacek [24] and Merrit [25]. They formulated chatter by an autonomous linear Delay Differential Equation (DDE) and determined its stability for given cutting parameters. The result of stability analysis is normally illustrated using the Stability Lobes Diagram (SLD) which shows the combinations of axial cutting depth and spindle speed that lead to stable or unstable cutting conditions. An example of the SLD is shown in Fig. 2.3. The solid line shows the border of stability in terms of the cutting parameters (cutting depth and spindle speed). The areas below and above the solid line show the stable and unstable regions, respectively.

The stability laws presented for turning were not applicable to milling because of the periodicity of cutting forces; therefore, various assumptions were used to simplify the problem. Koenisberger and Tlusty [26] considered an average direction and an average number of cutting teeth. Opitz et al. [27, 28] suggested using the average value of the periodic coefficients. The first theoretical analysis that considered the periodicity of the coefficients was presented by Sridhar et al. [29]. They developed a numerical algorithm to determine stability of the milling process that was flexible in one direction. Minis et al. [30] and Minis and Yanushevsky [31] considered a milling system with flexibility in both feed and normal directions. They applied Floquet theory to determine the cutting depth at the stability limit at different spindle speed. Later, Budak and Altintas [32] developed Multi-Frequency Solution (MFS) to determine the stability limit in the SLD. They aprroximated the periodic coeffi-

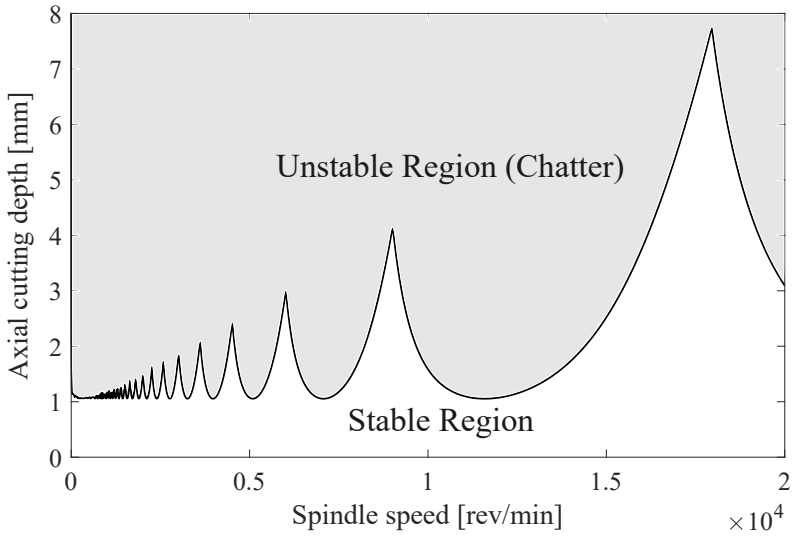

Figure 2.3: A sample stability lobes diagram.

cients in $[\alpha(t)]$ with their Fourier expansion. Considering a certain number of terms in the Fourier expansion, an iterative algorithm is applied to generate the stability lobes. They also showed that the average term of the Fourier expansion of the periodic coefficients is sufficient for accurate chatter stability analysis in common milling applications. The solution with only the average term is called Zero-Order Approximation (ZOA) method. Unlike MFS, ZOA offers a closed-form solution to find the axial cutting depth and spindle speed at the border of stability. Since ZOA only uses the average term of periodic coefficients, secondary Hopf (Torus, or Neimark-Sacker) bifurcation of the forced periodic oscillations is the only type of stability loss that is predicted by this method. However, in high-intermittent cutting conditions, such as low radial immersion milling, other types of bifurcations including period-n bifurcations can occur that can be predicted by MFS. The accuracy of MFS solution depends on the number of Fourier expansion terms included. Later, discretization methods were used to study the stability of vibrations in machining. The Semi-Discretization Method (SDM) by Insperger and Stepan [33] and Full-Discretization Method (FDM) by Ding et al. [34] are the two discrete time-domain approaches that are widely used for chatter modeling in machine tools. In these methods, the time-periodic characteristics of the directional coefficients $[\alpha(t)]$ can be maintained in the solution. By discretizing the continuous-time equation, we are able to approximate the distributed-parameter system in Eq.2.2 by a lumped-parameter system described by its state transition matrix, $\mathbf{\Phi}$, as follows:

$$\mathbf{u}_{k+1} = \mathbf{\Phi}\mathbf{u}_k; \;\; k = 1, 2, .. \tag{2.3}$$

where $\mathbf{u}_k$ is the state vector of the approximate lumped-parameter system. This lumped-parameter system is asymptotically stable if and only if all of the eigenvalues of the state-transition matrix $\mathbf{\Phi}$ are inside the unit circle on the complex plane. The dimension and composition of the state vector and its corresponding transition matrix vary by the applied discretization method (e.g. SDM, FDM). Nonetheless, the state transition matrix depends on cutting parameters (e.g. depth of cut and spindle speed) as well as the modal parameters at the TCP. Unlike ZOA and MFS, SDM and FDM represent the full dynamics. However, they require the modal parameters derived by applying modal analysis to the measured transfer function $\mathbf{H}(s)$, or equivalently the FRF $\mathbf{H}(i\omega)$, while the measured FRF can be directly used in the frequency domain approach.

In both frequency domain and time domain approaches, accurate estimations of the FRF or the modal parameters extracted from them at the TCP are required. The accuracy of the resulting SLD are directly correlated with the accuracy of the FRF used to compute them. In Section 2.2, the approaches to model the structural dynamics of robotic machining systems are reviewed, which is followed by Section 2.3 discussing chatter vibrations in robotic milling.

2.2 Modelling of structural dynamics

There is a direct link between the vibrational behavior of a machining process and the structural dynamics of the machining equipment (e.g. machine tool or robotic arm). Therefore, studying the structural dynamics of the machining equipment has been a key component in the search for proper machining strategies and eventually achieving increased process efficiency without violating the quality constraints.

The most distinct difference between the structural dynamics of machining robots and CNC machine tools is that the dynamic response of robots varies within the workspace. Each configuration of the robot leads to different mass and stiffness distribution and therefore different vibration modes [35, 36]. Many studies have been focused on investigating the posture-dependent dynamics of robots and ultimately developing models that can predict the dynamic response of the robot in various postures. The flexibility of joints is widely reported as the major source of robot

compliance [37, 12]. As a result, modeling and identification of robot joint stiffness have been of great interest to researchers. An early work on modeling of robot stiffness was done by Salisbury [38] where he derived a relationship between joint stiffness values and the end-effectors Cartesian stiffness matrix using the Jacobian matrix of the robot. Later on, Chen and Kao [39] showed that the formulation derived by Salisbury is only valid at the unloaded equilibrium configuration. They proposed Conservative Congruence Transformation (CCT) for mapping stiffness matrices between joint and Cartesian spaces which considers the effects of configuration changes due to external loads on Cartesian stiffness. Along with the studies on modeling robot stiffness, many researchers have also worked on developing stiffness identification procedures. To mention a few, Abele et al. [40] studied modeling of the robot structure and identification of its parameters focusing on the joints' stiffness and its behavior under the milling forces. They extended the identified model to predict the tooltip (TCP) displacements [41]. Later, a fast and robust method of joint stiffness identification of a six revolute serial robot was developed by Dumas et al. [42]. In this procedure, both rotational and translational displacements of the robot end-effector subjected to cutting forces were considered. Most, if not all, of the studies in robotic milling applications, have considered linear torsional springs to model the flexibility of the joints.

The developed joint stiffness model and the associated identification procedures are being used by researchers to predict the overall robot dynamic response. In this regard, two main approaches have been used. The first approach, so-called flexible joints and rigid bodies, is based on the assumption that the elasticity is concentrated at the joints (see Fig. 2.4). In this approach, the Multi-Body Dynamic (MBD) model of the robot with rigid links (bodies) is used to obtain the dynamic response of the system at the TCP. This approach is described in [43] and have been used in [44, 45, 8]. Huynh et al. [8] presented a combination of the rigid body model identification method and the experimental modal analysis to determine the inertial parameters of the rigid bodies and the joints' linear stiffness and damping parameters.

In another approach, the multi-body dynamic model is developed using beam elements as elastic links [46]. This approach has mostly been applied on very elastic and light-weight research robots [47] while the first approach is widely used for robots in robotic machining applications due to their highly flexible joints compared to the links.

Although remarkable improvements in modeling robots' dynamics using multi-

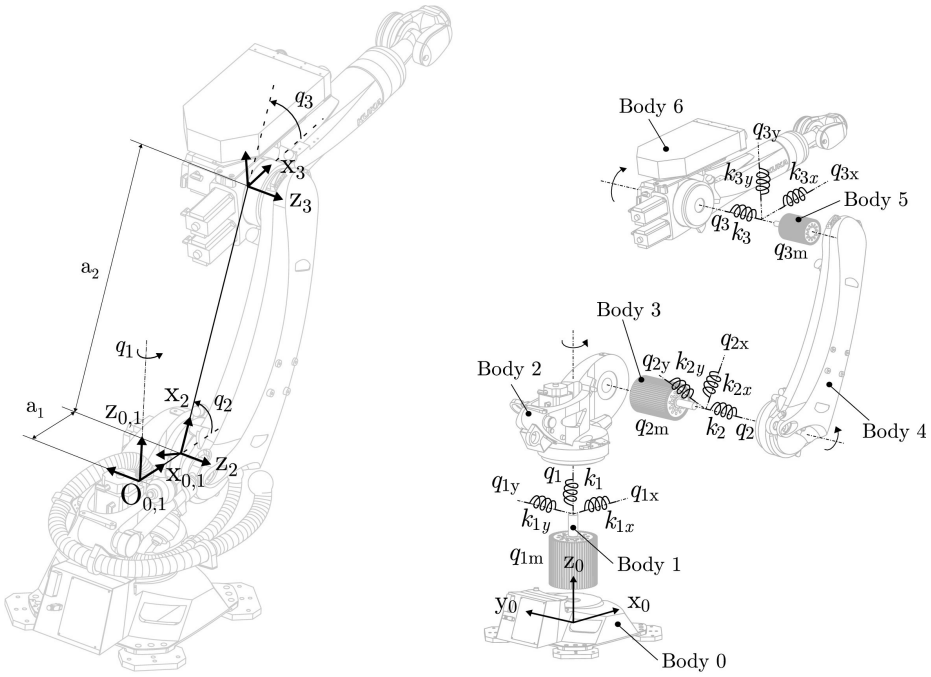

Figure 2.4: Multi-Body Dynamic modeling of robotic machining system with rigid bodies and flexible joints [8].

body dynamics models have been achieved, identification of the inertial and joint elastic parameters for the MBD models requires extensive experiments. Besides, the large number of unknown parameters may make the model parameters globally unidentifiable. Data-driven methods are also used to model the pose-dependency of the FRF, but the trained model shows a large variance outside the range of postures that are used for training [48, 49, 50]. Developing a complete model along with reliable and robust identification methods which can be utilized to predict the dynamic response at any arbitrary posture is still an open problem. An important drawback of the existing models is the inability of the multi-body dynamic models to predict the asymmetrical FRF observed in many robotic machining systems [36], including the KUKA robot available in the Dynamics and Digital Manufacturing (DDM) research laboratory of the University of Victoria, which violates the reciprocity property of self-adjoint linear systems [51]. Elosegui [52] showed that the asymmetry in the dynamic response of robots cannot be due to measurement issues. Based on his experiments, regardless of how carefully the measurement techniques are designed to avoid possible errors, the effects of the nonlinearities exist leading to asymmetrical FRF which cannot be predicted by linear multi-body dynamic models. Such complexity

of the robot's dynamic response is the main reason that many researchers prefer to directly measure the dynamic response neglecting its variations with a configuration change. The measured FRF can be directly used in frequency domain analyses of chatter stability in the milling process. The common practice to measure the structural dynamics of a robotic machining system is through the hammer tap test [53, 54] in which an impact is applied and the impulse response function of the system is measured. Although the cutting forces are distributed along the milling tool [55, 56], because of the typically small axial depth of cut in robotic milling (to avoid excessive deflections), the cutting forces are assumed to be concentrated at the tool-tip. Therefore, impulse-hammer tests are conducted only at the tool-tip, i.e. TCP of the robot. Because the structural dynamics of the robotic arm depends on its posture, which may change during the machining of a relatively large workpiece, a set of FRFs measured at different positions along the machining path have to be used [35, 57].

Regardless of the methods used to model the TCP vibration response, linearity of the response is the common assumption among all the contributions reviewed above. Although the directly measured dynamics capture the asymmetrical FRF, because the impulse hammer tests are performed in the idle state of the robot, the effect of machining conditions on the excitation of nonlinearities is not included. This effect is especially important in robotic machining where the amplitude of forced vibrations is much larger than those in CNC machining. Because of the high rigidity of traditional CNC machine tools, the tool's vibration response is usually assumed to be linear. However, in some cases, the nonlinear effects excited in machining conditions can alter the dynamic response even in CNC machining. That is why several research studies have been conducted in CNC machining to measure in-process FRF. To the author's knowledge, there is no published research to focus on the in-process dynamics of robotic machining systems. In the following subsection, some of the approaches used in CNC machining to measure the in-process dynamics are reviewed.

2.2.1 In-process structural dynamics

Experimentally measured FRF are usually obtained by impulse hammer tests conducted in idle conditions. However, the FRF in operational conditions may differ. The idle condition represents the situations in which the robot is at rest and the operational condition is referred to the conditions in which milling operation is performed and the tooltip is subjected to cutting forces. Different approaches can be

applied to measure the FRF under operational conditions in CNC machining.

Operational Modal Analysis (OMA), which estimates the modal parameters from vibration response to ambient noise excitation, can potentially be applied to estimate in-process FRF [58]; however, because the mode shapes resulting from OMA are not mass-normalized due to the lack of input measurement, the resulting FRF are not applicable for chatter stability analysis. Besides, the modal parameters resulting from OMA represent the dynamics of the closed-loop (regenerative) system and not the robot's (or machine tool's) structural dynamics [59, 60]. Alternatively, milling forces that are measured by dynamometers during the process can be used as the excitation source for in-process FRF estimation. The FRF estimated by this method are not affected by the feedback loop in the process and are scaled to the physical unit; therefore, they are applicable for stability analysis. As an early work, Opitz and Weck [61] followed this idea and used a dynamometer to measure cutting forces and a seismic pick-up sensor to measure the relative movements between the cutter and the table. In this approach, the cutting forces should excite the flexible modes sufficiently. For this purpose, Minis et al. [62] designed a specialized workpiece with randomly distributed channels to provide random cutting forces during the turning process. Later, Ozsahin et al. [63] employed a similar idea to measure in-process FRF in milling. In these works, the spindle speed was kept constant and the broadband excitation was because of the specially designed workpiece. However, Aguirre et al. [64] and Iglesias et al. [65] swept the spindle speed while milling normal workpieces to provide excitation at several frequencies by the cutting force harmonics. Takasugi et al. [66] used both techniques simultaneously. They applied variable speed while milling a workpiece with a sinusoidal surface to provide harmonic excitation. The measured FRF had lower natural frequency and higher stiffness compared to FRF measured in idle conditions. In this approach, the milling forces simultaneously excite the system in multiple directions with correlated forces. The correlation of milling forces is not important when this method is applied to machine tools but becomes important in robots. Because the vibration response of the machine tool in each Cartesian direction is uncoupled from others, FRF in each direction can be estimated as a Single Input Single Output (SISO) [65, 63].

Inverse stability analysis can also be used to determine the FRF under operational conditions. In this approach, experimentally identified chatter stability limits are substituted in the theoretical model of chatter to inversely determine the modal parameters. Ozsahin et al. [67] presented a method based on this inverse approach

and showed that the parameters of the flexible mode can be identified based on the limiting cutting depths at two relatively close spindle speeds. Grossi et al. [68] augmented the inverse method by combining it with the speed ramp-up technique to improve the accuracy of the identified FRF in a wide range of spindle speeds. Both of these two works confirmed the substantial variation of the FRF under operational conditions from those measured in idle conditions. Postel et al. [69], also following inverse methodology, employed a machine learning-based method to identify the unknown natural frequency and damping ratio of the system based on several measured chatter stability limits and the corresponding frequencies.

For robots, nonlinear mechanisms such as strain hardening/softening, friction, and hysteresis effects in the robot's revolute joints are minimally active in idle conditions but become prevalent under operational loads [70, 71, 72, 73]. Idle and in-process FRF can be different even without the operational loads. This was shown in Tunc and Gonul's study where they observed a significant variation in the FRF measured by an impulse hammer test conducted on the idle robot and when it moves at a constant speed [74]. The FRF measured in idle condition are therefore not representative of the vibration response under operational conditions and new FRF measurement methods need to be developed for chatter analysis in robotic machining.

2.3 Vibrations in robotic milling

For robotic milling, two types of chatter mechanisms have been reported in the literature: Regenerative chatter that was discussed in section 2.1, and Mode Coupling chatter which was described by Tlusty and Ismail [21, 9]. According to the mode-coupling mechanism, chatter occurs due to the simultaneous vibrations of the cutting tool in various (lateral) directions with different phases and amplitudes. The mechanism was explained using Fig. 2.5 in [9]. The cutting tool is flexible in the two directions X_1 and X_2. The motion of the cutting tool in the U-Z plane forms an ellipse as shown in the zoomed area. The direction of the total cutting force is shown by an arrow. Assume the direction of motion is clockwise. When the tool moves on this elliptical path in the direction from point 2 to point 1, the total force acts against the motion (the force brakes the motion); the vibration energy of the tool is lost. However, in the second half of the motion from point 1 to point 2, the force has a positive component in the direction of the velocity of motion (it drives the tool); the tool gains energy. Since the cutting depth during the motion from point 1 to

point 2 is larger, the gained energy is more than the lost energy. This leads to higher vibration amplitude in the next period; this cycle continues and chatter develops.

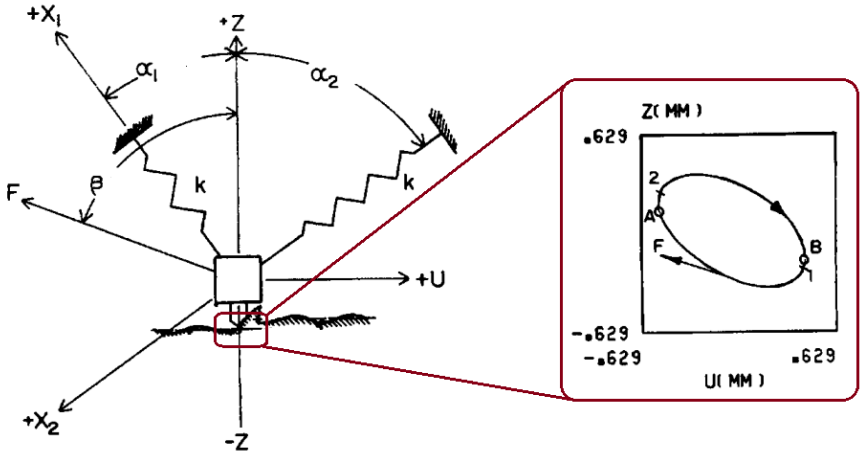

Figure 2.5: Mode-coupling chatter mechanism [9].

A simple analysis shows that mode coupling chatter is more likely to happen if the structural stiffness of the system is low relative to the stiffness at the cutter and workpiece interface [75]. In machining with conventional CNC machine tools, the structural stiffness of the system is normally high enough so that the regenerative mechanism dominates the vibrations. Therefore, the focus of studies in CNC machining has been on regenerative chatter rather than mode coupling chatter [76, 77]. However, industrial robots are remarkably flexible compared to CNC machines which caused many researchers to report the mode-coupling mechanism as more active than the regenerative mechanism [77]. Gasparetto [75] presented criteria for mode-coupling chatter by analyzing the eigenvalues of the equations of motion. His criteria described the effect of the difference between structural stiffness and cutting stiffness on the stability of the process. Similar to previous works in [23, 78, 32] which studied regenerative chatter, the equations of motion were obtained by combing the linear structural dynamics model and cutting forces model. However, in the cutting force model that Gasparetto used, the effects of the delayed vibrations were neglected. Later, Wang et al. [79] and Pan et al. [80] applied Gasparetto's theory to robotic milling applications. It was shown that mode coupling is the dominant source of vibrations in robotic milling caused by flexible low-frequency modes of the robot structure. They developed a chatter stability criterion based on the principle stiffness values and directions at the TCP. According to this criterion, chatter is more likely to happen if the smaller principal stiffness direction lies within the angle formed by the total cutting

force and the normal to the machined surface. Cen et al. [81] updated this criterion by considering CCT in mapping stiffness matrices between joint and Cartesian spaces. Based on this modification, they developed a chatter avoidance method which suggests changing the feed rate to stabilize the process. Gasparetto's approach to predicting mode coupling stability was also followed by Cen et al. [81]. In this work, the structural dynamics model was developed by using the CCT stiffness model. Based on this modification, they developed a mode coupling chatter avoidance technique which suggests changing the feed rate to stabilize the process. Although Gasparetto's approach provides a simple and straightforward tool to describe the mode coupling mechanism separately and to study the effects of structural stiffness on stability, it suffers from the fact that the delayed vibrations, and consequently the regenerative mechanism, are neglected in the cutting force model. Jafarzaded and Movahhedy [82] showed that both mechanisms can be activated at the same time. They used numerical simulations to demonstrate the interaction between the two mechanisms for different cutting parameters.

It should be noted that the chatter model developed by Budak and Altintas for milling operations, which considers the delayed term in the differential equations, inherently covers the mode coupling mechanism, as well as the regenerative mechanism [83]. Hence, it can be considered as a complete set of equations of motion to solve the stability problem in robotic milling applications as well. Therefore, several researchers adapted the chatter stability analysis in CNC machining to robotic machining. Mousavi et al. [46] also used the frequency domain method to predict the stability limit for robotic milling. They combined the regenerative chatter model with a linearized multi-body dynamic model of the robot with flexible links. Li et al. [53] generated the stability diagrams by using the frequency-domain method for the robot Fanuc-1000i. They directly measured the FRFs of the robot using an impulse hammer test and showed that cross-FRF contribute to the system dynamics much more significantly in robots than in machine tools. Similarly, Cordes et al. [84] applied both the frequency domain solution and SDM to generate the stability diagram using measured FRFs and the corresponding extracted modal parameters. They showed that the posture-dependent modes of the robot (typically lower than 50 Hz) affect its stability in low-speed machining, but the stability of high-speed machining is mainly dominated by the invariant high-frequency vibration modes of the tooling system (assembly of spindle, holder, and tool).

Although robot's vibration modes may not contribute to chatter vibrations at high

spindle speeds, the static deflections at the tooltip due to the robot's static structural stiffness can cause variation in the stability diagrams. Due to these deflections, the actual radial and axial cutting depths deviate from the nominal values which affect the stability diagrams at all spindle speeds.

2.4 Nonlinearities in machining vibrations

Although the robotic milling system is inherently a nonlinear system due to the presence of Coriolis and centrifugal forces, structural nonlinearities, and nonlinearities in cutting forces, except for a few studies such as [45], linear models have mostly been used to study the dynamics of robotic machining systems. However, to the best of the author's knowledge, there is no published research with a focus on studying the nonlinear dynamic behaviour in robotic milling. On the contrary, nonlinear vibrations in milling with CNC machine tools have been studied by several researchers, even though the nonlinearities in CNC milling are weak compared to robotic milling. Nonlinearities can be associated with either the cutting forces or the structural dynamics of the machining equipment (machine tool or machining robot) [85]. The nonlinear behaviour of the cutting forces stems from the material's constitutive relationship, chip formation mechanism, process damping, and loss of tool-workpiece contact [86].

The existing nonlinear models of chatter are mostly focused on chatter in turning operation, where the dynamics can be modelled by a scalar DDE without the time-periodic coefficients. Hanna and Tobias [87] presented an SDOF model of turning dynamics that includes quadratic and cubic stiffness terms and a third-degree polynomial of present and delayed vibrations describing regenerative machining forces. Using the Harmonic Balance method, they showed the Hopf bifurcation of the system's fixed (equilibrium) point. They also introduced the concept of finite-amplitude instability as the post-chatter state where the vibration amplitude stabilizes at a constant amplitude, i.e. supercritical stability exists. The numerical simulations presented by Tlusty and Ismail [9] identified the intermittent loss-of-contact of the tool and workpiece at high-amplitude oscillations as the source of nonlinearity that causes finite-amplitude instability in both milling and turning operations even with linear stiffness, damping, and machining forces. Shi and Tobias [88] confirmed that the structural nonlinearities in machine tools can be neglected compared to the nonlinearity of machining forces and intermittent loss-of-contact. Similar to [87], Nayfeh et al. [89] investigated the impact of quadratic and cubic stiffness and delay terms in the

equation of motion. But they used Multiple Scales and Harmonic Balance methods to show that considering higher-order terms in Harmonic Balance is necessary for the correct determination of the criticality of Hopf bifurcation. They also studied the post-chatter bifurcation of the periodic solution arising from the Hopf bifurcation of the fixed point, although the intermittent loss-of-contact in post-chatter dynamics was neglected in their work. It was demonstrated that nonlinear stiffness and time delay effects are in fact sufficient in a single degree of freedom system to cause limit-cycle, quasi-periodic, and chaotic dynamic behaviours. Effects of nonlinear time-delay terms were also studied by Fofana [90] using the integral averaging method and Lyapunov exponents. Lin and Weng [91] proposed a process model including the nonlinear relationship among cutting angles and the variation of shear angle during feedrate changes. They used the multiple scale method to study the weak nonlinear stability of the process. They showed that the nonlinear chatter frequency is smaller than that of linear prediction, and chatter frequency slowly decreases with the increase of cutting depth. Later, the hysteresis effect was also added to the cutting force model by Moon and Nagy [86]. Another tool to investigate the dynamics of nonlinear DDE is the numerical continuation method. Dombovari et al. [92] used the numerical continuation method to study chatter in turning with linear structure but machining forces with a third-degree polynomial function of the present and delayed vibrations. By considering the loss-of-contact in post-chatter dynamics, they formulated the system dynamics with a nonlinear non-smooth DDE where the instantaneous chip thickness defines the switching manifold. They used a smoothing technique and numerical continuation to develop the bifurcation diagram of the system, which showed that the periodic motions arising from Hopf bifurcation may directly become chaotic due to loss of contact.

Adopting nonlinear chatter analysis methods from turning to milling is challenging. Not only are the coefficients of the DDE describing milling dynamics time-periodic (as opposed to the fixed coefficients in turning), but also the milling tool is usually equally flexible in more than one mode and thus MDOF models are required. Besides, in addition to the non-smoothness caused by loss of contact, the intermittent engagement of the cutting edges with the workpiece in each tool revolution generates additional non-smooth terms in the equations of motion. As a result, the general chatter model in milling is a system of coupled nonlinear DDE with time-periodic coefficients and non-smooth terms. Therefore, most of the works in nonlinear milling systems have used numerical simulations. Minis [30] studied the nonlinearities that

arise when the tool loses contact with the workpiece due to high amplitude vibrations through numerical integration of the governing equations. There have been more studies investigating nonlinear dynamics of the milling process using numerical integration such as [93, 94, 95, 96]. Although numerical integration methods are time-consuming, the full dynamics of the system can be considered without requiring assumptions which are normally considered in analytical solutions. Moradi et al. [97] presented a nonlinear model for milling chatter that includes structural and force nonlinearities in the form of polynomial functions of present and delayed vibrations. In order to simplify the time-periodic and non-smooth dynamics, they approximated the periodic coefficients with their average over one principal period. This simplification enabled the application of a two-dimensional Multiple Scaled method to determine the stability of vibrations; however, by removing the periodic coefficients from the equations, the forced periodic solution and the possibility of period-doubling bifurcation were also removed from the results.

Most of the studies on nonlinear chatter mentioned above were conducted years ago when the chatter instability in CNC machining was not as well-known as it is nowadays; in recent years, the number of publications on nonlinear chatter in CNC machining has been considerably decreased. This is due to the fact that the developed linear models have been highly successful in predicting the dynamics of the system observed experimentally. There has been a broad consensus that both the structure of CNC machine tools and the milling cutting process can be accurately modelled as linear systems in most cases. However, the structure of robots is extremely flexible compared to conventional CNC machine tools and the resulting high amplitude vibrations can excite the possible nonlinearities considerably. The compliance of articulated robots mainly originates from the flexibility of their revolute joints, where nonlinear mechanisms such as backlash, friction, and hysteresis effects are prevalent [71, 72, 73]. Kircanski and Goldenberg [70] showed that, in addition to the backlash, friction and hysteresis effects, the joint's stiffness is also significantly nonlinear. Their experiments on a single joint with a harmonic drive showed that a cubic stiffness term has to be added to the linear stiffness model of the joint to describe its dynamics. The nonlinearities in the joints subsequently lead to the nonlinearity of the vibration response at the robot's TCP. Despite these observations, the common assumption in the existing chatter models of robotic milling is the linearity of the robot's structural dynamics, similar to CNC machine tools. The structural nonlinearity of robots causes discrepancies between analytical predictions using linear models with experimental

results [84]. Therefore, studying nonlinear effects in robotic milling is essential in order to properly understand the dynamic behaviour of the system.

Chapter 3

Effect of axial vibrations on regenerative chatter

Modeling chatter in robotic milling has been naturally adapted from CNC milling. However, the highly flexible structure of industrial robots introduces new challenges to modeling vibrations during robotic milling processes. As mentioned in Section 1.2, one of the challenges is high flexibility of the robotic machining system in all directions, including axial direction. Although the dynamic deflections of the tool in the axial direction has been considered in some researches such as [53, 54], its effect on the modulation of the axial depth of cut was neglected. This chapter studies the contribution of the axial vibrations of the milling end-effector to regenerative chatter in robotic milling. The numerical case studies show that the modulation of the nominal depth of cut due to axial vibrations introduces nonlinearities in the cutting forces. Moreover it results in additional feed and edge forces that can alter stability of the vibrations.

3.1 Dynamic force model

A Multi Degree of Freedom (MDOF) milling system with a round-end tool (e.g. ball end or bull nose) having N teeth is considered as shown in Fig. 3.1 . Assuming a small axial depth of cut, a, the cutting forces on each tooth j ($j = 1, ..., N$) are assumed to be concentrated at the midpoint of its engaged length. The forces acting on each tooth are functions of axial depth of cut a, and chip thickness h_j. The total chip thickness consists of the portion generated by feed motion of the tool, $h_{f,j}$, and the

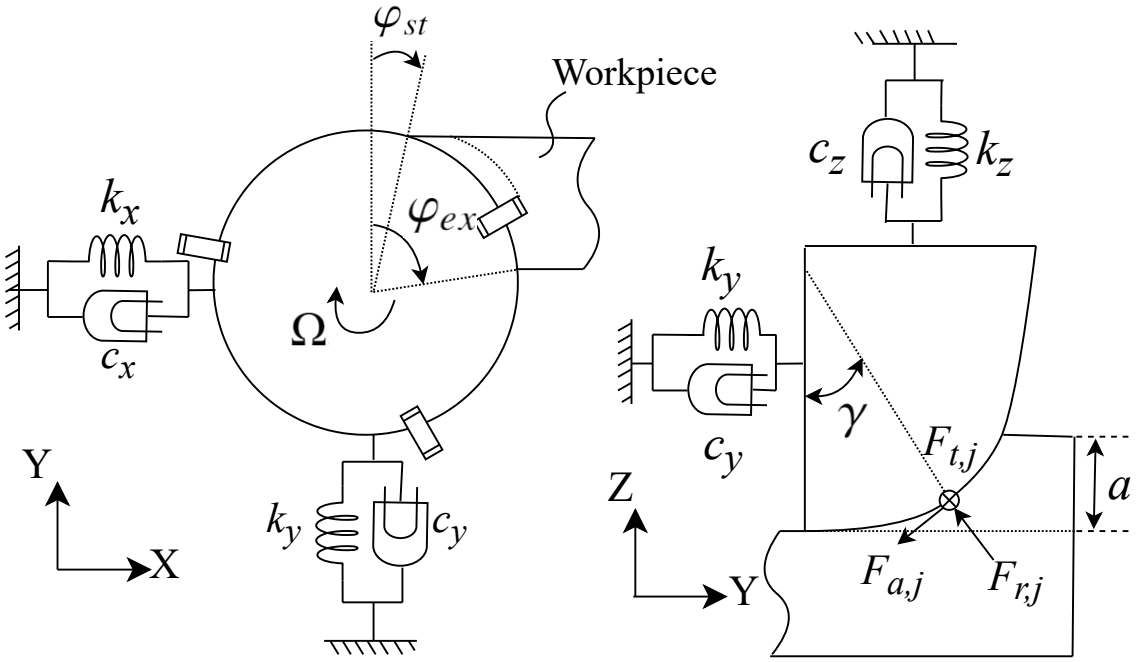

Figure 3.1: Three dimensional model of milling forces.

portion generated by the vibrations of the tool, $h_{v,j}$ [22]:

$$\begin{aligned} &h_j(\varphi_j) = h_{f,j}(\varphi_j) + h_{v,j}(\varphi_j); \\ &h_{f,j}(\varphi_j) = f_t \sin\varphi_j \sin\gamma \\ &h_{v,j}(\varphi_j) = \Delta x \sin\varphi_j \sin\gamma + \Delta y \cos\varphi_j \sin\gamma - \Delta z \cos\gamma \end{aligned} \tag{3.1}$$

where f_t is the feed per tooth, $\varphi_j = (j-1)\frac{2\pi}{N} + \Omega t$ is the instantaneous immersion angle of tooth j at the spindle speed Ω, and $\Delta x = x(t) - x(t-\tau)$, $\Delta y = y(t) - y(t-\tau)$ and $\Delta z = z(t) - z(t-\tau)$ are the regeneration terms with the tooth passing period $\tau = \frac{2\pi}{N\Omega}$. The milling forces in tangential, radial and axial directions acting on tooth j can be obtained as follows [22]:

$$\begin{aligned} F_{t,j}(t) &= K_{te} s + K_{tc} h_j(\varphi_j) a \\ F_{r,j}(t) &= K_{re} s + K_{rc} h_j(\varphi_j) a \\ F_{a,j}(t) &= K_{ae} s + K_{ac} h_j(\varphi_j) a \end{aligned} \tag{3.2}$$

where $s = \frac{a}{\sin\gamma}$, and γ is the cutting edge angle at the midpoint of the axial engagement, as shown in Fig. 3.1. The constants, $K_{mn}, m = t, r, a; n = e, c$, represnt the edge and cutting force coefficients. The total forces in Cartesian coordinates are obtained by adding the contribution of the cutting forces generated by each one of

the N flutes:

$$\begin{aligned}\mathbf{F}(t) &= \begin{bmatrix} F_x & F_y & F_z \end{bmatrix}^T \\ &= \sum_{j=1}^{N} \mathbf{R}(\varphi_j) g(\varphi_j) \begin{bmatrix} F_{t,j}(t) & F_{r,j}(t) & F_{a,j}(t) \end{bmatrix}^T \end{aligned} \tag{3.3}$$

$$g(\varphi_j) = u(\varphi_j - \varphi_{st}) - u(\varphi_j - \varphi_{ex})$$

In Eq. 3.3, $u(\cdot)$ is a unit step function and $g(\varphi_j)$ is a Heaviside function that determines if tooth j is engaged with the workpiece. The start and exit angles, φ_{st} and φ_{ex}, respectively, are illustrated in Fig. 3.1. Matrix $\mathbf{R}(\varphi_j)$ projects the tangential, radial, and axial forces on the X, Y, and Z directions:

$$\mathbf{R}(\varphi_j) = \begin{bmatrix} -\cos\varphi_j & -\sin\varphi_j \sin\gamma & -\sin\varphi_j \cos\gamma \\ \sin\varphi_j & -\cos\varphi_j \sin\gamma & -\cos\varphi_j \cos\gamma \\ 0 & \cos\gamma & -\sin\gamma \end{bmatrix} \tag{3.4}$$

In machining with conventional machine tools, the system is much more stiff in axial direction compared to lateral directions; hence, the axial depth of cut is assumed to be constant $a = a_o$. However, in robotic machining systems, the structure in axial direction can be as flexible as the lateral directions; or even more flexible depending on the robot posture. Therefore, axial vibrations become significant and cause the actual depth of cut to vary. The actual depth of cut is assumed to be modulated by the axial vibration:

$$a(t) = a_o - z(t) \tag{3.5}$$

Substituting $a(t)$ and h_j from Eqs. 3.5 and 3.1, respectively, in Eq. 3.2, and then the resulting tangential, radial, and axial force components in Eq. 3.3, lead to the following expression of the total cutting forces applied on the milling tool:

$$
\begin{aligned}
\mathbf{F}(t) &= \mathbf{F}_e(t) + \mathbf{F}_f(t) + \mathbf{F}_r(t); \\
\mathbf{F}_e(t) &= \sum_{j=1}^{N} \mathbf{R}(\varphi_j) g(\varphi_j) \begin{bmatrix} K_{te} & K_{re} & K_{ae} \end{bmatrix}^T (a_o - z) \,/\, \sin\gamma \\
\mathbf{F}_f(t) &= \sum_{j=1}^{N} \mathbf{R}(\varphi_j) g(\varphi_j) \begin{bmatrix} K_{tc} & K_{rc} & K_{ac} \end{bmatrix}^T \sin\varphi_j \, \sin\gamma \\
&\qquad f_t \, (a_o - z) \\
\mathbf{F}_r(t) &= \sum_{j=1}^{N} \mathbf{R}(\varphi_j) g(\varphi_j) \begin{bmatrix} K_{tc} & K_{rc} & K_{ac} \end{bmatrix}^T \sin\gamma \\
&\qquad (\Delta x \sin\varphi_j + \Delta y \cos\varphi_j - \Delta z \cot\gamma) \, (a_o - z)
\end{aligned}
\tag{3.6}
$$

As shown in Eq. 3.6, the total milling forces, $\mathbf{F}$, consist of the forces generated by the feedrate $\mathbf{F}_f$ (will be referred to as feed forces hereafter), edge forces $\mathbf{F}_e$ and regenerative forces $\mathbf{F}_r$. In conventional machine tools, due to their high stiffness in axial direction, depth of cut is assumed to be constant at a_o and thus the terms that depend on the axial deflection (Z) are disappeared from Eq. 3.6. As a result, the edge and feed forces do not influence the stability of the system and are neglected in chatter analysis. In robotic milling, as shown in Eq. 3.6, the modulation of depth of cut results in new displacement dependent terms in the edge and feed forces, and a nonlinear term in the regenerative force. In the following two sections, the effect of these additional components on the stability of vibrations will be studied.

3.2 Effect of feed and edge forces

The existing chatter stability prediction methods, such as the frequency domain solution [32] and the time domain semi-discretization method [33], are applied to linear milling systems. As it was shown in the previous section, the dynamic feed and edge forces are linear functions of axial vibrations (Eq. 3.6). Hence, by ignoring the nonlinear term of the regenerative forces, the effect of dynamic feed and edge forces on stability of the system can be investigated through the existing linear methods. In this section, Zero Order Approximation (ZOA) method is used to determine the stability limit of the system considering the effect of axial vibrations on feed and edge forces.

3.2.1 Stability lobe diagrams

As shown in Eq. 3.6, the feed and edge forces consist of a term that depends on the nominal depth a_o, and another term that depends on axial vibrations $z(t)$. While the former term does not affect the stability of the system [22, 32] and can be dropped from equations, the latter terms must be considered in the stability analysis. Also, the nonlinear terms in the regenerative component of the forces are neglected in this section. As a result, the total milling forces in Eq. 3.3 can be re-written as follows:

$$\mathbf{F}(t) = a_o K_{tc} \left[\alpha(t)\right] \left(\mathbf{X}(t) - \mathbf{X}^{\tau}(t)\right) - \left(\left[\beta_e(t)\right] + \left[\beta_f(t)\right]\right) \mathbf{X}(t) \tag{3.7}$$

where $[\alpha(t)]$ is the directional coefficient [32] and the non-zero elements of $[\beta_e(t)]$ and $[\beta_f(t)]$ are as follows:

$$\beta_{e,xz} = \sum_{j=1}^{N} g(\varphi_j) \left(-K_{te} \cos\varphi_j - \left(K_{re} \sin\gamma + K_{ae} \cos\gamma\right) \sin\varphi_j\right) / \sin\gamma$$

$$\beta_{e,yz} = \sum_{j=1}^{N} g(\varphi_j) \left(K_{te} \sin\varphi_j - \left(K_{re} \sin\gamma + K_{ae} \cos\gamma\right) \cos\varphi_j\right) / \sin\gamma$$

$$\beta_{e,zz} = \sum_{j=1}^{N} g(\varphi_j) \left(K_{re} \cos\gamma - K_{ae} \sin\gamma\right) / \sin\gamma$$

$$\beta_{f,xz} = \sum_{j=1}^{N} g(\varphi_j) \left(-K_{tc} \sin\varphi_j \cos\varphi_j - \left(K_{rc} \sin\gamma + K_{ac} \cos\gamma\right) \sin^2\varphi_j\right) f_t \sin\gamma$$

$$\beta_{f,yz} = \sum_{j=1}^{N} g(\varphi_j) \left(K_{tc} \sin^2\varphi_j - \left(K_{rc} \sin\gamma + K_{ac} \cos\gamma\right) \sin\varphi_j \cos\varphi_j\right) f_t \sin\gamma$$

$$\beta_{f,zz} = \sum_{j=1}^{N} g(\varphi_j) \left(K_{rc} \cos\gamma - K_{ac} \sin\gamma\right) f_t \sin\varphi_j \sin\gamma$$

Figure 3.2 shows the variation of the additional coefficients $[\beta_e(t)]$ and $[\beta_f(t)]$ with the immersion angle. Similar to directional coefficients $[\alpha(t)]$, they vary periodically with the rotation of the cutting tool; hence, they can be expressed as Fourier series. Following the ZOA method, the average term of the Fourier series is used for stability analysis [32]:

$$\left[A_0\right] = \frac{1}{T} \int_0^T \left[A(t)\right] dt \;\; ; \; A = \alpha \, , \, \beta_e \, , \, \beta_f \tag{3.8}$$

In Eq. 3.7, $\mathbf{X}(t)$ and $\mathbf{X}^{\tau}(t)$ are the current displacement and delayed displacement vectors, respectively:

$$\begin{aligned} \mathbf{X}(t) &= \begin{bmatrix} x(t) & y(t) & z(t) \end{bmatrix}^T \\ \mathbf{X}^{\tau}(t) &= \begin{bmatrix} x(t-\tau) & y(t-\tau) & z(t-\tau) \end{bmatrix}^T \end{aligned} \tag{3.9}$$

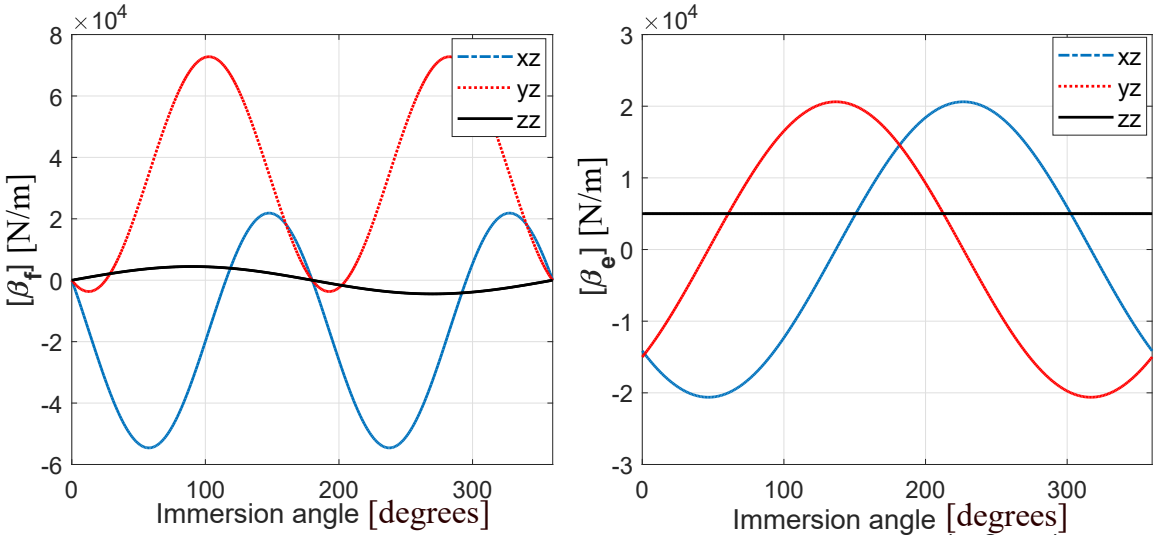

Figure 3.2: Variation of the additional coefficients $[\beta_e(t)]$ and $[\beta_f(t)]$ with rotation of cutting tool.

The current and delayed displacement vectors can be mapped to the force vectors using the Frequency Response Function (FRF) matrix $\mathbf{H}$:

$$\begin{aligned} \mathbf{X}(i\omega) &= \mathbf{H}(i\omega)\,\mathbf{F}(i\omega) \\ \mathbf{X}^{\tau}(i\omega) &= e^{-i\omega\tau}\,\mathbf{H}(i\omega)\,\mathbf{F}(i\omega) \end{aligned} \tag{3.10}$$

By substituting the deflection terms from Eq. 4.4, Eq. 3.7 can be re-written as the following eigenvalue equation:

$$\mathbf{F} = \left\{ a_o \left[\alpha_0\right] \left(1 - e^{-i\omega\tau}\right) - \left(\left[\beta_{e0}\right] + \left[\beta_{f0}\right]\right) \right\} \mathbf{HF} \tag{3.11}$$

The nontrivial solution of the above equation leads to the characteristic equation of the system:

$$\det \left\{ \mathbf{I} - \left(a_o \left[\alpha_0\right] \left(1 - e^{-i\omega\tau}\right) - \left(\left[\beta_{e0}\right] + \left[\beta_{f0}\right]\right) \right) \mathbf{H} \right\} = 0 \tag{3.12}$$

The stability of vibrations at any combination of spindle speed and axial depth of cut is determined by applying the Nyquist stability criterion. The procedure of applying the Nyquist stability criterion for the chatter problem is provided in [98].

3.2.2 Case study

A numerical example is presented to study the effect of the feed and edge forces on chatter stability limits. In order to use a realistic representation of the robot flexibility in this example, the direct and cross FRFs of a KUKA KR 90 robotic arm at its wrist are measured using impulse hammer tests. The measured FRFs are shown in Fig. 3.3. Note that the FRFs at the tool tip, and not the wrist, are to be used in chatter analysis; however, because the available robotic arm did not include a milling end-effector, the FRFs were measured at the wrist to obtain the closest representation of the FRFs at the tool tip.

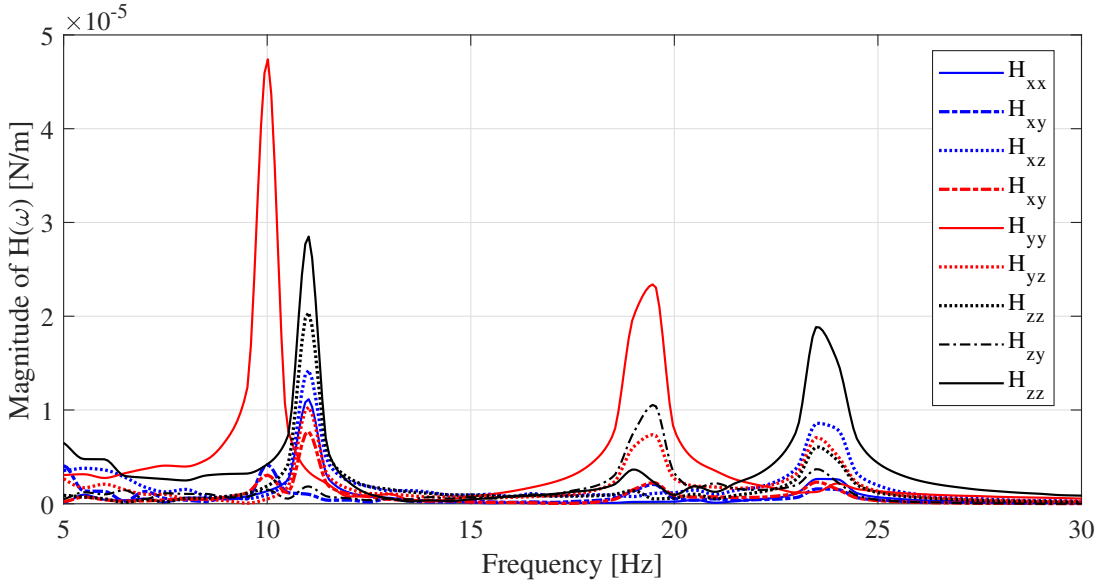

Figure 3.3: Measured direct and cross frequency response functions of the KUKA KR 90 robot with joint angles 0°, −70°, 100°, 0°, 0° and 0°, from first to sixth joint, respectively.

The stability diagrams are developed by applying Nyquist criterion on the characteristic equation obtained at each point on a grid of spindle speeds and nominal axial depth of cut a_o. Note that the robot compliance is posture-dependent and can be significantly high in a flexible postures. As shown in Eq. 3.7, $[\beta_e]$ and $[\beta_f]$ matrices also act as stiffness matrices and can cause considerable variation in stability limit. The contribution of $[\beta_f]$ to the (un)stability of the system is magnified by increasing feed rate as it proportionally increase by feedrate.

Figure 3.4 shows the stability diagrams obtained for machining of Aluminum workpiece. As shown in this figure, stability limit at low speed region ($<$ 500 rev/min)

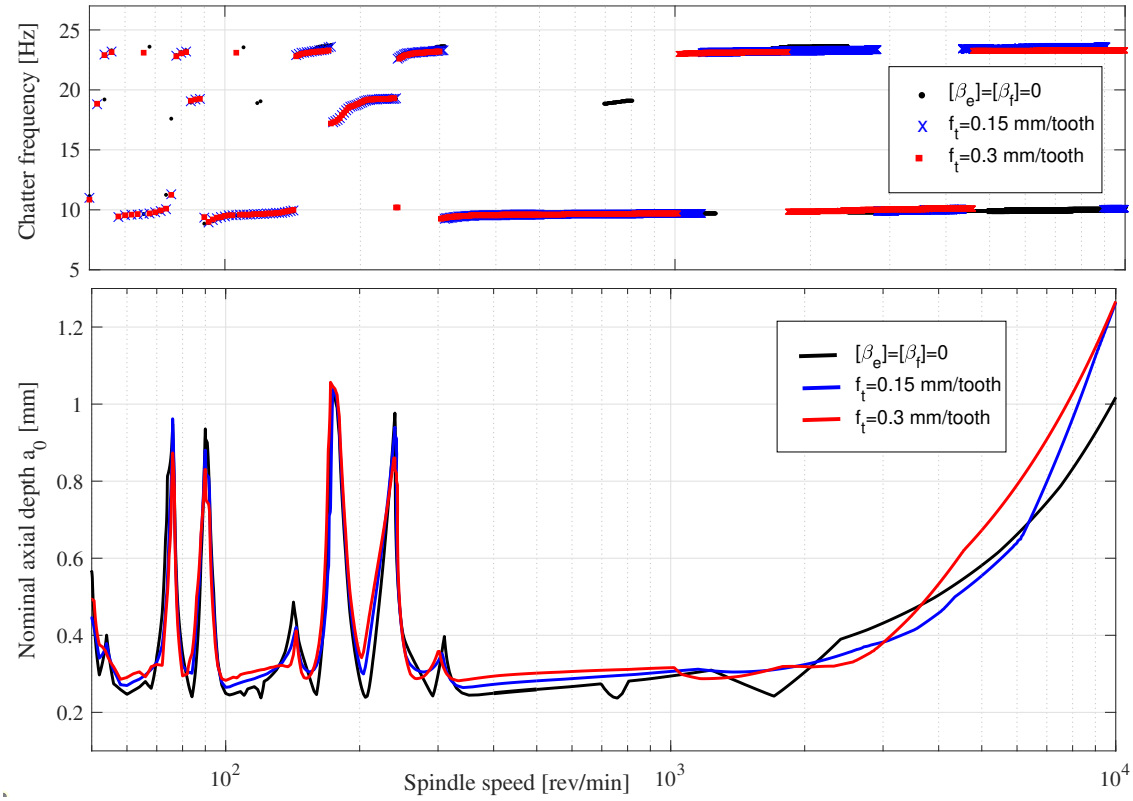

Figure 3.4: Stability limit and chatter frequency of half-immersion down milling of Aluminium with KUKA robot; K_{tc} =691 MPa, K_{rc} =263 MPa, K_{ac} =100 MPa, K_{te} =10 N/mm, K_{re} =10 N/mm, K_{ae} =5 N/mm, γ=50° , N =4.

increases by increasing feedrate. However, the discrepancies between the stability limits with and without the effect of feed and edge forces are even more pronounced at higher cutting speeds. For example, the stability limit at 7000 rev/min increases from 0.74 mm to 0.91 mm for feedrate of 0.3 mm/tooth which corresponds to 22% increase while 17% reduction is observed at 2500 rev/min. Another aspect of the effect of the edge and feed forces on chatter stability can be understood by investigating the chatter frequency shown in Fig. 3.4. At higher cutting speeds, i.e. approximately above 4000 rev/min, chatter mode shifts from the mode at 10 Hz to the mode around 24 Hz. Figure. 3.3 shows that the mode at 24Hz is the most flexible in Z direction. It can be concluded that by taking into account the effect of axial vibrations on modulation of depth of cut, and consequently on the feed and edge forces, the chatter mode shifts to the mode at 24 Hz.

Stability diagram for low speed milling of Titanium alloy (TiAl6V4) is also shown in Fig. 3.5. As shown in this figure, the variations of stability limits at lower speeds

are more significant. For example, the stability limit around 200 rev/min increases from 0.12 mm to 0.17 mm, a 40% increase in stability limit.

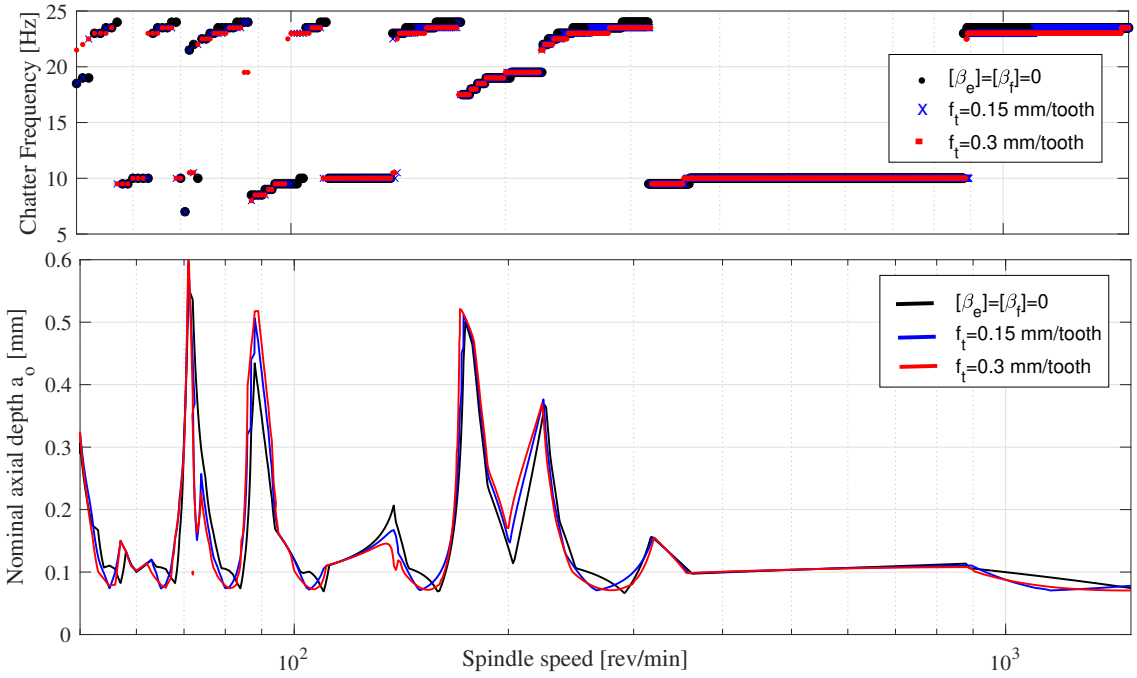

Figure 3.5: Stability limit of 20% down milling of Titanium with KUKA robot; K_{tc} =1835 MPa, K_{rc} =1132 MPa, K_{ac} =280 MPa, K_{te} =25 N/mm, K_{re} =45 N/mm, K_{ae} =10 N/mm, γ=41° , N =4.

3.3 Nonlinearity in regenerative forces

The effect of the nonlinear terms that emerge in the regenerative portion of the cutting forces (Eq. 3.6) is studied by developing numerical simulations in Simulink/MATLAB. The following system of equations is numerically solved to simulate vibrations of the end-effector subjected to nonlinear milling forces:

$$\mathbf{M}\ddot{\mathbf{X}}(t) + \mathbf{C}\dot{\mathbf{X}}(t) + \mathbf{K}\mathbf{X}(t) = \mathbf{F}(t) \tag{3.13}$$

Because the typical feed speed in robotic machining applications is much slower than cutting speed, the effect of inertial forces (i.e. Coriolis and Centrifugal forces) can be neglected [79, 81, 46, 54].The effect of nonlinear inertial forces is neglected in this simulation as well, and the dynamics of the robot structure is assumed to be

linear as described on the left hand side of Eq.5.5. The matrices $\mathbf{M}$, $\mathbf{C}$ and $\mathbf{K}$ are the mass, damping and stiffness matrices of the robot in Cartesian space. These matrices are obtained from the corresponding matrices in joint space ($\mathbf{M}_q$, $\mathbf{C}_q$ and $\mathbf{K}_q$) using the Jacobian of the robot, $\mathbf{J}$ [99]:

$$\mathbf{M} = \mathbf{J}^{-T}\mathbf{M}_q\mathbf{J}^{-1}\,,\ \mathbf{C} = \mathbf{J}^{-T}\mathbf{C}_q\mathbf{J}^{-1}\,,\ \mathbf{K} = \mathbf{J}^{-T}\mathbf{K}_q\mathbf{J}^{-1} \tag{3.14}$$

The stiffness and damping matrices in joint space are considered as diagonal matrices of joint stiffness and damping values, respectively. The mass matrix is a function of the inertia of the robot links and joint coordinates [99]. It is assumed that the robot vibrates in a small range of joint angles, so that the robot posture is invariant. Hence, the mass matrix can be considered as a constant matrix.

3.3.1 Numerical simulation results

Down-milling of Titanium alloy with Staubli TX200 robot is considered. Six degrees of freedom are considered to model the dynamics of the robot as it has six revolute joints. The inertial parameters of the links are derived from the CAD model of the robot to calculate the mass matrix in joint space [99]. Then, the stiffness and damping matrices in joint space are identified in two steps. First, the joint stiffness values are selected such that the square roots of the eigenvalues of $\mathbf{M}_q^{-1}\mathbf{K}_q$ match with the measured natural frequencies of the system. The natural frequencies are identified by performing experimental modal analysis. The FRFs are measured using impulse hammer test and the peaks of the measured FRFs are selected as natural frequencies. In the second step, the damping matrix is identified through the comparison of the magnitudes of the measured and simulated FRFs. Since the measured FRFs are defined in Cartesian space, the simulated FRFs need to be calculated in this space as well. Therefore, the identified system matrices in joint space are transformed to the Cartesian space using the relations in Eq. 3.14. Then, the simulated FRF for a given damping matrix is calculated as follows:

$$\mathbf{H}(\omega) = \left(\mathbf{K} - \mathbf{M}\omega^2 + i\omega\mathbf{C}\right)^{-1} \tag{3.15}$$

The joint damping values are obtained such that the simulated FRFs using Eq. 3.15 fit the measured FRFs. Using the full Jacobian matrix, the system matrices in Cartesian space are obtained as follows:

$$\mathbf{M} = \begin{bmatrix} 415.9 & 30.8 & 15.2 & 1.7 & 42.6 & -129.7 \\ 30.8 & 1571 & 330.8 & -17.9 & -0.4 & 2.1 \\ 15.2 & 330.8 & 397.4 & 36.2 & 0.5 & -3.9 \\ 1.7 & -17.9 & 36.2 & 16.6 & 0.3 & -1.7 \\ 42.6 & -0.4 & 0.5 & 0.3 & 22.1 & -56.1 \\ -129.7 & 2.1 & -3.9 & -1.7 & -56.1 & 175.8 \end{bmatrix} \text{(kg)}$$

$$\mathbf{K} = \begin{bmatrix} 329.9 & 46.5 & 5.1 & 0.2 & 193.2 & 435 \\ 46.5 & 2895 & 281.8 & -182.3 & -0.2 & 7.8 \\ 5.1 & 281.8 & 345.8 & 108.2 & -2 & 0.01 \\ 0.2 & -182.3 & 108.2 & 124.8 & 1.3 & -6.3 \\ 193.2 & -0.2 & -2 & 1.3 & 197.4 & -351.4 \\ 435 & 7.8 & 0.01 & -6.3 & -351.4 & 778 \end{bmatrix} \times 10^4 \text{(N/m)}$$

$$\mathbf{C} = \begin{bmatrix} 4713 & 134 & 20 & 17 & 2004 & 4616 \\ 134 & 12075 & 1147 & -1061 & -17 & 83 \\ 20 & 1147 & 1716 & 696 & 12 & 0.1 \\ 17 & -1061 & 696 & 12 & 19 & -63 \\ 2004 & -17 & 12 & 19 & 1978 & -3527 \\ 4616 & 83 & 0.1 & -63 & -3527 & 7830 \end{bmatrix} \text{(N.s/m)}$$

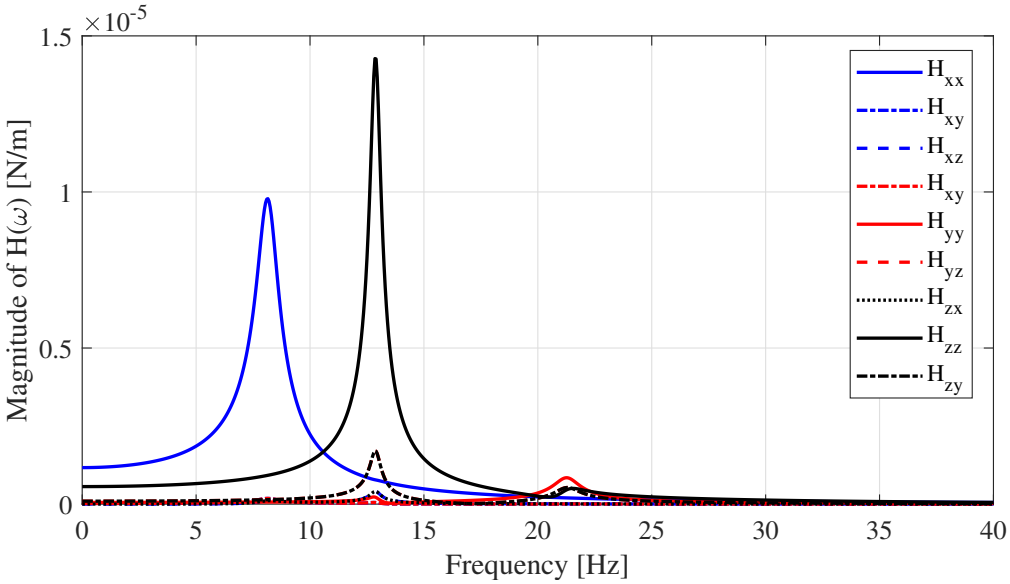

Figure 3.6: Simulated direct and cross FRFs of the Staubli TX200 robot.

The simulated FRFs are presented in Fig. 3.6. Note that substituting the above 6×6 system matrices into Eq. 3.15 results in a 6×6 transfer function matrix which

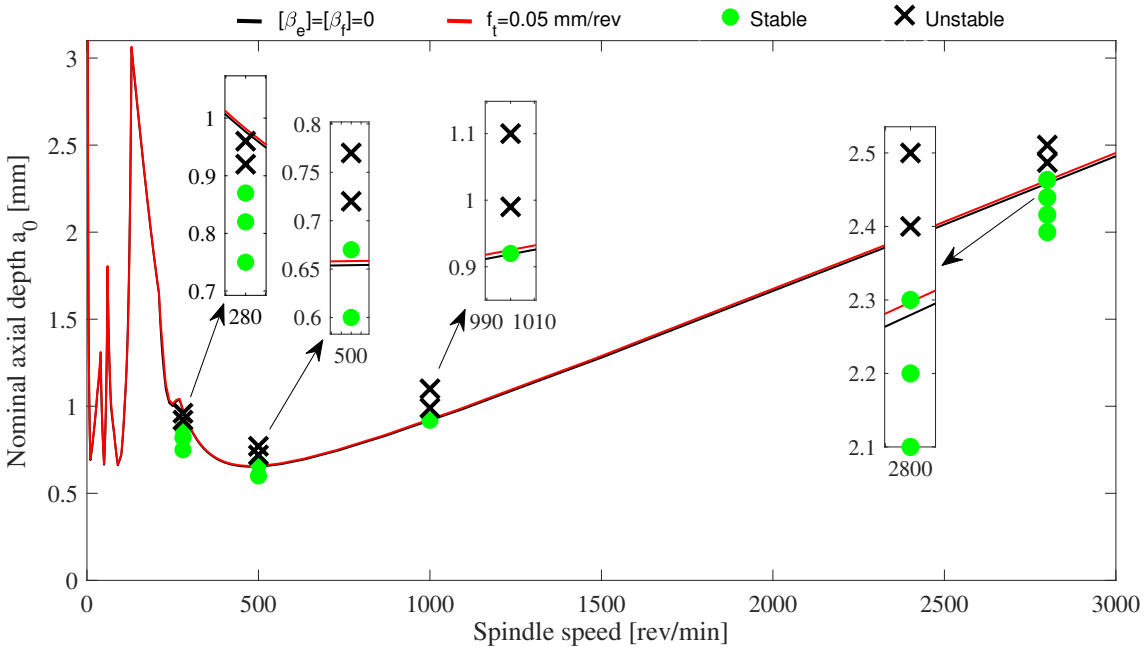

Figure 3.7: Stability limit of 20% down milling of Titanium with Staubli robot; K_{tc} =1835 MPa, K_{rc} =1132 MPa, K_{ac} =280 MPa, K_{te} =25 N/mm, K_{re} =45 N/mm, K_{ae} =10 N/mm, γ=50° , N =4.

includes FRFs between torques and angular displacements as well. In Fig. 3.6, only the force-displacement FRFs are shown. Assuming 20% radial immersion down milling using a 4-tooth milling tool, stability lobe diagrams without considering the nonlinear term is constructed using the method described in Section 3.2.1 and FRFs shown in Fig. 3.6. The resulting diagram is presented in Fig. 3.7. As it can be seen in this figure, the effect of feed and edge forces are negligible in this case, due to low values of feed rate (0.05 mm/tooth) and edge force coefficients. The end-effector vibrations are simulated considering the nonlinear term by numerically solving Eq. 5.5 at different spindle speeds and nominal axial depth of cuts. Stable vibrations are shown with green circles while the black cross marks stand for unstable vibrations.

As shown in Fig. 3.7, the nonlinear term of cutting forces can have both stabilizing and destabilizing effects at different spindle speeds. For example, at spindle speed of 500 rev/min, the stability limit increases from 0.66 mm to 0.70 mm, which is about 6% increase in stability limit, while 9% reduction is observed at 280 rev/min. Figure 3.8 shows the simulated vibrations in X-direction of the end-effector when subjected to linear and nonlinear cutting forces at 0.67 mm nominal depth of cut. The system is unstable if the nonlinear terms are neglected and the vibration amplitude grows

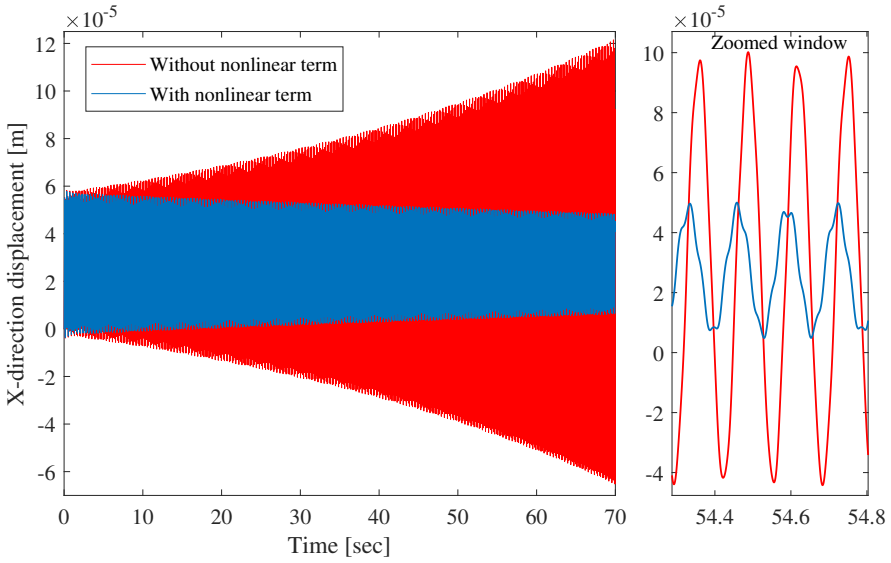

Figure 3.8: Stabilizing effect of the nonlinear term in cutting forces at spindle speed of 500 rev/min and cutting conditions given in Fig. 3.7.

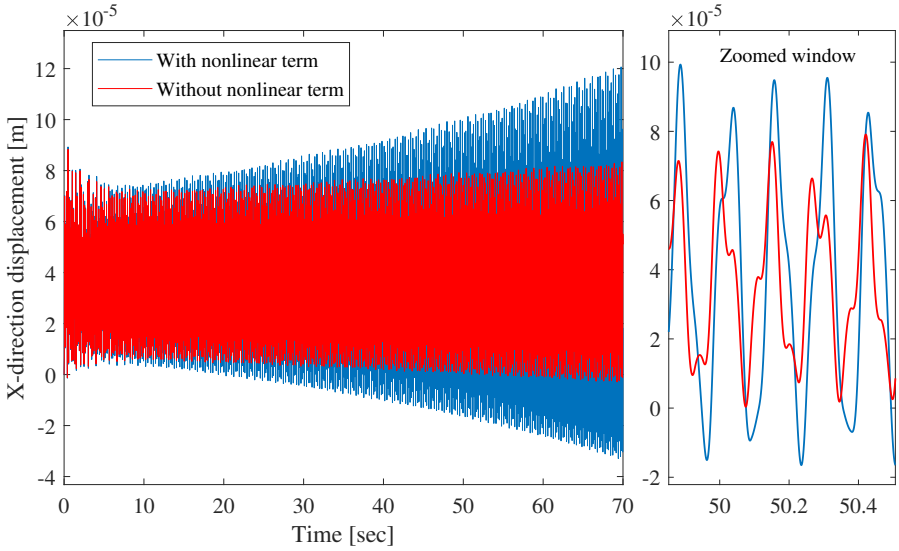

Figure 3.9: Destabilizing effect of the nonlinear term in cutting forces at spindle speed of 280 rev/min and cutting conditions given in Fig. 3.7.

with time. The nonlinear term has damping effect and stabilizes the system. Similar stabilizing effect has been observed at 1000 rev/min and 2800 rev/min. However, the amplitude of simulated vibrations increases when considering the nonlinear term at spindle speed of 280 rev/min and nominal cutting depth of 0.92 mm; as shown in

Fig. 3.9.

3.4 Conclusions

A three dimensional milling force model in robotic milling process was developed to investigate the effect of axial cutting depth modulation due to vibrations in the same direction. It was shown that the modulation of depth of cut leads to additional stiffness-like terms in the equation of motion. These terms arise from the edge and feed-generated forces. In addition, nonlinearities emerge in the regenerative cutting forces model. The effect of edge and feed-generated forces as well as nonlinear regenerative terms on the vibrations stability during robotic milling was studied using numerical examples. Effect of the nonlinear terms of cutting forces on stability was indeed negligible while the additional stiffness-like terms had significant effect on stability of the process, particularly when the robot is in its flexible posture or feedrate is high.

Chapter 4

Investigating structural nonlinearity in robotic machining systems

The fundamental assumption in most of the existing models of vibrations in robotic machining is linearity of the dynamic response at the TCP. In this chapter, the accuracy of this assumption is investigated experimentally. Determining the nonlinearity of system dynamics starts with diagnosing its failure to comply with linearity principles such as scaling and superposition; the experimental investigation of the harmonic response of the structure is commonly used to conduct such a diagnosis. The FRF which fully characterizes the harmonic response of the linear system, is independent of the type and intensity of the excitation. Because the damping and stiffness characteristics of nonlinear structures vary by their deflection, their harmonic response depends on the type and intensity of the excitation force. Leveraging this distinction between linear and nonlinear systems, the extent of the system's nonlinearity is determined by examining the distortion of the FRF from its nominal linear form when the type or intensity of the excitation force changes. This approach is used in this chapter.

4.1 Experimental setup

The experiments in this work were conducted on a KUKA KR90 R3100 robotic arm with a Powertech 400 Hiteco milling spindle that has an HSK 63F holder interface. The configuration of the robotic machining system during the experiments is shown in Fig. 4.1(a).

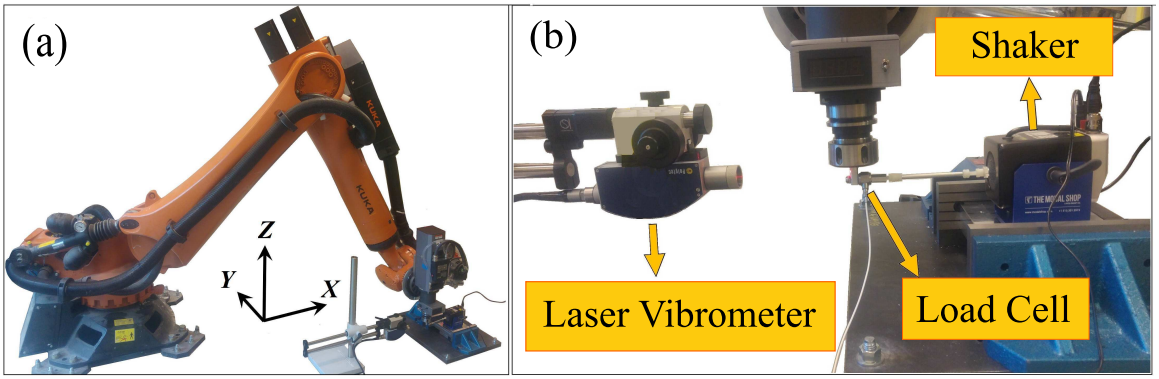

Figure 4.1: (a) Configuration of the robotic machining system during the tests, (b) Vibration excitation and response measurement setup.

A Modal Shop K2007E01 electrodynamic shaker was used to apply harmonic forces at the TCP, as shown in Fig. 4.1(b). The resulting vibrations at the excitation point were measured using a Polytec CLV-2534 laser vibrometer. The sensitivity of the laser vibrometer was set to 0.1 V/mm.s^{-1}. The applied forces were measured at the end of shaker stinger using a PCB 208C01 load cell with 114.6 mV/N sensitivity. Because attaching the load cell at the end of a milling tool is not possible, a 12.7 mm (0.5 inches) diameter solid Aluminum cylinder resembling a milling tool was mounted in the toolholder. As shown in Fig.4.1(b), the shaker was fixed to the ground using a vise to enable delivering higher excitation forces.

4.2 Measurement of Frequency Response Functions

Dynamic compliance of a linear system subjected to harmonic forces is independent of the amplitude of excitation, and its steady-state response is a harmonic motion at the same frequency as the excitation force. Consequently, the harmonic response of a linear system is fully characterized by the unique FRF of the system, which determines the amplitude and phase of the response per unit applied force at each excitation frequency [100]. Measuring the FRF of mechanical structures involves providing various types of excitation force (e.g. sinusoidal, impulse, or random) to the system and measuring the resulting vibrations using acceleration, displacement, or velocity sensors. In linear systems, the measured FRF are independent of the type of or amplitude of the input forces. In nonlinear systems, dynamic compliance depends on the type and amplitude of the input force, and the steady-state response to

harmonic excitation may include super or subharmonics of the excitation frequency as well. Because of these characteristics, the measured FRF of systems with significant nonlinearities strongly depend on the type and amplitude of the excitation force. The systematic change (or distortion) of the measured FRF as the type or amplitude of the input force changes can, therefore, be used as an indicator of nonlinearities in the structure's dynamics.

Compared to random or impulse excitation, measuring FRF using sinusoidal excitation is advantageous in detecting nonlinearities, because arbitrary levels of force at isolated frequencies can be applied on the structure [51, 101]. This advantage of harmonic excitation enables measuring FRF at various constant excitation or response amplitudes, which could then be used to detect and identify the nonlinearity of the structural dynamics.

The direct FRF were measured at the TCP of the robot by applying a harmonic excitation with constant amplitude in one of the Cartesian directions (X, Y, or Z) and measuring the resulting vibrations in the same direction. Figure 4.2 shows a sample of the measured input force and the resulting displacement signals– both in X-direction. The excitation force, shown in part (a) of the figure, is a slowly varying sine sweep with an approximately constant amplitude of ∼14 N and frequency that increases linearly from 1 Hz to 30 Hz at a constant rate of 6 Hz/min. The sweep rate of the frequency was chosen according to ISO 7626 [102] recommendation to minimize the effect of transient response. As shown in the figure, within the first few seconds of the test, the force amplitude reaches the set value (∼14 N) and then remains almost constant for the entire swept frequency range. Close to resonance frequencies, negligible force dropouts occur due to impedance mismatch between the shaker and the structure. Clear response amplifications are observed close to resonance frequencies in the resulting vibrations shown in part (b) of the figure. The FRF under slow sinusoidal sweep can be estimated as the ratio of the auto Power Spectral Density (PSD) of the response, S_{XX}, and the cross PSD of the input and response, S_{XF} [102, 101]:

$$H_1(\omega) = \frac{S_{XX}(\omega)}{S_{XF}(\omega)} \tag{4.1}$$

Alternatively, the FRF can be defined as the ratio of cross PSD of the input and response, S_{FX}, and the auto PSD of the input force, S_{FF} [102, 101]:

$$H_2(\omega) = \frac{S_{FX}(\omega)}{S_{FF}(\omega)} \tag{4.2}$$

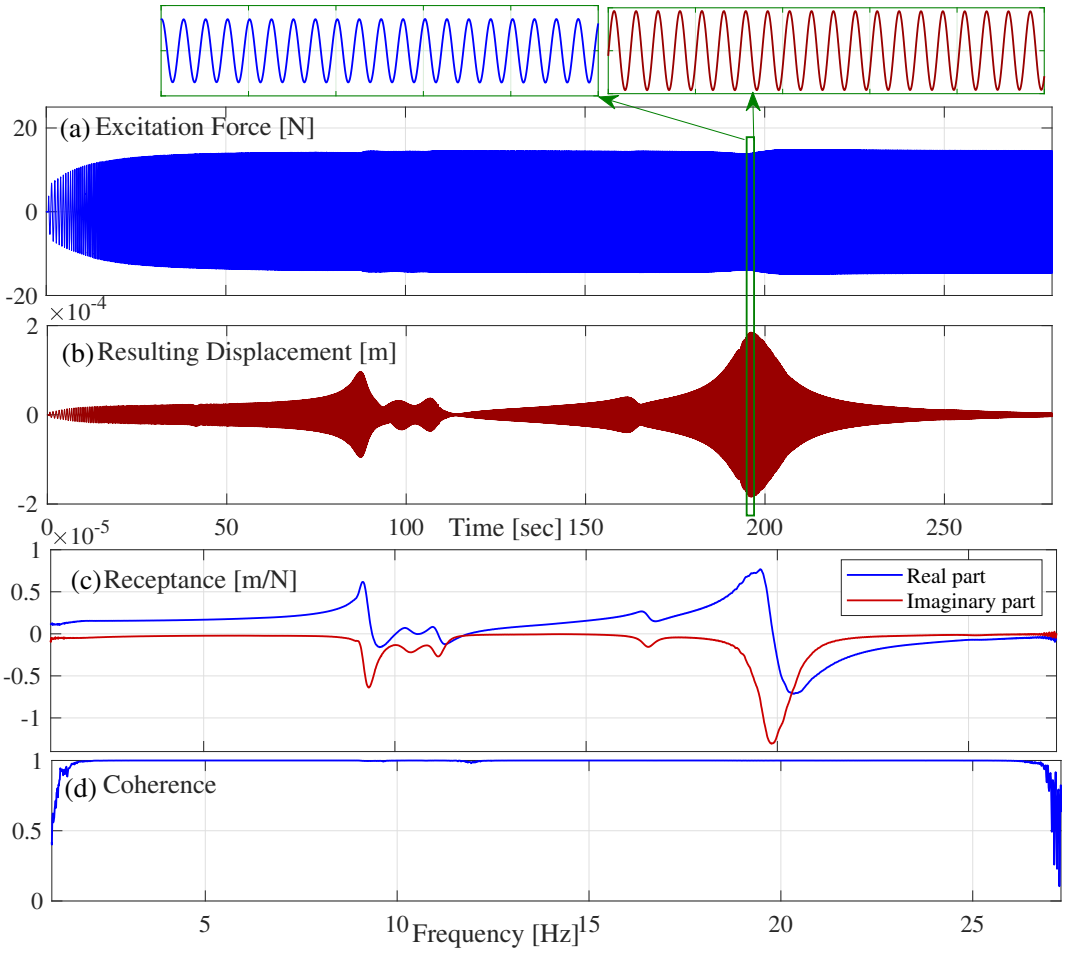

Figure 4.2: Constant force FRF measurement. (a) applied sinusoidal force with constant ∼14 N amplitude and slowly varying frequency between 1 and 30 Hz with a linear sweep rate of 6 Hz/min. (b) corresponding response measured at the excitation point, (c) resulting first-order FRF, and (d) Coherence function.

The formulation in Eq.5.13 reduces the effect of noise in the input signal and the formulation in Eq.4.2 reduces the effect of noise in the output signal. For negligible input and output signal noise levels, H_1 and H_2 yield similar estimates of the FRF. Coherence Function($C(\omega)$), defined as the ratio of H_2 and H_1, is therefore used as an indicator of the level of randomness in the measured FRF:

$$C(\omega) = \frac{H_2(\omega)}{H_1(\omega)} \tag{4.3}$$

Coherence function of the measurement in Fig. 4.2 is presented in part (d) of the figure. Coherence is close to 1 in most of the swept frequency range, indicating near-

identical results from H_1 and H_2 estimation of FRF. The drop of coherence at around 12 Hz is associated with the low signal-to-noise ratio at the antiresonance frequency. Considering that both H_1 and H_2 estimations lead to similar FRF, the arithmetic average of the two estimations are used to represent the FRF in this work:

$$H(\omega) = \frac{1}{2}\left(H_1(\omega) + H_2(\omega)\right) \tag{4.4}$$

The FRF computed using the input and output signals in Fig. 4.2 is shown in part (c) of the figure. Auto and cross PSD of the input and output signals were estimated using Welch's method. Each signal was divided into eight segments and a Hamming window with 50% overlap was applied on each segment to reduce the effect of leakage [103].

In general nonlinear systems, the response to a harmonic excitation comprises oscillations at the frequency of excitation as well as its sub and superharmonics, but the FRF computed using Eqs. 5.13 and 4.2, consider only the components of the response at the excitation frequency, i.e. only the first term in the harmonic balance solution of the nonlinear response [104]. These FRF are therefore referred to as the first-order FRF of the system. Detailed discussions about higher-order FRF and their application in the identification of nonlinear structural dynamics are available in [104, 105, 101].

As described in Fig. 4.2, in this work the amplitude of excitation force is kept constant for the entire swept frequency range. This approach is known as constant-force sine sweep. Alternatively, in a constant-response approach, the force amplitude could be manipulated during the sine sweep to keep the amplitude of response constant. The constant-response approach is usually preferred over constant-force because standard modal curve fitting methods [51] can be applied on the measured FRF to identify the dynamics of the nonlinear system when it is linearized around the harmonic response with the applied constant amplitude. In the constant-force approach, because the amplitude of the response is much higher close to the resonance frequencies, each point on the resulting FRF contains information about the system when it is linearized around a different amplitude. Consequently, linear modal curve fitting methods cannot be applied on constant-force FRF and nonlinear modal analysis methods must be used. Nonetheless, the constant-force approach is implemented in this work because of the rather complex feedback control systems that are needed to maintain the response at a constant level. Modal parameters of the linearized systems are extracted from

constant-force FRF using the NCMA method explained in Section 4.3.

4.2.1 Effect of force amplitude on First-order FRF

A set of constant-force measurements were conducted using sine sweep excitation with different force amplitudes. The FRF corresponding to each force level was then calculated using Eq. 4.4. Figure 4.3(a) shows the FRF resulting from the sine sweep tests in Y-direction. As the force amplitude increases from 4.2 N to 16.5 N, the resonance peaks and the corresponding frequencies at around 9 Hz and 17 Hz consistently decrease. These systematic changes in the resonance peak indicate the presence of considerable nonlinearities in the structure. Similar experiments were performed to measure FRF in X and Z directions, and the resulting FRF are shown in Figs. 4.3 (b) and (c), respectively. Similarly, the magnitudes of FRF in X and Z directions decrease by increasing the force level, although the reductions are not as drastic as in Y direction. The observed differences in the FRF can lead to substantial changes in the predicted SLD and SLE diagrams in robotic machining operations. For example, Fig. 4.4 shows the SLD of the robotic machining system described in Chapter 3 when the FRF in Fig. 4.3 are employed in the frequency domain solution. The SLD obtained by using both low-force (4$\sim$5 N) and high-force (15$\sim$16 N) FRF are shown in this figure to highlight the extent of the variations that may occur in the predicted SLD when FRF of various force levels are used in the solution.

Also shown in Fig. 4.3 are the corresponding direct FRF measured using impulse hammer tests, where a Kistler 9726A5000 hammer was used to apply the impulse excitation. While the force capacity of the shaker was limited to about 17 N, the peak impulse force of above 50 N was achieved in the hammer test. The FRF obtained using the shaker test deviate from those of the hammer impulse test, indicating that the FRF that are usually measured using impulse tests may not be representative of the true dynamics of the system under various operational loads. The frequency resolution in the impulse test was set to 0.5 Hz. Considering that the flexible vibration modes of the robot are typically below 30 Hz [8], the resolution of 0.5 Hz is not fine enough to accurately capture the shape of the resonance peak. This shortcoming is more obvious in Figs. 4.3(a) and (b) for the modes located around 9 Hz and 21 Hz, respectively. Finer resolutions could not be achieved in hammer tests, because a lower resolution requires recording a longer impulse response which leads to poor signal-to-noise ratio and thus bad coherence. In addition to not being able to control

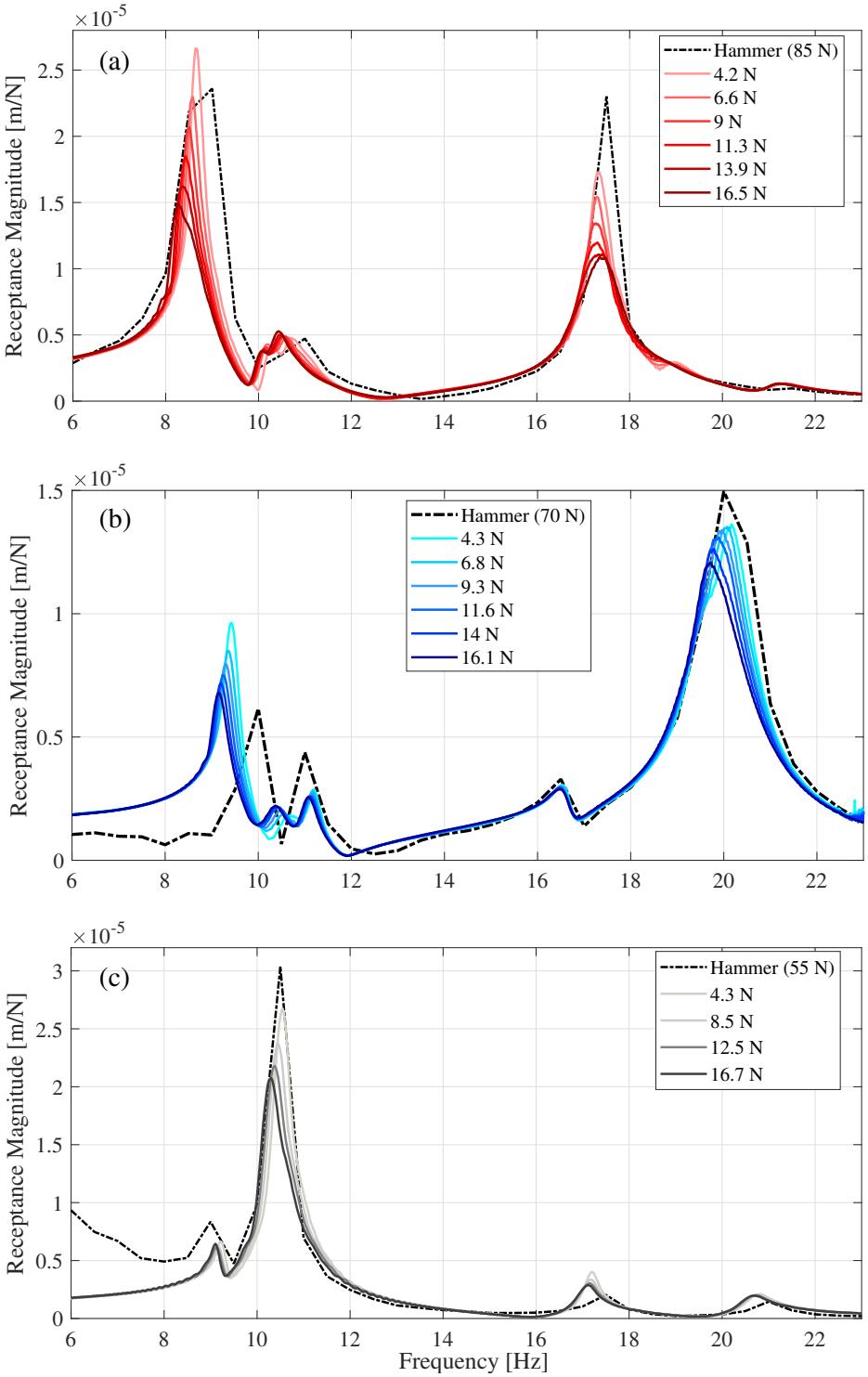

Figure 4.3: Effect of excitation force level on receptances in (a) Y, (b) X and (c) Z directions.

the amplitude and frequency of excitation, the low-frequency resolution in impulse excitation is another reason for applying sinusoidal excitation to measure the FRF of robotic machining systems.

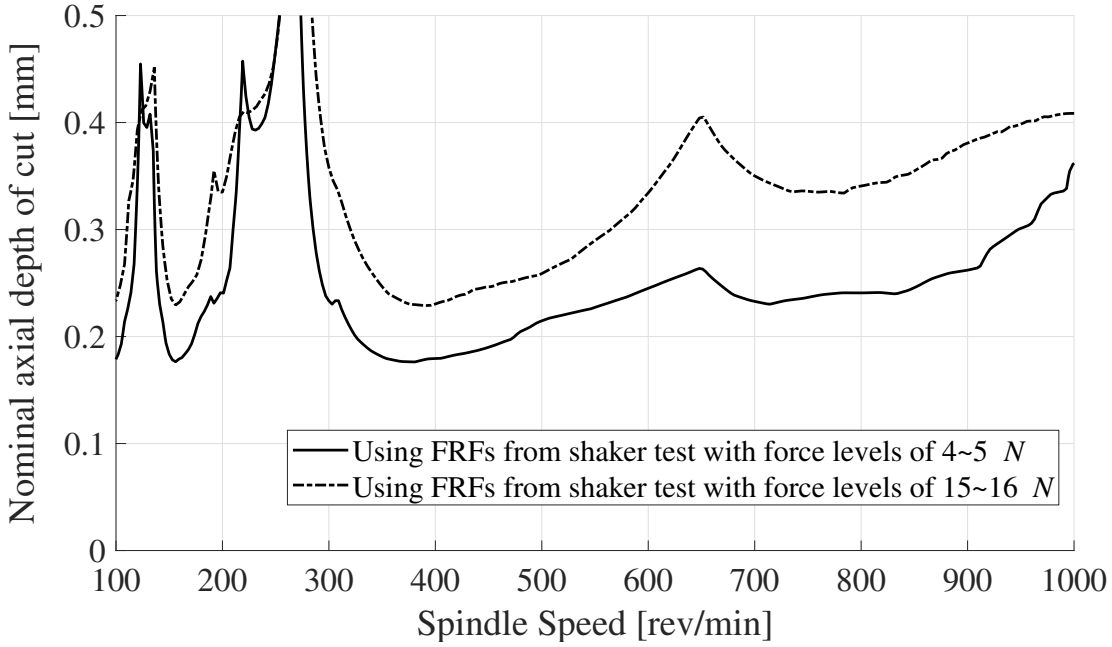

Figure 4.4: Stability Lobe Diagrams (SLD) of the milling system in Chapter 3 when the FRF shown in Fig. 3 are used in the solution. Half-immersion downmilling of Al 6061 with a two-fluted cutter is assumed.

4.2.2 Backward and forward sweep

The FRF in Fig. 4.3 were obtained by sweeping the frequency of excitation from 1 Hz to 30 Hz, i.e. forward sine sweep. Figure 4.5 shows the excitation force and the corresponding response in X-direction when backward sweeping of frequency is used, i.e. the excitation frequency decreasing from 30 Hz to 1 Hz. The direct FRF were measured in X-direction this time by using backward sine sweep, and the results are compared to the FRF measured using forward sine sweep in Fig. 4.6. Similar force amplitudes are used in forward and backward sweeps. As shown in this figure, small deviations in the magnitude of FRF–particularly around the first peak– are observed when the sweeping direction of the excitation frequency changes. Nevertheless, as the excitation force amplitude increases in both backward and forward sweep tests, a similar trend of systematic FRF variation is observed; the resonance peak and

frequency decrease by increasing the force level. Similar results were obtained for FRF in Z and Y directions, but they are not shown here.

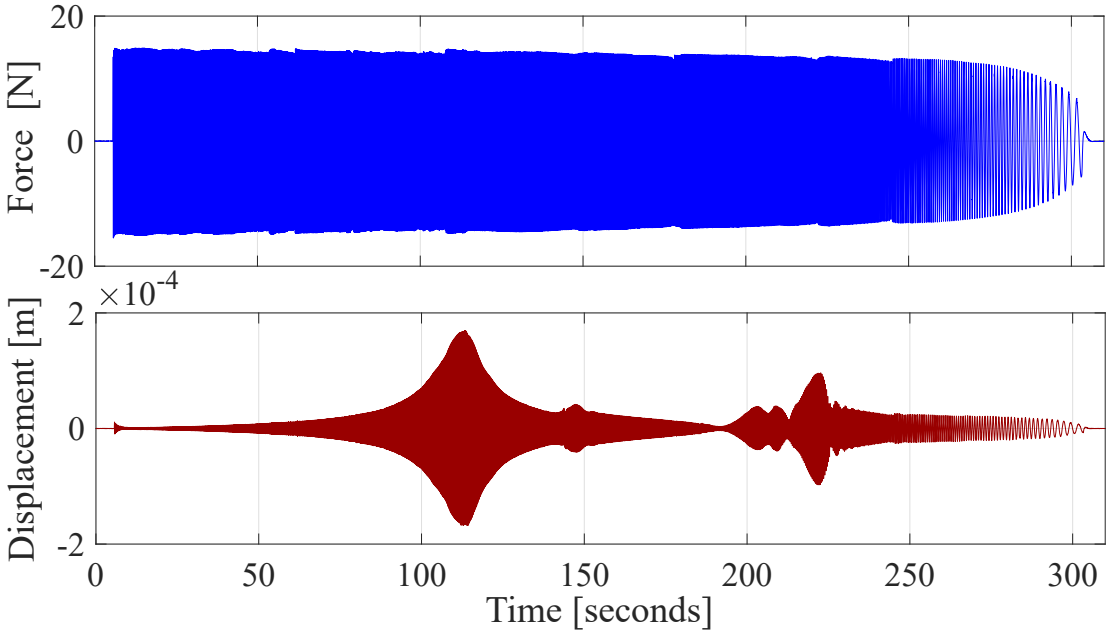

Figure 4.5: The excitation force applied at the TCP in X-direction and the resulting displacement. Frequency of the force is decreasing linearly from 30 Hz to 1 Hz (backward sweeping).

4.2.3 Excitation at constant frequency

The homogeneity property of linear systems requires the amplitude of their response to unit harmonic force to remain constant regardless of the amplitude of the excitation. In this section, the linearity of the TCP dynamics is further investigated by exciting the robot TCP using a sinusoidal force with constant frequency but a linearly increasing amplitude. For instance, Fig. 4.7(a) shows a sinusoidal force with 16 Hz frequency and amplitude that increases linearly from zero to 20 N over 153 seconds. This force was applied at the TCP in Y-direction and the resulting response, measured in the same direction, is shown in part (b) of the figure. Similar to the excitation force, the response is also a harmonic motion with a 16 Hz frequency and a linearly increasing amplitude. The excitation and response at this frequency satisfy the homogeneity property of linear systems. Such tests were performed for several excitation frequencies close to the resonance peaks, and in what follows, some cases where the dynamic response demonstrated clear nonlinearities are presented.

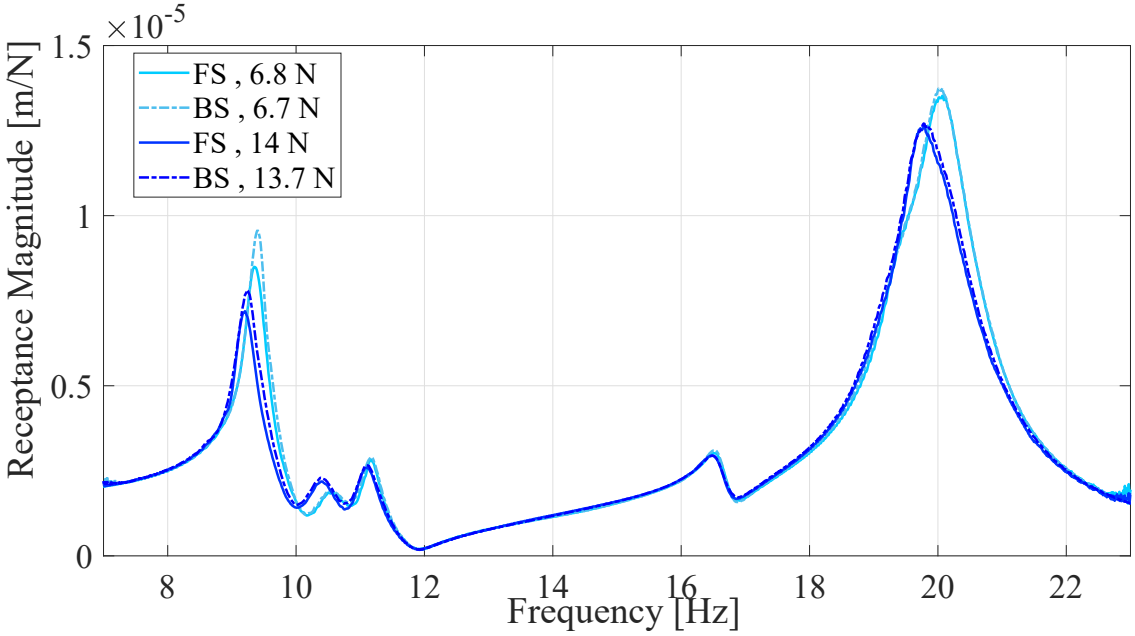

Figure 4.6: Comparison of FRF at TCP in X direction obtained from measurements with constant force level and forward (FS) and backward sweeping (BS) of the excitation frequency.

Figures 4.8(a) and (b) show the results of the experiments conducted at 8.4 Hz. The excitation forces in these cases are not shown because they are similar to the force in Fig. 4.7, and only the positive part of the measured displacement is shown for better visibility. As shown in part (a) of the figure, the response amplitude increases consistently with the force during the low-force part of excitation, which is marked as region I. The response, however, increases at a much lower rate after the force amplitude reaches a point between 10 and 12 N, i.e. the start of region II in the figure. Similar behavior is observed for the case of decreasing force amplitude (sweep down) shown in Fig. 4.8(b). Unlike the test conducted at 16 Hz, shown in Fig. 4.7, the dynamics of the system at 8.4 Hz reveals a clear violation of homogeneity. The system's response was also investigated in Y-direction at a frequency close to the second mode at 17.4 Hz, and the results are shown in Fig. 4.8(c) and (d). Although the displacement amplitude increases linearly with the force, three ranges (marked as I, II, and III) with different rates of amplitude increase can be observed. Small jumps also are observed at the intersections of the three ranges in Fig. 4.8(c). The transitions of the vibration amplitude between regions I, II, and III in Fig. 4.8(c) could be indicators of continues bifurcations of the harmonic response of the nonlinear system as the amplitude of excitation changes.

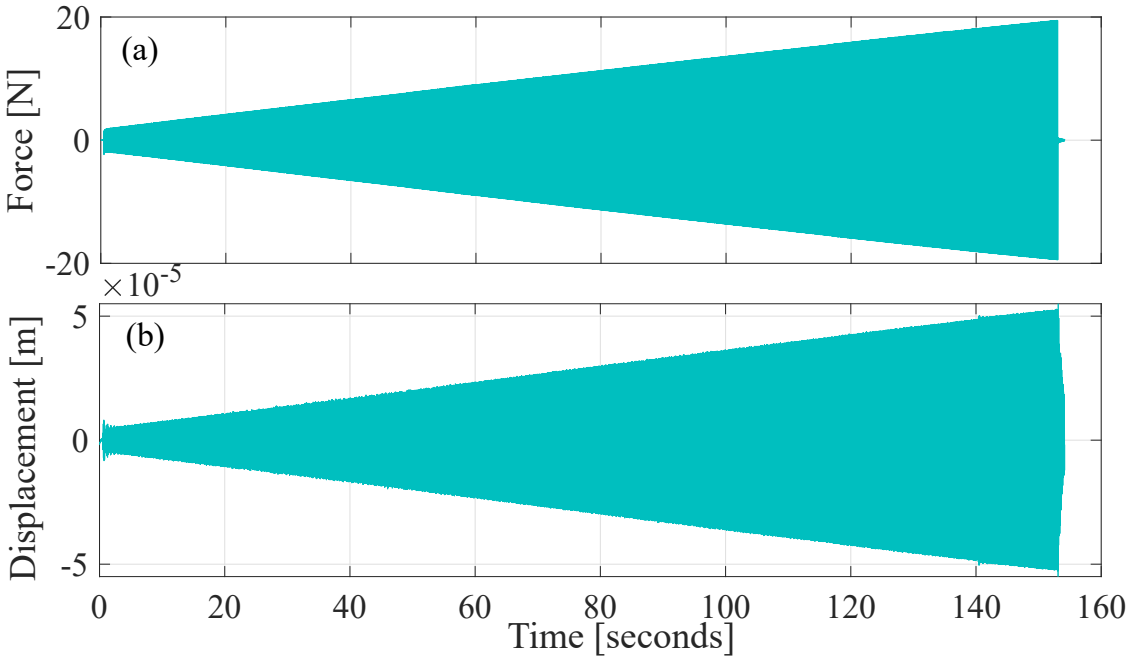

Figure 4.7: Linear response of the robot to sinusoidal forces in Y direction at constant frequency of 16 Hz and increasing amplitude.

4.3 Nonlinear Complex Mode Analysis (NCMA)

As discussed in Section 4.2, first-order FRF measured using constant-response approach represent the FRF of the system when it is linearized in the vicinity of the tested constant response amplitude, and therefore standard linear modal curve fitting methods [51] can be used to determine the modal parameters of the linearized system. This is not the case in constant-force approach, because the amplitude of vibration near resonance frequencies is much higher and therefore each point on the FRF represents a linearized system around a different vibration amplitude. Consequently, linear modal curve fitting methods are not applicable for constant-force FRF. Nonlinear Complex Mode Analysis is usually used to study structures with non-proportional damping and structures that have amplitude-dependent natural frequency and damping loss factors [101]. In this method, modal parameters associated with each vibration amplitude are extracted from the constant-force FRF, and then empirical relations are established between the identified modal parameters and the vibration amplitude.

Suppose ω_1 and ω_2 are the frequencies of two data points with similar receptance magnitudes on the two sides of the resonance peak of a constant-force FRF. Neglecting

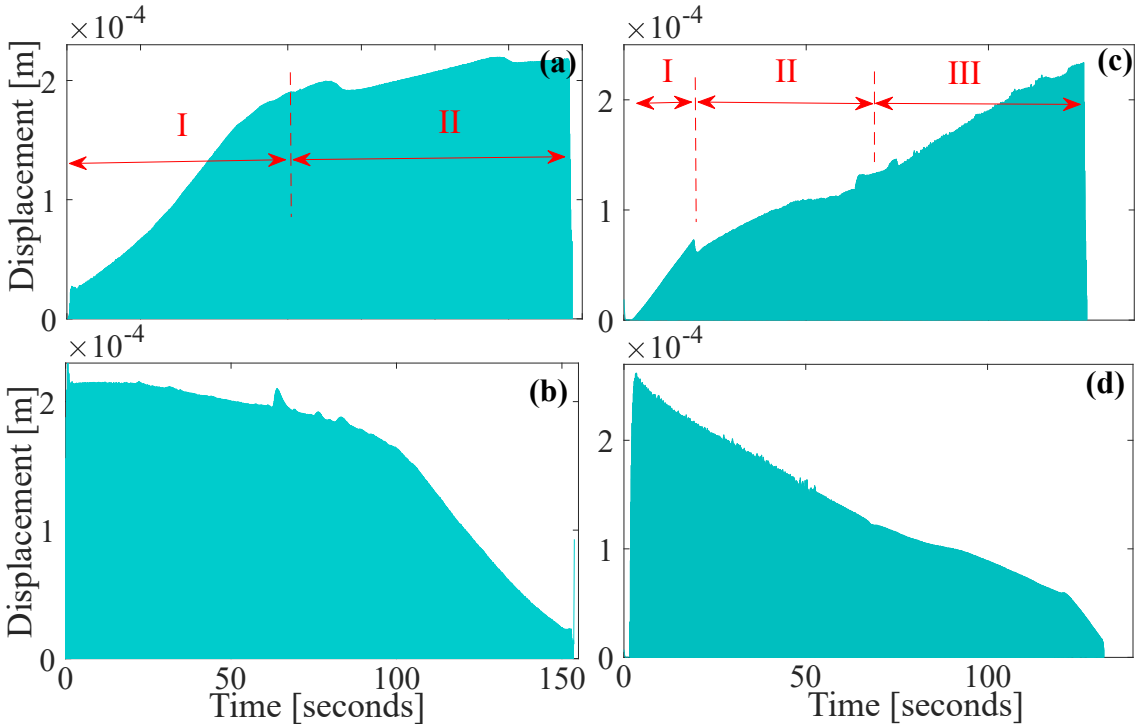

Figure 4.8: Response of the robot to sinusoidal forces in Y direction at constant frequency of (a) 8.4 Hz and increasing force (b), 8.4 Hz and decreasing force, (c) 17.4 Hz and increasing force, (d) 17.4 Hz and decreasing force.

the contribution of other modes to the dynamics in the vicinity of the resonance peak, the FRF of the system that is linearized around the amplitude of vibration at ω_1 and ω_2 is expressed in terms of its modal constants as follows [51, 101]:

$$H(\omega_1) = \frac{A_r + iB_r}{\omega_r^2 - \omega_1^2 + i\eta_r\omega_r^2} \tag{4.5}$$

$$H(\omega_2) = \frac{A_r + iB_r}{\omega_r^2 - \omega_2^2 + i\eta_r\omega_r^2} \tag{4.6}$$

The parameters A_r and B_r are the modal constants, ω_r is the natural frequency and η_r is the damping loss factor of the linearized system. These four constants are obtained by solving the four equations arising from the two complex equations, i.e. Eqs. 4.5 and 4.6. The resulting parameters describe the modal parameters of the linearized system.

Nonlinear Complex Mode Analysis is applied to the constant-force FRF presented in Fig. 4.3 to determine the amplitude-dependent modal frequencies and loss factors of the robotic machining setup. Figure 4.9(a) shows the variation of the frequency and

damping of the first flexible mode in the Y direction. Consistent with the observation in Fig. 4.3(a), the modal frequency decreases by increasing the force amplitude, while the damping loss factor increases. Additionally, when the excitation force amplitude is lower, the variation of modal frequency and damping loss factors as the receptance amplitude increases is much smaller than when the excitation force is high. For example, in Fig.4.9(a), when the excitation force is constant at 4.2 N, in receptance amplitudes higher than 10 μm/N, modal frequency and damping loss factor remain relatively constant at 8.7 Hz and 0.033, respectively. In the same figure, as the amplitude of excitation force increases, the dependency of modal parameters on the response amplitudes become more pronounced. This observation indicates that the nonlinearity of the structure becomes more influential as the operational forces and the resulting deflections increase.

Figures 4.9 (b) and (c) show the results of similar analyses conducted on the flexible modes in X and Z directions, respectively. In both modes and all force levels, natural frequency and loss factor change by vibration amplitude. This effect is especially significant for the mode in the Z direction. Similar to the mode in Y-direction, the dependency of frequency and damping on the response level become stronger by increasing the force amplitude. Therefore, it is safe to conclude that the nonlinearity of the system increases by increasing the excitation force and thus the vibration amplitude.

4.3.1 Variation of modal paramters

As demonstrated in the previous section, modal frequencies and damping loss factors change systematically as the force and vibration amplitudes increase. In most of the cases shown in Fig. 4.9, the variations of ω_r and η_r with respect to receptance amplitude can be approximated by a polynomial function. So, it is possible to establish an empirical model that predicts the modal parameters of the systems linearized around arbitrary force and vibration amplitudes. In this section, as a case study, an empirical model is developed to describe the variations of the frequency and damping loss factors of the flexible mode in Y-direction (Fig. 4.9(a)).

In each excitation force amplitude, F, the variation of ω_r with respect to the receptance magnitude is estimated using a quadratic function of the following form:

$$\omega_r = a\left(\frac{X}{F}\right)^2 + b\left(\frac{X}{F}\right) + c \tag{4.7}$$

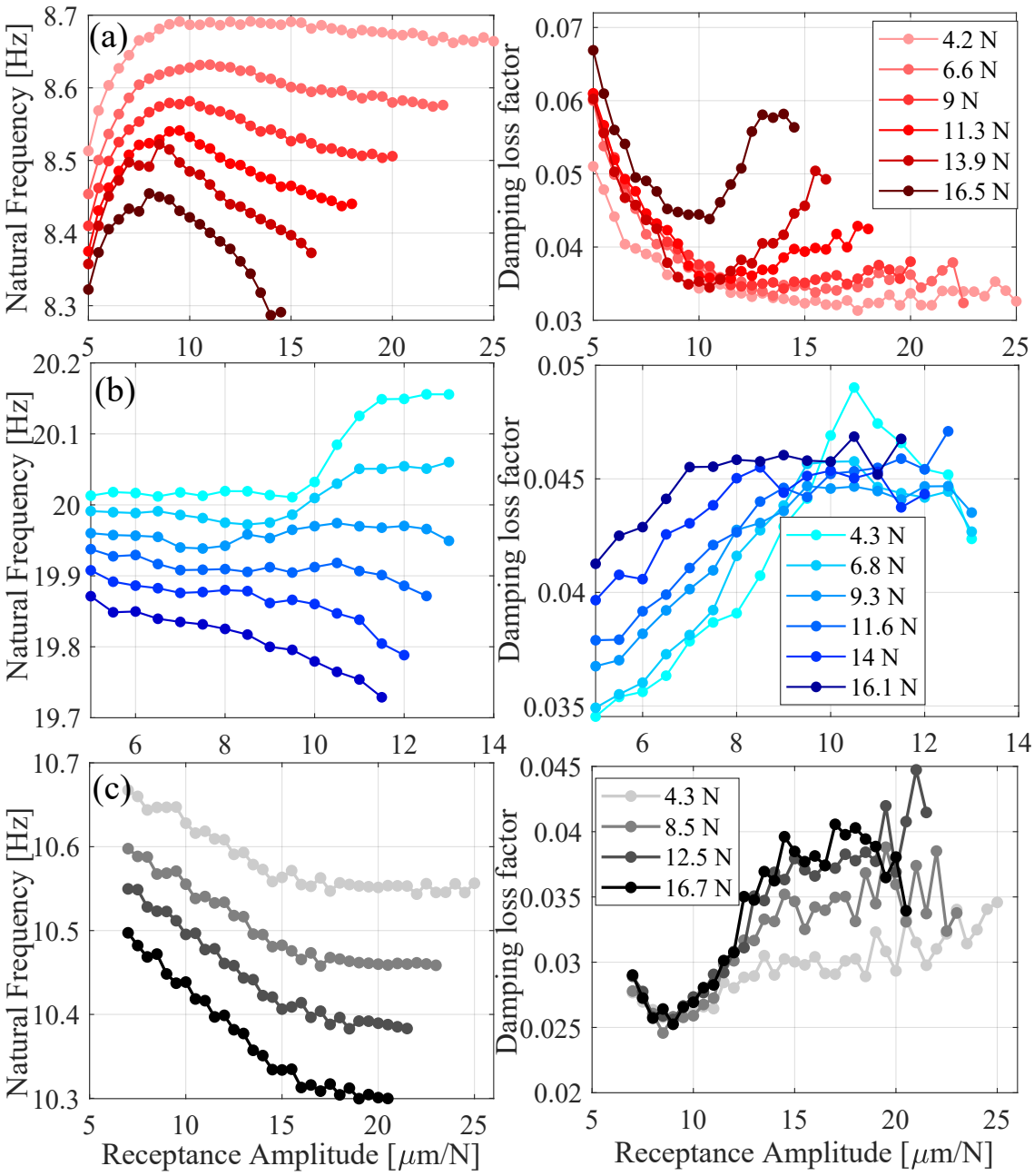

Figure 4.9: Variation of natural frequency and loss factor of the flexible modes in (a) Y, (b) X and (c) Z directions.

where X and F are the amplitudes of the response and the excitation force, respectively, and consequently $\frac{X}{F}$ is the magnitude of the receptance, $|H|$. The coefficients of the quadratic function (a, b,and c) are determined using Least Squares approximation, and the resulting functions in each of the force amplitudes are shown in Fig. 4.10(a). In this figure, the results of only three force levels are shown for better visibility. These equations define the relationship between ω_r and receptance amplitude, $|H|$. The coefficients a, b and c are force-dependent and vary for each excitation force amplitude. These coefficients are then plotted in terms of the excitation force level. As shown in this figure, a, b and c coefficients vary linearly with respect to the force amplitude and therefore they can be estimated using the linear functions shown in the figure. As a result, the following functions are established to describe the modal frequency at each force and response amplitude.

$$\begin{aligned}\omega_r = (-3.7e8F + 1.3e9)\left(\tfrac{X}{F}\right)^2 + (5.6e3F - 6.3)\left(\tfrac{X}{F}\right) \\ + (-0.036F + 8.7)\end{aligned} \tag{4.8}$$

Similarly, a quadratic function is used to model the variation of η_r of the first mode in Y-direction (Fig. 4.9(a)). The constants a, b and c are obtained for each measurement at the given force level, as shown in Fig. 4.10(b). The variation of the constants with the force amplitude is modelled using linear functions. As a result, the following equation is derived to estimate the damping loss factor at different force levels and vibration amplitudes:

$$\begin{aligned}\eta_r = (6.1e7F - 2.4e8)\left(\tfrac{X}{F}\right)^2 + (-1.1e3F + 2.1e3)\left(\tfrac{X}{F}\right) \\ + (0.005F + 0.039)\end{aligned} \tag{4.9}$$

Similar empirical models can be derived to describe the variation of the other modal parameters of linearized systems.

4.4 Conclusions

The linearity of the structural dynamics of a machining robot was investigated by measuring its response to harmonic excitations. Based on the experimental results, it was concluded that the robot's vibrations under dynamic loads are strongly affected by nonlinearities in its structure. Nonlinear Complex Mode Analysis was used to identify the modal parameters of the nonlinear system when its dynamics is linearized around a harmonic oscillation with a constant amplitude. The identified modal parameters

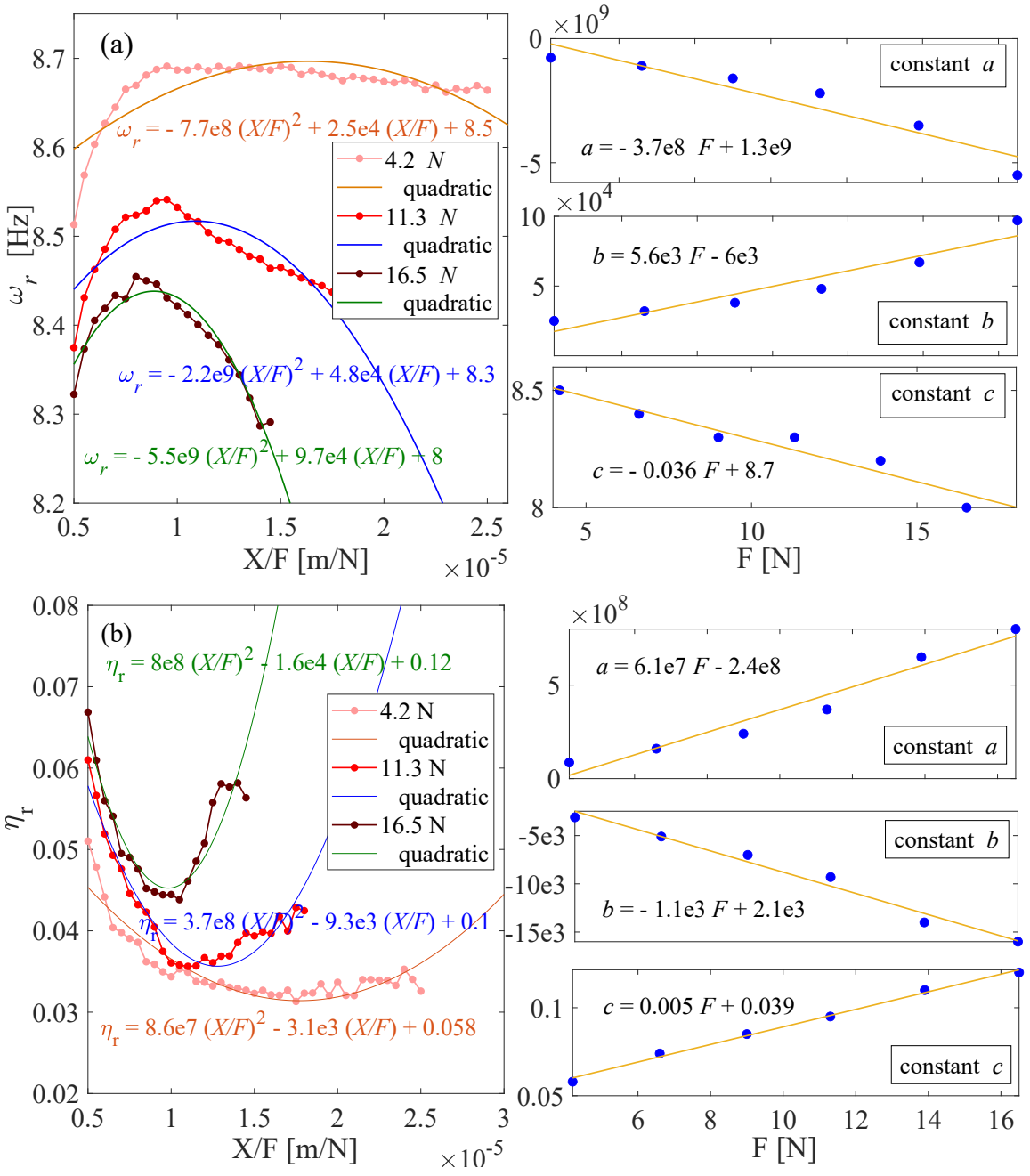

Figure 4.10: Empirical modelling of the variations of a) ω_r and b) η_r with force and receptance amplitudes for the flexible mode in Y direction.

strongly depend on the vibration amplitude around which the system is linearized. As a result, unlike the common machine tool vibration models, using a unique FRF or modal model to describe the dynamics of the machining system regardless of the magnitude of the operational loads, may lead to considerable inaccuracies in modeling vibrations in robotic machining.

Chapter 5

Modeling of the nonlinear vibration response

In the previous chapter, the nonlinearity and its extent in the structural dynamics of machining robot were investigated. The results highlighted the inaccuracies that may be caused by assuming linear dynamics in modeling vibrations of robotic machining, and therefore, the need for considering the nonlinearities of the structural dynamics of industrial robots. This chapter focuses on developing a model to capture the observed nonlinear effects. The TCP vibration response of the KUKA machining robot is modeled using a nonlinear SDOF system. Type of the nonlinearity of the restoring force is first characterized experimentally. The results of this characterization shows that the damping and stiffness components of the restoring force can be approximated by cubic models. Subsequently, the Higher-order FRF (HFRF) of the SDOF system are estimated from step-sine excitation measurements, and the parameters of the nonlinear SDOF system are identified by curve-fitting the resulting HFRF. The accuracy of the presented SDOF modeling approach in capturing the nonlinearity of the TCP vibration response is verified experimentally. It is shown that the identified models accurately predict the variation of the receptance of the nonlinear system in the vicinity of well-separated peaks, but nonlinear coupling around closely-spaced peaks may cause inaccuracies in the prediction of system dynamics.

5.1 Characterization of the nonlinear restoring force

When the nonlinearity of the system is neglected, in the vicinity of the resonance peaks and by assuming well-separated modes, each peak in Fig. 4.3 can be approximated by the FRF of a SDOF system described by the following equation [106]:

$$m\ddot{q}(t) = f_p(t) - kq(t) - c\dot{q}(t)\,; \;\; p, q = x, y, z \tag{5.1}$$

where m, k, and c are modal mass, stiffness, and damping coefficients, respectively, and f_p is the force applied in $p = x, y$ or z direction. Because only direct FRF are studied in this work, $p = q$ will be assumed in the rest of this chapter, but a similar analysis applies to cross FRF where $p \neq q$. The restoring force, which drives the motion towards equilibrium in Eq. 5.1, consists of the linear spring force, $kq(t)$ and the linear viscous damping force, $c\dot{q}(t)$. In the presence of nonlinear dynamics, the restoring force is a general function of the corresponding displacement and velocity and, as a result, the equation of motion is expressed in the following general form:

$$m\ddot{q}(t) = f_q(t) - f_r(\dot{q}, q) \tag{5.2}$$

where $f_r(\dot{q}, q)$ represents the nonlinear restoring force, and the mass m is assumed to remain unaffected by nonlinearities. For simplicity, the following assumptions are made about the restoring force in Eq. 5.2: (a) Because the linear modes are assumed to be well-separated, modal coupling due to the system nonlinearities is also neglected in formulating the restoring force, and (b) restoring force is assumed to include uncoupled velocity-dependent (damping) and displacement-dependent (stiffness) terms, as follows:

$$f_r(\dot{q}, q) = c(\dot{q})\dot{q} + k(q)q \tag{5.3}$$

where $c(\dot{q})$ and $k(q)$ resemble nonlinear damping and stiffness coefficients, respectively. The parametric identification of the restoring force requires a prior knowledge of the composition of the function $f_r(\dot{q}, q)$, which can include piecewise continuous terms to account for backlash and coulomb friction or polynomial stiffness and damping terms to represent hardening or softening effects. Visual inspection of the restoring force is used in this section to determine the types of the prevalent nonlinear terms that should be considered in system dynamics.

If the excitation force, f_q, and the resulting acceleration, $\ddot{q}(t)$, in Eq. 5.2 are

available from measurements, the restoring force can be obtained as follows:

$$f_r(\dot{q}, q) = f_q(t) - m\ddot{q}(t) \tag{5.4}$$

where m is assumed to be known from the linear modal analysis of impulse-hammer test results. As an example, the excitation forces and the resulting velocity signals, both in Y-direction, are used in Eq. 5.4 to determine the restoring force when the system is excited in the vicinity of the resonance peak at 17.5 Hz, and the results are presented in Figs. 5.1 and 5.2. In this measurement, the excitation force was a multi-tone sinusoidal signal with frequencies between 16.8 and 17.8 Hz. The velocity of the resulting vibrations in Y-direction were measured using the LDV, which was subsequently differentiated and integrated numerically to obtain the acceleration and displacement responses, respectively. The linear mass, stiffness, and damping coefficients of this mode were identified from the modal analysis of impulse-hammer FRF as $m = 166$ kg, $k = 2.04e6$ N/m, and $c = 435$ N.sec/m. The measured input force and output acceleration response were used in Eq. 5.4 to determine the restoring force in the system. To isolate the damping component of the restoring force, $c(\dot{q})\dot{q}$ in Eq. 5.4, the computed restoring forces at negligible displacement values ($|q(t)|$ less than 0.1% of maximum deflection) are plotted in Fig. 5.1. Because the displacement values at the points shown in this figure are negligible, the overall restoring force represents $c(\dot{q})\dot{q}$. Similarly, the computed restoring force when the velocity is negligible ($|\dot{q}|$ less than 0.1% of maximum velocity) is shown in Fig. 5.2, which represents the $k(q)q$ component of the overall restoring forces. The blue dots show the estimated restoring force and the red lines show the linear restoring force estimated based on the linear modal parameters. As shown in Fig. 5.1(a), although the estimated restoring force is close to the linear behavior at small velocities ($|\dot{q}(t)| \leq 0.01 m/sec$), it deviates from the linear line as the velocity increases. Part (b) of the figure shows the deviation of the restoring force from the linear approximation. The observation of the restoring force in this plot suggests that the damping term of the restoring force can be approximated using polynomial functions. The yellow line in Fig. 5.1(b) presents a cubic function of velocities (e.g. $c_3\dot{q}^3$) fitted to estimated deviations.

As shown in Fig. 5.2(a), unlike the damping component of the restoring force, the stiffness component remains close to the linear approximation, with small deviations. Nonlinearity is more clear in part (b) of the figure where the deviation from linear estimation is depicted. It is shown that the deviation of the linear stiffness also

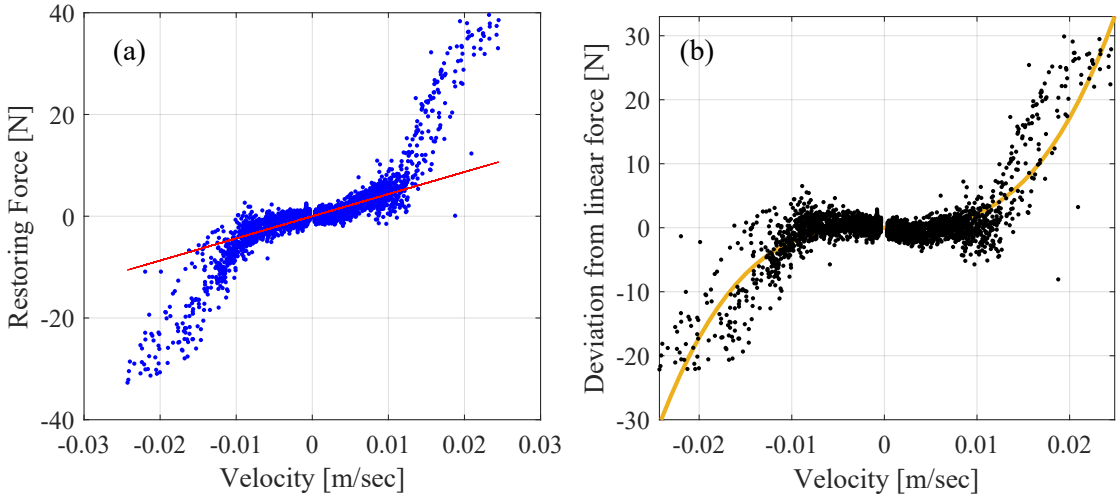

Figure 5.1: Variations of restoring force with velocity at small displacements. (a) Blue dots: estimated restoring force; Red line: approximated linear restoring force. (b) Black dots: deviations from linear approximation; Yellow line: fitted cubic function.

follows a polynomial trend shown by the yellow line ($k_3 q^3$). This behavior resembles softening effect which occurs when stiffness decreases at larger deflections. However, at the displacements larger than 0.6×10^{-4}m, the restoring force does not follow this cubic curve and becomes closer to the linear approximation, i.e. stiffness increases. This change in the stiffness behavior is in agreement with the variation of the resonant frequency as shown in Fig. 4.3(a). The resonant frequency first decreases with the excitation force amplitude, but then increases.

Similar analyses were conducted to determine the variation of the restoring force when the system is excited in the vicinity of the other modes shown in Fig. 4.3. The variation of the damping component of the restoring force in all of the modes is similar to Fig. 5.1. The variation of the stiffness component is also similar to Fig. 5.2, but the deviation from the linear stiffness follows a cubic trend for the entire range of displacements. Therefore, in the next section, cubic nonlinearity is assumed for both damping and stiffness components of the restoring force model. More precise but complicated models can be considered by adding other polynomial terms such as quadratic and higher order terms, as well as the cross terms $q^m \dot{q}^n$. However, the goal here is to develop a model with less complexity which can be implemented in vibration control strategies.

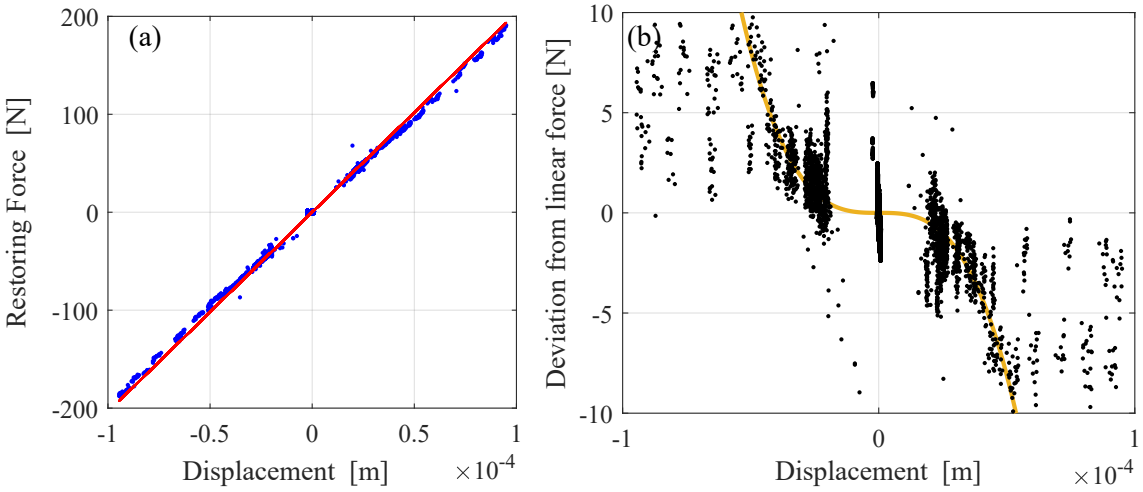

Figure 5.2: Variations of restoring force with displacement at small velocities. (a) Blue dots: estimated restoring force; Red line: approximated linear restoring force. (b) Black dots: deviations from linear approximation; Yellow line: fitted cubic function.

5.2 Identification of the model parameters using Higher-order FRF

Substituting the restoring force in Eq. 5.2 by a combination of linear and cubic stiffness and damping terms leads to the following nonlinear equation of motion in each of the X, Y, and Z directions:

$$m\ddot{q}(t) + c_1\dot{q}(t) + k_1 q(t) + c_3\dot{q}(t)^3 + k_3 q(t)^3 = f_q(t); \qquad q = x, y, z \tag{5.5}$$

In this section, the parameters of the model in Eq. 5.5 are identified by curve-fitting the Higher-order FRF of the system.

5.2.1 Higher-order FRF

The response of the nonlinear SDOF system in Eq. 5.2 can be described by its Volterra series expansion as follows [107]:

$$
\begin{aligned}
q(t) &= \sum_{n=1}^{\infty} q_n(t), \\
q_n(t) &= \int_{-\infty}^{\infty} \cdots \int_{-\infty}^{\infty} h_n(\tau_1, \ldots, \tau_n) f_q(t-\tau_1) \cdots \\
&\quad f_q(t-\tau_n)\, d\tau_1 \cdots d\tau_n
\end{aligned}
\tag{5.6}
$$

where $h_1(\tau_1)$ and $h_n(\tau_1, \ldots, \tau_n)$ resemble the first and higher order impulse response functions of the system, respectively. The higher order impulse response functions of linear systems are zero. Multi-dimensional Fourier transforms of the higher order impulse response functions are known as Higher-order FRF (HFRF) [107], defined as follows:

$$
\begin{aligned}
H_n(\omega_1, \ldots, \omega_n) = \int_{-\infty}^{\infty} \cdots \int_{-\infty}^{\infty} & h_n(\tau_1, \ldots, \tau_n) \\
& \prod_{k=1}^{n} e^{-i\omega_k \tau_k}\, d\tau_1 \cdots d\tau_n
\end{aligned}
\tag{5.7}
$$

A sinusoidal excitation force, $f_q(t)$, with frequency ω and amplitude F can be expressed in the following complex exponential form:

$$
f_q(t) = F\cos\omega t = \frac{F}{2}e^{i\omega t} + \frac{F}{2}e^{-i\omega t} \tag{5.8}
$$

By substituting this form of harmonic excitation in Eq. 5.6, each term in the Volterra series expansion of the response is also obtained as a combination of complex exponential terms. For example, the first three terms of the series are obtained as follows:

$$
\begin{aligned}
q_1(t) &= H_1(\omega)\tfrac{F}{2}e^{i\omega t} + H_1(-\omega)\tfrac{F}{2}e^{-i\omega t} \\
q_2(t) &= H_2(\omega,\omega)\left(\tfrac{F}{2}\right)^2 e^{i2\omega t} + 2H_2(\omega,-\omega)\left(\tfrac{F}{2}\right)^2 + \\
&\quad H_2(-\omega,-\omega)\left(\tfrac{F}{2}\right)^2 e^{-i2\omega t} \\
q_3(t) &= H_3(\omega,\omega,\omega)\left(\tfrac{F}{2}\right)^3 e^{i3\omega t} + 3H_3(\omega,\omega,-\omega)\left(\tfrac{F}{2}\right)^3 e^{i\omega t} \\
&\quad +3H_3(\omega,-\omega,-\omega)\left(\tfrac{F}{2}\right)^2 e^{-i\omega t} \\
&\quad +H_3(-\omega,-\omega,-\omega)\left(\tfrac{F}{2}\right)^3 e^{-i3\omega t}
\end{aligned}
\tag{5.9}
$$

Substituting the components of the Volterra series from Eq. 5.9 in Eq. 5.6 results in the following equation which describes the response of the system to a sinusoidal excitation as a combination of sinusoidal terms at the excitation frequency and its

harmonics:

$$q(t) = \sum_{n=1}^{\infty} \sum_{m=0}^{n} \binom{n}{m} H_{n,m} \left(\frac{F}{2}\right)^n e^{i(n-2m)\omega t} \tag{5.10}$$

where $H_{n,m}$ indicates the N-th order FRF with $n-m$ arguments of (ω) and m arguments of $(-\omega)$. Equation 5.10 can be further simplified by applying the reflection property of the FRFs [107], i.e. $H_1(-\omega) = {H_1}^*(\omega)$, $H_2(-\omega,-\omega) = {H_2}^*(\omega,\omega)$, etc., where * stands for the conjugate of a complex value. After simplifications, as shown in Eq. 5.10, the response to a sinusoidal excitation can be expressed as a combination of sinusoidal motions at the excitation frequency and its harmonics. The component of the motion at the excitation frequency is obtained as

$$\begin{aligned} Q(\omega) = F H_1(\omega) + \tfrac{3}{4} F^3 H_3(\omega,\omega,-\omega) \\ + \tfrac{5}{8} F^5 H_5(\omega,\omega,\omega,-\omega,-\omega) + \cdots \end{aligned} \tag{5.11}$$

where $Q = X, Y$, or Z is the Fourier transformation of the response $q(t) = x, y$, or z. Similarly, the components of the response at the second and third harmonics of the excitation frequency are obtained as follows:

$$\begin{aligned} Q(2\omega) &= \tfrac{F^2}{2} H_2(\omega,\omega) + \tfrac{F^4}{2} H_4(\omega,\omega,\omega,-\omega) + \cdots \\ Q(3\omega) &= \tfrac{F^3}{4} H_3(\omega,\omega,\omega) + \tfrac{5}{16} F^5 H_5(\omega,\omega,\omega,-\omega,-\omega) + \cdots \end{aligned} \tag{5.12}$$

As shown in Eqs. 5.11 and 5.12, the components of the response of the nonlinear system at the excitation frequency and its harmonics are determined by the HFRF of the system and the amplitude of the excitation force.

By applying the probing method [107], approximate equations can be developed to formulate the HFRF of the SDOF system shown in Eq. 5.5 in terms of its linear and nonlinear damping and stiffness coefficients. For this purpose, Eq. 5.10 is substituted in Eq. 5.5 and the coefficients of similar terms are equated. As a result, the first order FRF is approximated in terms of the linear stiffness and damping coefficients, as follows:

$$H_1(\omega) = \frac{1}{k_1 - m\omega^2 + i\omega c_1} \tag{5.13}$$

As well, the probing method leads to the following approximation of the third-order FRF in terms of the cubic stiffness and damping parameters:

$$H_3(\omega,\omega,-\omega) = (-ic_3\omega^3 - k_3)\ H_1(\omega)^3 H_1(-\omega) \tag{5.14}$$

5.2.2 Identification of parameters

In this section, following the method presented in [108], Eqs. 5.11, 5.13, and 5.14 are used to identify the damping and stiffness parameters of the system in Eq. 5.5. Suppose the SDOF system in Eq. 5.5 is excited by a sinusoidal force at the frequency of ω and amplitude of $F_n,\ n = 1...N$. Considering the terms up to H_5 in Eq. 5.11, the response of the system at the excitation frequency for each force level (i.e. $Q_n(\omega)$, $n = 1...N$) can be expressed in terms of the HFRF and the excitation amplitudes, as follows:

$$\begin{bmatrix} Q_1(\omega) \\ Q_2(\omega) \\ \vdots \\ Q_N(\omega) \end{bmatrix} = \begin{bmatrix} F_1 & \frac{3}{4}F_1^3 & \frac{5}{8}F_1^5 \\ F_2 & \frac{3}{4}F_2^3 & \frac{5}{8}F_2^5 \\ \vdots & \vdots & \vdots \\ F_N & \frac{3}{4}F_N^3 & \frac{5}{8}F_N^5 \end{bmatrix} \begin{bmatrix} H_1(\omega) \\ H_3(\omega,\omega,-\omega) \\ H_5(\omega,\omega,\omega,-\omega,-\omega) \end{bmatrix} \tag{5.15}$$

Having obtained $Q_n(\omega)$ terms in Eq. 5.15 from the standard Fourier analysis of the measured response, one can determine the HFRF, $H_1(\omega)$, $H_3(\omega,\omega,-\omega)$ and $H_5(\omega,\omega,\omega,-\omega,-\omega)$ as the Least Squares Estimation (LSE) of the equation. Subsequently, the stiffness and damping parameters are obtained from curve-fitting the HFRF estimated at a set of frequencies, ω_1 to ω_{Nf}, in the vicinity of the resonance peak. The linear parameters are estimated by fitting Eq. 5.13 on the first order FRF as follows:

$$\begin{bmatrix} -\omega_1^2 & 1 & 0 \\ 0 & 0 & \omega_1 \\ \vdots & \vdots & \vdots \\ -\omega_{Nf}^2 & 1 & 0 \\ 0 & 0 & \omega_{Nf} \end{bmatrix} \begin{bmatrix} m \\ k_1 \\ c_1 \end{bmatrix} = \begin{bmatrix} \mathrm{Re}\left[H_1(\omega_1)^{-1}\right] \\ \mathrm{Im}\left[H_1(\omega_1)^{-1}\right] \\ \vdots \\ \mathrm{Re}\left[H_1(\omega_{Nf})^{-1}\right] \\ \mathrm{Im}\left[H_1(\omega_{Nf})^{-1}\right] \end{bmatrix} \tag{5.16}$$

and the cubic stiffness and damping parameters are obtained by fitting Eq. 5.14 on the third order FRF estimated in Eq. 5.15:

$$\begin{bmatrix} 0 & -1 \\ -{\omega_1}^3 & 0 \\ \vdots & \vdots \\ 0 & -1 \\ -\omega_{Nf}^3 & 0 \end{bmatrix} \begin{bmatrix} c_3 \\ k_3 \end{bmatrix} = \begin{bmatrix} \mathrm{Re}\left[\frac{H_3(\omega_1,\omega_1,-\omega_1)}{H_1(\omega_1)^3 H_1(-\omega_1)}\right] \\ \mathrm{Im}\left[\frac{H_3(\omega_1,\omega_1,-\omega_1)}{H_1(\omega_1)^3 H_1(-\omega_1)}\right] \\ \vdots \\ \mathrm{Re}\left[\frac{H_3(\omega_{Nf},\omega_{Nf},-\omega_{Nf})}{H_1(\omega_{Nf})^3 H_1(-\omega_{Nf})}\right] \\ \mathrm{Im}\left[\frac{H_3(\omega_{Nf},\omega_{Nf},-\omega_{Nf})}{H_1(\omega_{Nf})^3 H_1(-\omega_{Nf})}\right] \end{bmatrix} \tag{5.17}$$

Both the linear and nonlinear stiffness and damping parameters are obtained from the LSE of Eqs. 5.16 and 5.17, respectively.

5.2.3 Experimental Results

The robotic machining system shown in Fig. 4.1 was excited using step-sine forces with frequencies in the vicinity of the resonance peaks of the nominal FRFs. For example, step-sine forces were applied in Y-direction with frequencies increasing from 16.6 to 17.9 Hz to cover the mode around 17.4 Hz. The frequency increment of 0.05 Hz was used at each step and the force amplitude was kept constant. Sample excitation force and the resulting displacement response are shown in Fig. 5.3. Note that the velocity response measured using LDV was numerically integrated to obtain the displacement response. The test was repeated using force amplitudes of approximately 1.8, 5.8, 9.5, 12.6, 15.6 and 17.2 N. After each frequency increment, the TCP was excited at a constant frequency and amplitude for about 25 seconds. After a few seconds of pause to let the transient vibrations settle down, the excitation was repeated at a higher frequency. In each excitation step, the first 5 seconds of the response was considered as transient vibrations and the rest was used as steady state response for the analyses.

In Fig. 5.4(a), the power spectral density of the displacement response to the excitation force at the nominal resonance frequency ($\sim$ 17.5 Hz) is shown for the lowest and highest force amplitudes, i.e. 1.8 and 17.2 N, respectively. The response in both force levels has components at the harmonics of the excitation frequency due to the system nonlinearities. Parts (b) and (c) of Fig. 5.4 show the ratio of the response at $\omega = 17.5$ Hz to the response at $2\omega = 35$ Hz and $3\omega = 52.5$ Hz for different excitation force amplitudes. By increasing the excitation force amplitude, the ratio of the component of the response at 2ω becomes smaller after the initial increase. However, the component at the third harmonic 3ω becomes stronger as the force amplitude increases. This observation supports the assumption of cubic

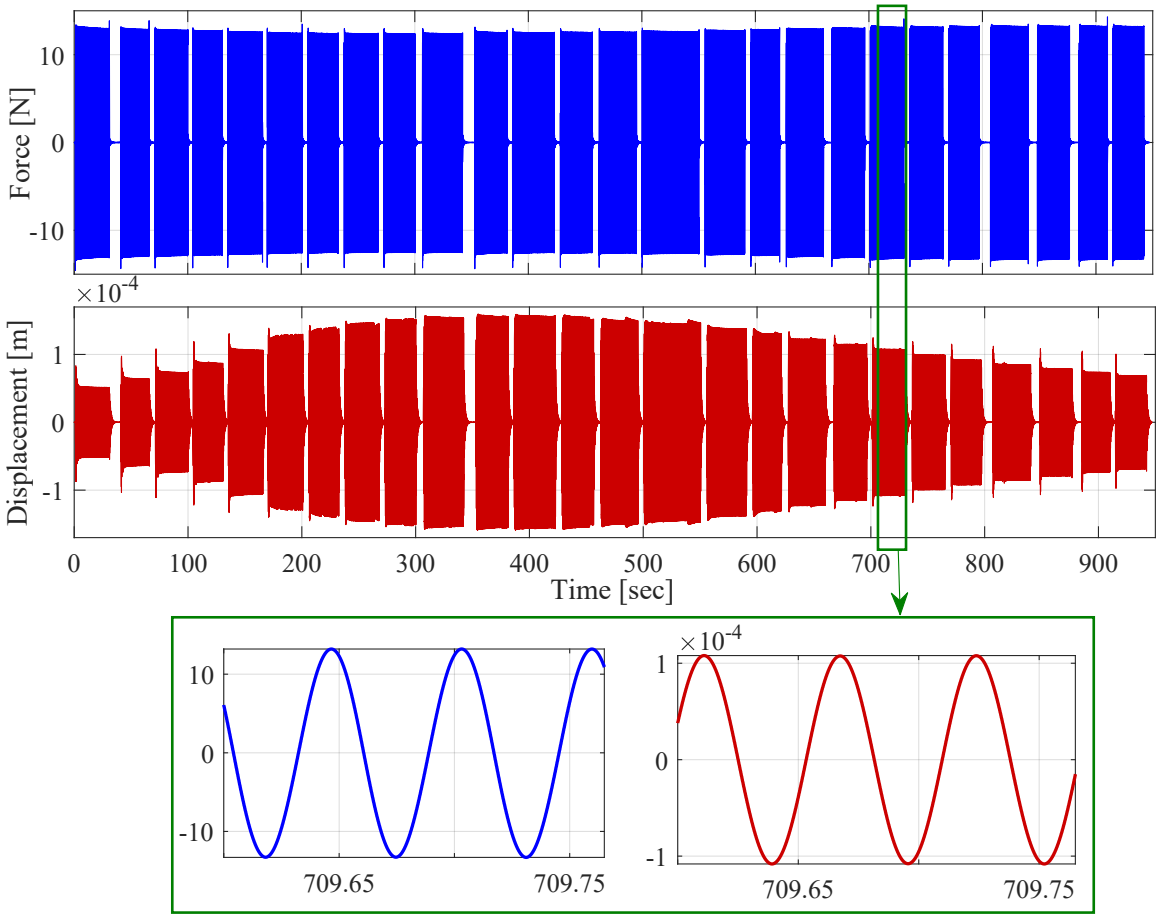

Figure 5.3: Sample excitation force and corresponding displacement signals in Y direction; Force amplitude: 12.6 N, Start frequency: 16.6 Hz, End frequency: 17.9 Hz.

nonlinearities and neglecting of quadratic terms developed earlier, because systems with significant quadratic nonlinearities display strong second-harmonic components in their harmonic response [107].

The receptance in Y-direction was calculated as the ratio of the Fourier transformation of the displacement to the Fourier transformation of the excitation force i.e. $Y(\omega)/F(\omega)$, and the resulting receptance plots are shown in Fig. 5.5. Note that the first-order FRF of the system, $H_1(\omega)$, is different than the receptance shown in Fig. 5.5. According to Eq. 5.13, the first-order FRF is unique regardless of the excitation force amplitude. The receptance, however, represents $Q(\omega)/F$ in Eq. 5.11 and depends on the excitation force amplitude and HFRF. As shown in Fig. 5.5, the resonance peak of the receptance first decreases by increasing the force amplitude up to 9.5 N, but then increase at higher force amplitudes. This change in behav-

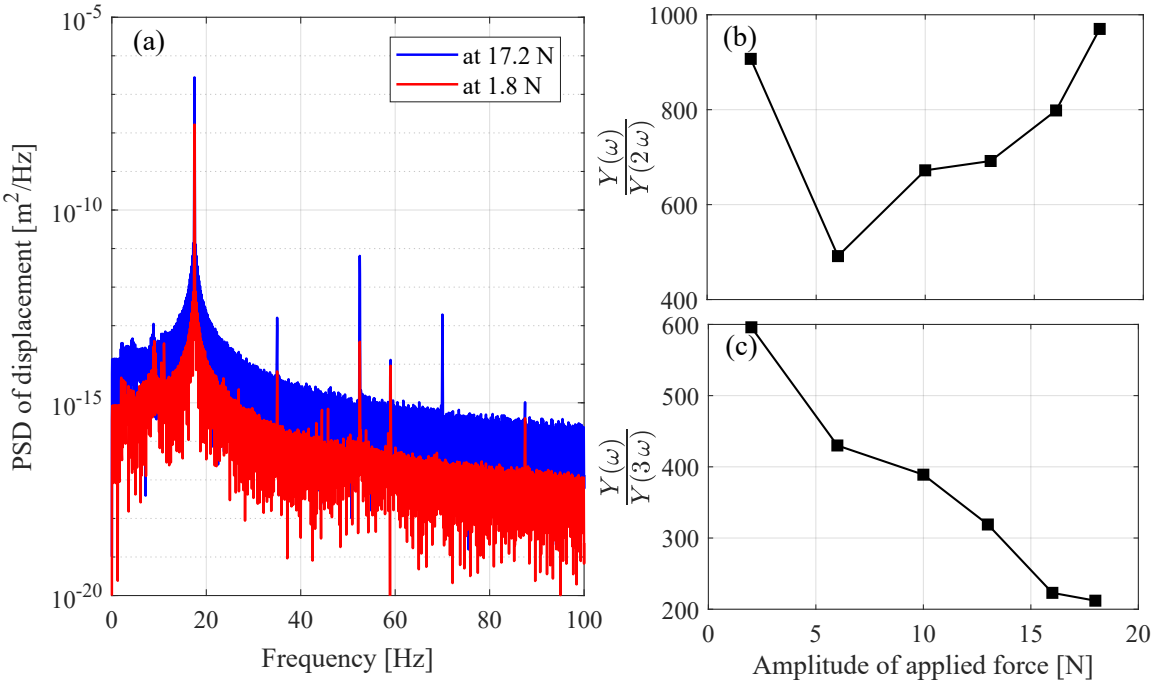

Figure 5.4: (a) Power spectral Density (PSD) of the displacement response when the system is excited at $\omega = 17.5$ Hz; Ratio of the response at ω to the response at (b) 2ω and (c) 3ω.

Table 5.1: Identified model parameters for the mode at 17.5 Hz in Y direction.

Model parameters	m (kg)	c_1 (N.sec/m)	c_3 (N.sec^3/m^3)	k_1 (N/m)	k_3 (N/m^3)
At lower force amplitudes	188	305	2.53e6	2.26e6	-5.05e12
At higher force amplitudes	196	579	5.79e5	2.31e6	7.62e11

ior is consistent with the change in restoring force discussed in the Section 5.1. To understand the reason for different dynamics at different ranges of force amplitudes, the stiffness and damping mechanisms in the robot's joints must be studied, which is beyond the scope of this paper. To ensure that the identified model is representative of the system dynamics during machining operations, in the identification process, it is important to use force amplitudes that are close to the force levels typically experienced during machining. In what follows, the method presented in Section 5.2.2 is used to identify the parameters of the SDOF system in Eq. 5.5 using the step-sine excitation results in the vicinity of the nominal mode at 17.5 Hz, in Y-direction. The model parameters are identified for two ranges of force amplitudes; first at the lower force amplitudes 1.8, 5.8 and 9.5 N, and then at the higher force amplitudes 12.6, 15.6 and 17.2 N.

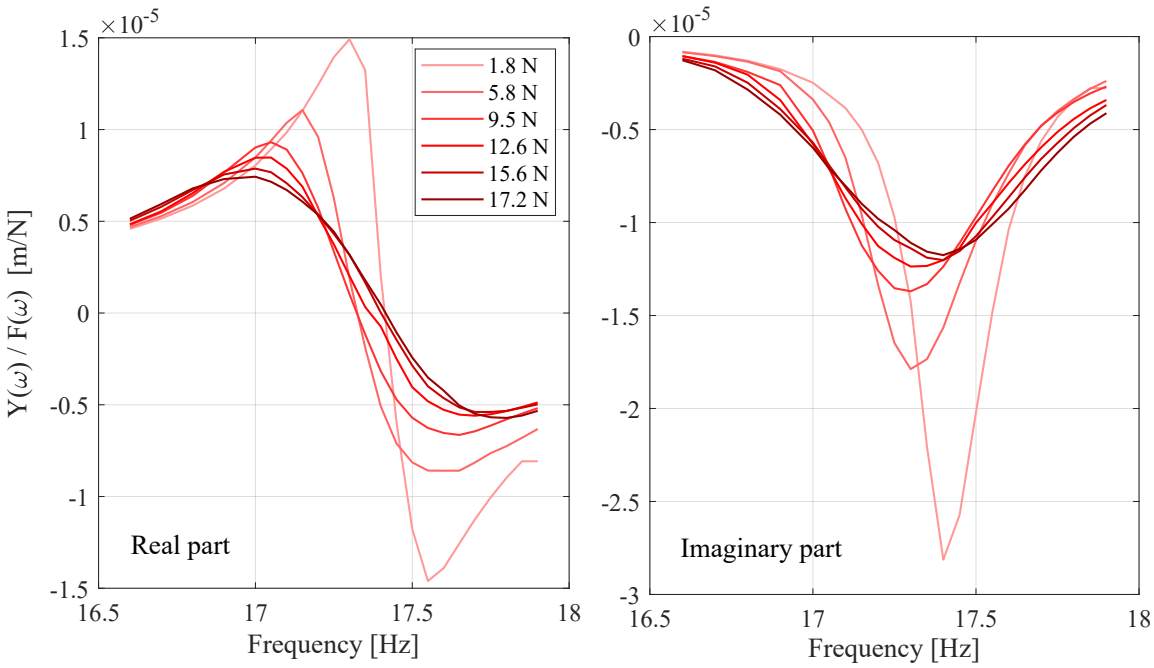

Figure 5.5: Measured receptances from step-sine tests for the mode around 17.5 Hz in Y direction.

In the first step of identification, at each frequency in the step-sine signals, the Fourier transformations of the excitation force and the resulting displacement response for all of the force amplitudes were substituted in Eq. 5.15 to estimate the corresponding first, third, and fifth order FRF. The first order FRF, $H_1(\omega)$, resulting from the identification when lower force amplitudes were used is shown with the dashed line in Fig. 5.6-c. Subsequently, the estimated first order FRF, $H_1(\omega)$ for $\omega = \omega_1 ... \omega_{Nf}$, are substituted in Eq. 5.16 and the linear parameters of the SDOF system, m, k_1, and c_1, are obtained as the LSE of the resulting equation. The identified linear parameters for both low and high force levels are shown in Table 5.1. In addition to the estimated first order FRF, Fig. 5.6-c also shows the first-order FRF that is obtained by substituting the identified parameters in Eq. 5.13. The agreement between the two FRF in this figure confirms the accuracy of the identified linear stiffness and damping parameters.

In the second step of identification, the estimated first and third order FRFs, $H_1(\omega)$ and $H_3(\omega, \omega, -\omega)$ for $\omega = \omega_1 ... \omega_{Nf}$, are substituted in Eq. 5.17 and the nonlinear parameters (k_3 and c_3) are determined as the LSE of the resulting equation. The identified parameters are shown in Table 5.1. To verify the accuracy of the identified

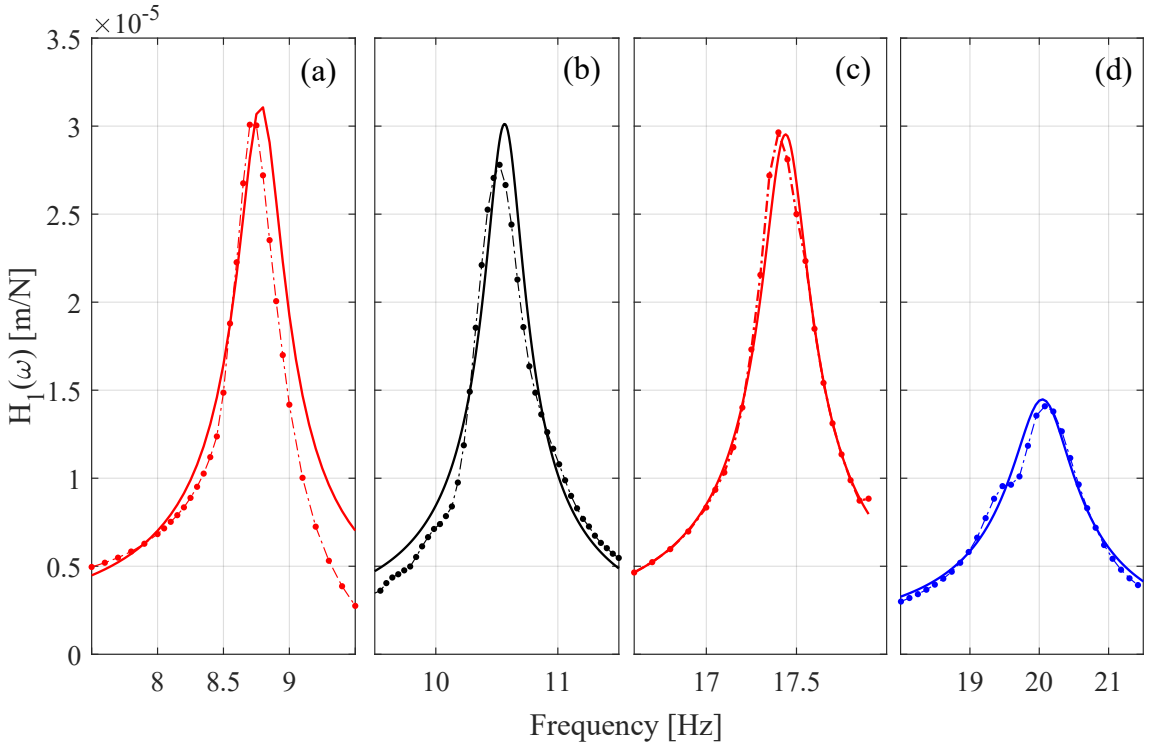

Figure 5.6: Magnitude of the identified (dashed lines) and fitted (solid lines) first-order FRFs of the mode at (a) 8.8 Hz in Y direction, (b) 10.5 Hz in Z direction, (c) 17.5 Hz in Y direction and (d) 20 Hz in X direction.

model, the response of the SDOF system to step-sine excitation, at the same force amplitudes and in the same frequency range as the experiments, was simulated in time domain using Runge-Kutta method. The receptance functions $Y(\omega)/F(\omega)$ were then calculated and compared to the ones measured in step-sine tests. The results are shown in Fig. 5.7 for both models at lower and higher force amplitudes. The natural frequency variation and amplitude reduction are captured well with the identified cubic models. The simulated results are in good agreement with the experimental results except at the force amplitude of 12.6 N where the transition from softening to hardening behaviour occurs.

Similar identification procedures were used to identify the parameters of the SDOF system (Eq. 5.5) in the vicinity of the other flexible vibration modes shown in Fig. 4.3. The identified model parameters for each mode are presented in Table 5.2. The identified and curve-fitted first-order FRF are shown in Fig. 5.6. The measured receptance functions and the ones simulated using the identified parameters are shown in Figs. 5.8, 5.9 and 5.10. Unlike the mode at 17.5 Hz in Y-direction, the softening

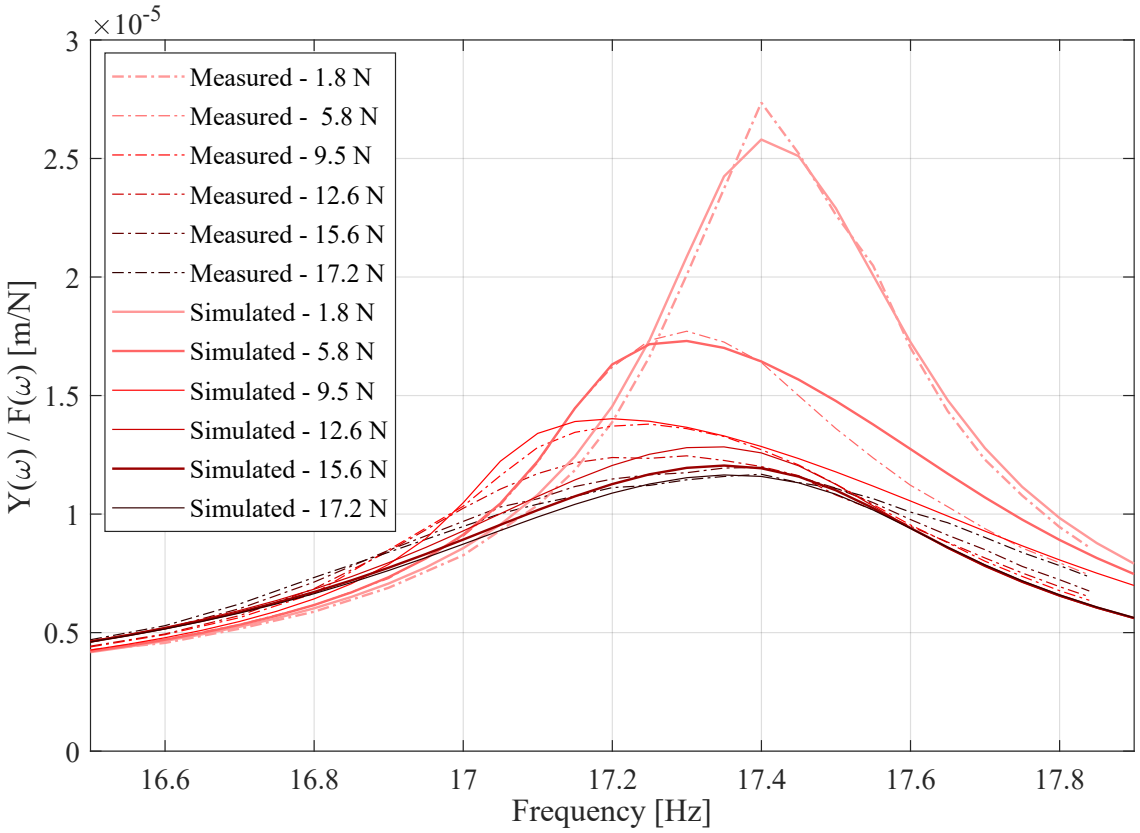

Figure 5.7: Magnitude of the receptance functions obtained experimentally and simulated using the identified model parameters in Table 5.1 for the mode at 17.5 Hz in Y direction.

behavior of the modes do not change in the entire range of the tested force levels and therefore a single set of parameters are identified for each mode. Figure 5.8 shows that the model can predict the receptance for the mode in X direction with an acceptable accuracy. However, the identified models for the modes around 9 and 10.5 Hz in Y and Z-directions, respectively, display a lower agreement with the measured results as shown in Figs. 5.9 and 5.10. The possible reason for the the lower accuracy in these modes could be the nonlinear coupling of closely-spaced modes. From Figs. 5.6(a) and (b), it can be seen that the error in predicting receptance functions originates from the identified linear parameters, as the accuracy of curve-fitting $H_1(\omega)$ for these modes are not as good as the mode at 17.5 Hz. This lower accuracy can be explained due to the existence of closely-spaced modes in the vicinity of the two modes shown Figs. 5.6(a) and (b). In the case of the mode at about 9 Hz in Fig. 5.9, although the amplitude of the receptance deviates from experimental measurements, the resonance

Table 5.2: Identified model parameters for the vibration modes around 20 Hz in X direction, 9 Hz in Y direction and 10.5 Hz in Z direction.

Model parameters	m (kg)	c_1 (N.sec/m)	c_3 (N.sec^3/m^3)	k_1 (N/m)	k_3 (N/m^3)
Mode in X direction at 20 Hz	97	548	4.65e5	1.54e6	-2.41e12
Mode in Y direction at 9 Hz	268	580	6.06e6	8.16e5	-3.23e12
Mode in Z direction at 10.5 Hz	243	420	3.33e6	1.08e6	-2.71e12

frequency variation is captured well by the model. However, in the case of the mode at 10.5 Hz in Fig. 5.10, the identified k_3 causes larger variation in the resonance frequency compared to the experimental results. Note that by increasing the force amplitude, the mode at 10.5 Hz becomes closer to its adjacent mode while the mode at 9 Hz moves away from the nearby mode (see Fig. 4.3). To address this problem, new models considering nonlinear coupling of the modes have to be developed in future studies.

5.3 Conclusions

A nonlinear Single Degree of Freedom (SDOF) model was presented to describe the vibration response at the TCP of a KUKA robotic machining system. Analysis of the experimentally determined restoring forces demonstrated that the nonlinearity of the system can be represented by cubic stiffness and damping terms. The Higher-order FRF of the nonlinear SDOF system were estimated experimentally from the step-sine excitation at the TCP, and were used to identify the linear and nonlinear parameters of the SDOF model.

The vibration response predicted by the presented SDOF model was shown to accurately capture the nonlinear behaviour of the system as observed in experimental measurements. When the presented approach is used to model nonlinearities in the vicinity of closely spaced linear modes, the modal coupling caused by the nonlinearities undermines the accuracy of the model predictions.

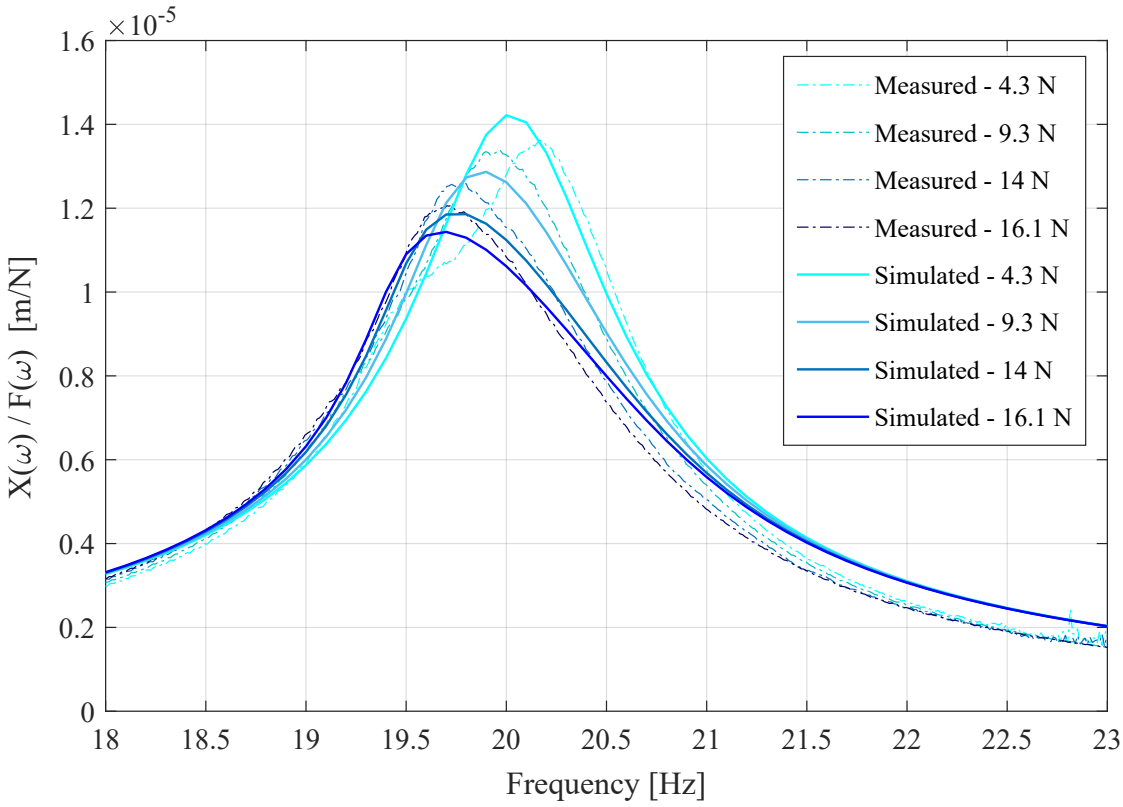

Figure 5.8: Magnitude of the receptance functions obtained experimentally and simulated using the identified model parameters for the vibration mode around 20 Hz in X direction.

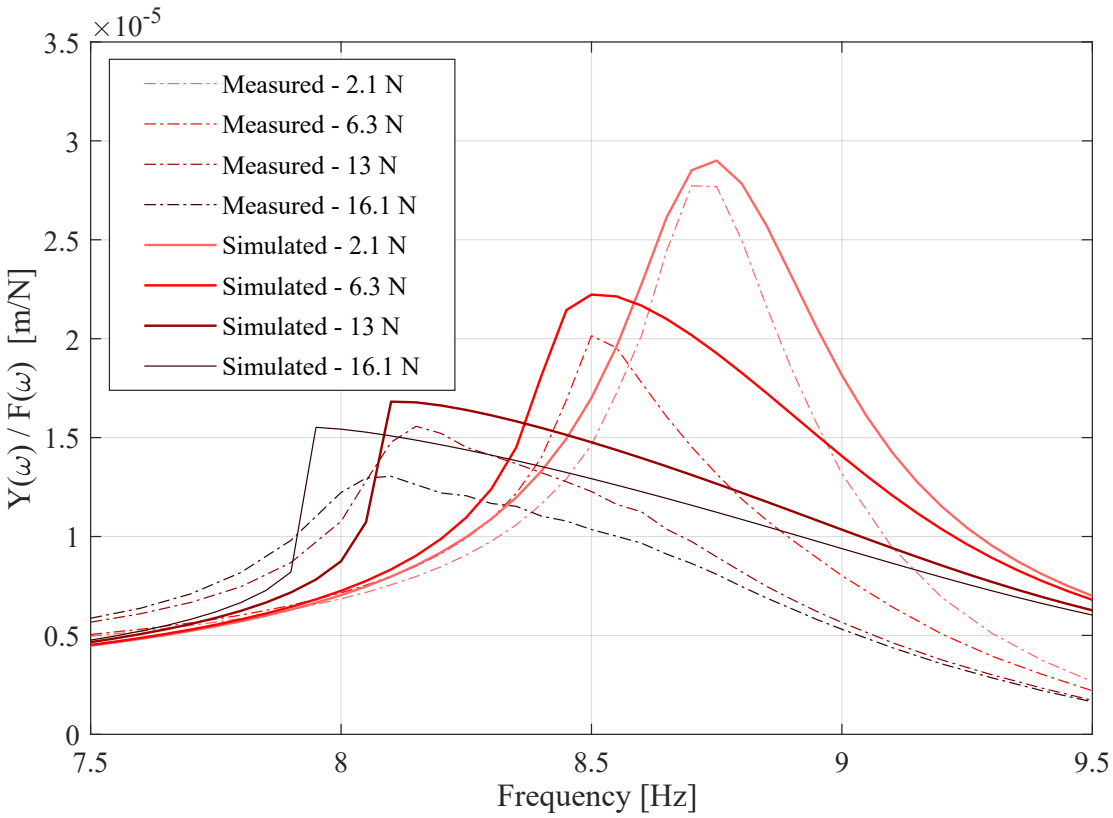

Figure 5.9: Magnitude of the receptance functions obtained experimentally and simulated using the identified model parameters for the vibration mode around 9 Hz in Y direction.

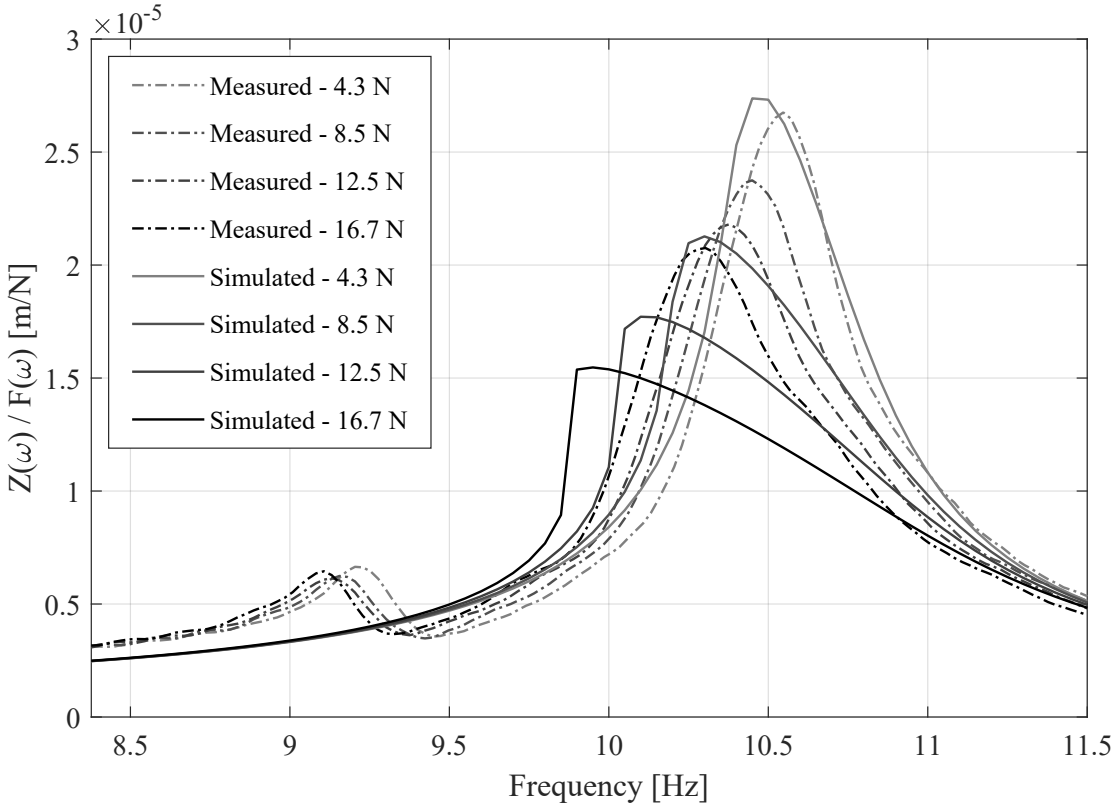

Figure 5.10: Magnitude of the receptance functions obtained experimentally and simulated using the identified model parameters for the vibration mode around 10.5 Hz in Z direction.

Chapter 6

Bifurcation analysis of vibrations in nonlinear robotic milling system

The experimental study in Chapter 4 confirmed the significance of the nonlinearity of the robot's vibration response at its TCP. Then, in Chapter 5, the nonlinearities were characterized as cubic stiffness and damping in the restoring forces and a method was presented to identify the nonlinear model parameters based on the Higher-order FRF measured at the robot's TCP. The extent to which the identified nonlinearities affect the robot's chatter in milling remained a question, which is studied in this chapter. A 2DOF nonlinear vibratory model is presented to study regenerative chatter in robotic milling. The dynamics in the presented model is described by a set of Delay Differential Equations with structural nonlinearities, periodic machining forces, and non-smoothness due to intermittent cutting (entrance and exit of the cutting edges to and from the cutting region) and loss-of-contact at high-amplitude oscillations. Numerical continuation with smoothing techniques is used to determine the combinations of spindle speed and axial depth of cut at which the forced periodic vibrations go through secondary Hopf or period doubling bifurcations.

6.1 Dynamics

The TCP dynamics of the robot under milling forces is modelled by the 2DOF system shown in Fig. 6.1. The two degrees of freedom consist of the TCP deflections in the feed ($\overline{x}$) and normal ($\overline{y}$) directions. Angular deflections are neglected to simplify the model. The deflection in the axial direction ($\overline{z}$) is also neglected, assuming a

milling tool with straight (non-helical) edges that generates negligible forces in the axial direction. The total restoring forces in each direction, $f_{r,\overline{x}}$ and $f_{r,\overline{y}}$ shown in Figs. 5.2 and 5.1, consist of linear and nonlinear stiffness and damping terms. In the following sections, firstly the general equations of motion of this 2DOF model subjected to periodic and non-smooth milling forces is presented. Then, the approach to approximating the resulting equations by a set of smooth autonomous delay differential equations, that can be used in numerical continuation for bifurcation analysis, is introduced.

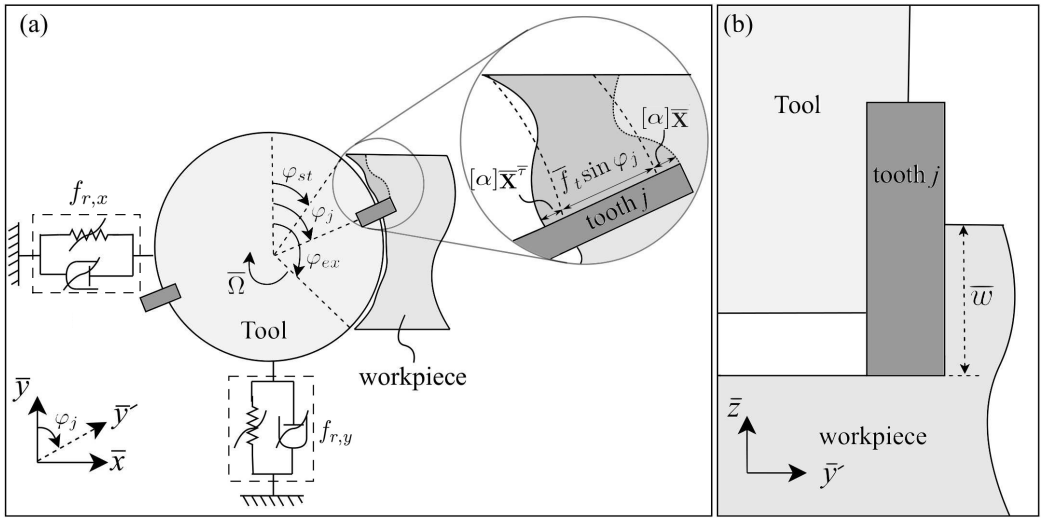

Figure 6.1: 2DOF Model of milling system with nonlinear structural dynamics.

6.1.1 Equations of motion

The equations governing the motion of the 2DOF system in Fig. 6.1 subjected to cutting forces $\overline{\mathbf{F}}_{cut}$ can be written as follows:

$$\overline{\mathbf{M}}\,\ddot{\overline{\mathbf{X}}} + \overline{\mathbf{C}}\,\dot{\overline{\mathbf{X}}} + \overline{\mathbf{K}}\,\overline{\mathbf{X}} + \overline{\mathbf{f}}_n(\dot{\overline{\mathbf{X}}}, \overline{\mathbf{X}}) = \overline{\mathbf{F}}_{cut} \tag{6.1}$$

where $\overline{\mathbf{X}} = \begin{bmatrix} \overline{x}(\bar{t}) & \overline{y}(\bar{t}) \end{bmatrix}^T$, and $\overline{x}(\bar{t})$ and $\overline{y}(\bar{t})$ are deflections in the feed and normal directions, respectively. Time is denoted by $\bar{t}$. Inertial forces and the linear components of restoring forces are modelled by a coupled 2DOF system with symmetric mass $\overline{\mathbf{M}}$, stiffness $\overline{\mathbf{K}}$, and damping $\overline{\mathbf{C}}$ matrices:

$$\overline{\mathbf{M}} = \begin{bmatrix} \overline{m}_{xx} & \overline{m}_{xy} \\ \overline{m}_{yx} & \overline{m}_{yy} \end{bmatrix}, \quad \overline{\mathbf{C}} = \begin{bmatrix} \overline{c}_{xx} & \overline{c}_{xy} \\ \overline{c}_{yx} & \overline{c}_{yy} \end{bmatrix}, \quad \overline{\mathbf{K}} = \begin{bmatrix} \overline{k}_{xx} & \overline{k}_{xy} \\ \overline{k}_{yx} & \overline{k}_{yy} \end{bmatrix} \tag{6.2}$$

The nonlinear components of restoring forces are represented by vector $\overline{\mathbf{f}}_n(\dot{\overline{\mathbf{X}}}, \overline{\mathbf{X}}) \in \mathbb{R}^2$. In light of the results presented in Chapter 5, the nonlinear restoring forces are approximated by cubical stiffness and damping terms, as follows:

$$\overline{\mathbf{f}}_n(\dot{\overline{\mathbf{X}}}, \overline{\mathbf{X}}) = \overline{\mathbf{C}}_3 \, \dot{\overline{\mathbf{X}}}^{\circ 3} + \overline{\mathbf{K}}_3 \, \overline{\mathbf{X}}^{\circ 3} \tag{6.3}$$

where

$$\overline{\mathbf{C}_3} = \begin{bmatrix} \overline{c}_{3xx} & 0 \\ 0 & \overline{c}_{3yy} \end{bmatrix}, \quad \overline{\mathbf{K}_3} = \begin{bmatrix} \overline{k}_{3xx} & 0 \\ 0 & \overline{k}_{3yy} \end{bmatrix} \tag{6.4}$$

The circle superscript designates element-wise power operator. The parameters $\overline{c}_{3qq}$ and $\overline{k}_{3qq}$ $(q = x, y)$ are the damping and stiffness constants for the nonlinear terms.

Cutting forces are functions of the thickness of the chip that is being removed. Although both linear and nonlinear functions are used to model the relationship between the chip thickness and the resulting forces, a linear model is used to focus on the nonlinearities arising from structural dynamics only. With this assumption, we are able to formulate the cutting force vector $\overline{\mathbf{F}}_{cut}$ as follows:

$$\overline{\mathbf{F}}_{cut} = \overline{w} K_{tc}[\alpha] \left\{ \overline{\mathbf{f}}_t + \overline{\mathbf{X}} - \overline{\mathbf{X}}^{\overline{\tau}} \right\} \tag{6.5}$$

where K_{tc} is a constant coefficient representing the tangential cutting force coefficient [22] and $\overline{w}$ is the axial cutting depth shown in Fig. 6.1. The total chip thickness, also depicted in Fig. 6.1, comprises the part generated by the tool's rigid motion in the feed direction (i.e. feed motion), its elastic vibrations in the feed and normal directions, and the undulations left on the machined surface due to the vibrations of the preceding tooth. In Eq. 6.5, the contribution of the tool's feed motion is represented by the vector $\overline{\mathbf{f}}_t = \begin{bmatrix} \overline{f}_t & 0 \end{bmatrix}^T$, where $\overline{f}_t$ is the linear motion of the tool in feed direction per revolution per tooth, also known as feedrate. The effect of runout due to radial and angular eccentricity of the tool is neglected in this force model. Runout periodically changes the chip thickness generated by successive cutting teeth, adding additional content at the harmonics of spindle rotation frequency to the cutting force spectrum. These additional frequencies may alter the stability of vibrations, particularly when the harmonics are close to the natural frequencies of the system [109]. Runout is neglected in this work to focus on the effect of structural nonlinearities on chatter. In order to extend the presented model to consider runout, the feedrate $\overline{f}_t$ can be

replaced by the effective feedrate $\overline{f}_{t,e}(\varphi_j) = q_1 + q_2\cos\varphi_j + q_3\cos\varphi_j\cot\varphi_j + q_4\csc\varphi_j$, where $q_i, i = 1..4$ are constant functions of feedrate, $\overline{f}_t$, and radial and angular eccentricity of the tool's rotation centre [110]. The contribution of the tool's elastic deflections (vibrations) to the total chip thickness is represented by the vector $\overline{\mathbf{X}}$, and the effect of surface undulations is represented by the vector of delayed vibrations $\overline{\mathbf{X}}^{\overline{\tau}} = \left[\overline{x}(\overline{t}-\overline{\tau})\ \ \overline{y}(\overline{t}-\overline{\tau})\right]^T$ with $\overline{\tau}$ being the time delay. The time delay is usually assumed constant and equal to tooth passing frequency, i.e. $\overline{\tau} = \frac{2\pi}{\overline{\Omega}N}$, where $\overline{\Omega}$ is the spindle rotational speed and N is the number of cutting teeth. Under some conditions, for example when the torsional deflections are considerable, delay may be time- or state-dependent, which is not considered in this work. The matrix $[\alpha]$ consists of the directional coefficients and has the following composition:

$$[\alpha] = \sum_{j=1}^{N} g_j[\alpha_j] \tag{6.6}$$

where

$$[\alpha_j] = \begin{bmatrix} -\sin\varphi_j\,(\cos\varphi_j + k_r\sin\varphi_j) & -\cos\varphi_j\,(\cos\varphi_j + k_r\sin\varphi_j) \\ \sin\varphi_j\,(\sin\varphi_j - k_r\cos\varphi_j) & \cos\varphi_j\,(\sin\varphi_j - k_r\cos\varphi_j) \end{bmatrix} \tag{6.7}$$

$$\varphi_j = \varphi + (j-1)\frac{2\pi}{N}; \quad \varphi = \overline{\Omega}\,\overline{t} \tag{6.8}$$

The constant k_r is known as the radial cutting force coefficient. Angle φ_j, measured clockwise from $\overline{y}-$direction, is the angular immersion of tooth $j = 1..N$, and the Heaviside function g_j determines whether this angle is within the cutting immersion angle range $[\varphi_{st}\ \ \varphi_{ex}]$, shown in Fig. 6.1:

$$g_j(\varphi_j) = u(\varphi_j - \varphi_{st}) - u(\varphi_j - \varphi_{ex}) \tag{6.9}$$

with $u(\cdot)$ being unit step function. To simplify the equations in this work, we consider a tool with two teeth ($N = 2$) and either full-immersion ($\varphi_{st} = 0$ and $\varphi_{ex} = \pi$) or half-immersion down milling ($\varphi_{st} = \pi/2$ and $\varphi_{ex} = \pi$) cases. One of the two cutting teeth is in the cutting zone at any given time in the full-immersion case, resulting in a continuous cut; none of the teeth are engaged with the workpiece during half of the tool rotation cycle in half-immersion cases, resulting in an intermittent cut.

In order to non-dimensionalize the equations of motion in Eq. 6.1, we normalize

the vibration and feedrate vectors by a reference feedrate value, $\mathbf{X} = \frac{\overline{\mathbf{X}}}{\bar{f}_{to}}$, $\mathbf{f}_t = \frac{\bar{\mathbf{f}}_t}{\bar{f}_{to}}$, and time and spindle angular velocity by the natural frequency, ω_n: $t = \bar{t}\,\omega_n$, $\tau = \overline{\tau}\,\omega_n$, $\Omega = \frac{\overline{\Omega}}{\omega_n}$. The frequency ω_n is defined as $\omega_n^2 = \frac{\bar{k}_{yy}}{\overline{m}_{yy}}$. After substituting these parameters in Eq. 6.1, the non-dimensionalized form of equations of motion can be written in the following first-order form:

$$\left\{ \begin{array}{c} \dot{\mathbf{X}} \\ \ddot{\mathbf{X}} \end{array} \right\} = \left\{ \begin{array}{c} \dot{\mathbf{X}} \\ -\mathbf{C}\dot{\mathbf{X}} - \mathbf{K}\mathbf{X} - \mathbf{C}_3\dot{\mathbf{X}}^{\circ 3} - \mathbf{K}_3\mathbf{X}^{\circ 3} + \mathbf{F}_{cut} \end{array} \right\} \tag{6.10}$$

where

$$\mathbf{F}_{cut} = w\boldsymbol{\beta}[\alpha]\left\{\mathbf{f}_t + \mathbf{X} - \mathbf{X}^{\tau}\right\} \tag{6.11}$$

and

$$\begin{aligned} & w = \frac{\overline{w}K_{tc}}{\bar{k}_{yy}},\ \boldsymbol{\beta} = \overline{\mathbf{M}}^{-1}\overline{m}_{yy}\ ,\quad \mathbf{f}_t = [h_0, 0]^T,\quad h_0 = \frac{\bar{f}_t}{\bar{f}_{to}}\ , \\ & \mathbf{C} = \overline{\mathbf{M}}^{-1}\overline{\mathbf{C}}\,\omega_n^{-1}, \qquad \mathbf{K} = \overline{\mathbf{M}}^{-1}\overline{\mathbf{K}}\,\omega_n^{-2}, \\ & \mathbf{C}_3 = \overline{\mathbf{M}}^{-1}\overline{\mathbf{C}}_3\,\omega_n\,\bar{f}_{to}^{\,2},\quad \mathbf{K}_3 = \overline{\mathbf{M}}^{-1}\overline{\mathbf{K}}_3\,\omega_n^{-2}\,\bar{f}_{to}^{\,2}. \end{aligned} \tag{6.12}$$

The resulting equations of motion are nonautonomous delay differential equations due to the presence of the non-dimensional matrix of periodic coefficients, $[\alpha]$, and the delayed vibrations, $\mathbf{X}^{\tau}$, in the cutting force equation. Additionally, they are non-smooth because of the Heaviside function, g_j, that implicitly exists in the composition of $[\alpha]$, as shown in Eqs. 6.6 to 7.3. In the next sections, Eq. 6.10 is expanded to an autonomous form and smoothend to be applicable in numerical continuation method.

6.1.2 Autonomous smooth system

The nonautonomous equations of motion in Eq. 6.10 can be rewritten in an autonomous form by appending Hopf bifurcation normal form equations to it and consequently extending its dimension. Let $\mathbf{Y} = [y_1(t) \quad y_2(t)]^T$ be the solution of Hopf bifurcation normal form:

$$\dot{\mathbf{Y}} = \mathbf{T}(\mathbf{Y}) = \left\{ \begin{array}{c} \varepsilon y_1 - \omega y_2 - y_1({y_1}^2 + {y_2}^2) \\ \omega y_1 + \varepsilon y_2 - y_2({y_1}^2 + {y_2}^2) \end{array} \right\} \tag{6.13}$$

For $\varepsilon > 0$, Eq. 6.13 describes an oscillator in an autonomous differential form with trigonometric functions $y_1(t) = \varepsilon cos(\omega t)$ and $y_2(t) = \varepsilon sin(\omega t)$ as its solutions. By

appending this oscillator to Eq. 6.10 and setting $\omega = \Omega$ and $\varepsilon = 1$, the extended governing differential equations are obtained as follows:

$$\dot{\mathbf{Q}} = \mathbf{H}_c(\mathbf{Q}) \tag{6.14}$$

where $\mathbf{Q}$ is the vector of extended states

$$\mathbf{Q} = \left[\begin{array}{ccc} \mathbf{X} & \dot{\mathbf{X}} & \mathbf{Y} \end{array} \right]^T \tag{6.15}$$

and $\mathbf{H}_c$ is the right hand side of the differential equation:

$$\mathbf{H}_c = \left\{ \begin{array}{c} \dot{\mathbf{X}} \\ -\mathbf{C}\dot{\mathbf{X}} - \mathbf{K}\mathbf{X} - \mathbf{C}_3\dot{\mathbf{X}}^{\circ 3} - \mathbf{K}_3\mathbf{X}^{\circ 3} + \mathbf{F}_{cut} \\ \mathbf{T}(\mathbf{Y}) \end{array} \right\} \tag{6.16}$$

The matrix of directional coefficients for tooth j, $[\alpha_j]$ in the cutting forces $\mathbf{F}_{cut}$, can be presented using the solution of the appended oscillator, $\mathbf{Y}$. For a tool with two cutting teeth, $N = 2$, it can be shown that $[\alpha_2] = [\alpha_1]$ where

$$[\alpha_1] = \left[\begin{array}{cc} -y_2(y_1 + k_r y_2) & -y_1(y_1 + k_r y_2) \\ y_2(y_2 - k_r y_1) & y_1(y_2 - k_r y_1) \end{array} \right] \tag{6.17}$$

Therefore,

$$[\alpha] = \sum_{j=1}^{N} g_j \, [\alpha_j] = g \, [\alpha_1] \quad \text{where} \quad g = \sum_{j=1}^{N} g_j \tag{6.18}$$

For full immersion case ($\varphi_{st} = 0$ and $\varphi_{ex} = \pi$) with two teeth, one tooth is within the range at each instant and therefore $g = 1$. However, for half immersion down milling case ($\varphi_{st} = \pi/2$ and $\varphi_{ex} = \pi$) with two teeth, one tooth is within the range when $sin(\varphi)cos(\varphi) < 0$, where $\varphi = \Omega t$ is the immersion angle of the reference tooth ($j = 1$). To enable the numerical continuation of the DDE, this criteria is approximated by the following smooth function:

$$g = \frac{1}{2} \left\{ 1 + \tanh \left(\frac{-y_1 y_2}{\varepsilon_1} \right) \right\} \tag{6.19}$$

where ε_1 is a positive small number functioning as smoothing parameter. The above equations are valid for full and half immersion cases. In general, defining the suitable smoothing function may require more parameters. For a general case of

milling with two cutting teeth and arbitrary entering and exiting angles, φ_{st} and φ_{ex}, the smooth functions approximating g_j are presented in Appendix A.

6.1.3 Loss of contact at large oscillations

At high-amplitude vibrations the tool starts losing contact with the workpiece. In such cases, the cutting tooth may cut the workpiece surface generated at more than one tooth-passing period prior. To consider potential disengagement of the tool from workpiece at large oscillations, we introduce a new variable $\mathbf{Z}$ that tracks the height of the surface undulations at each moment. When the tool is actively engaged with the workpiece, undulation is formed by the TCP location, i.e. $\mathbf{Z} = \mathbf{X}$ and the cutting forces is equal to $\mathbf{F}_{cut}$, where

$$\mathbf{F}_{cut} = w\boldsymbol{\beta}[\alpha]\left\{\mathbf{f}_t + \mathbf{X} - \mathbf{Z}^{\tau}\right\} \tag{6.20}$$

When the contact is lost due to large oscillations, the cutting forces vanish and the surface variable $\mathbf{Z}$ remains at its value when the previous tooth was passing the same location, corrected by the feedrate, i.e. $\mathbf{Z} = \mathbf{Z}^{\tau} + \mathbf{f}_t$. Considering this dynamics, another equation is added to the equations of motion to account for the variation of $\mathbf{Z}$ and its effect on the cutting force, resulting in the following set of DDE:

$$\dot{\mathbf{Q}} = g_c\mathbf{H}_c + (1 - g_c)\,\mathbf{H}_f \tag{6.21}$$

where

$$\mathbf{Q} = \begin{bmatrix} \mathbf{X} & \dot{\mathbf{X}} & \mathbf{Y} & \varepsilon_2\mathbf{Z} \end{bmatrix}^T \tag{6.22}$$

$$\mathbf{H}_c = \begin{Bmatrix} \dot{\mathbf{X}} \\ -\mathbf{C}\dot{\mathbf{X}} - \mathbf{K}\mathbf{X} - \mathbf{C}_3\dot{\mathbf{X}}^{\circ 3} - \mathbf{K}_3\mathbf{X}^{\circ 3} + \mathbf{F}_{cut} \\ \mathbf{T}(\mathbf{Y}) \\ \mathbf{X} - \mathbf{Z} \end{Bmatrix} \tag{6.23}$$

$$\mathbf{H}_f = \begin{Bmatrix} \dot{\mathbf{X}} \\ -\mathbf{C}\dot{\mathbf{X}} - \mathbf{K}\mathbf{X} - \mathbf{C}_3\dot{\mathbf{X}}^{\circ 3} - \mathbf{K}_3\mathbf{X}^{\circ 3} \\ \mathbf{T}(\mathbf{Y}) \\ \mathbf{Z}^{\tau} - \mathbf{f}_t - \mathbf{Z} \end{Bmatrix} \tag{6.24}$$

Vectors $\mathbf{H}_c$ and $\mathbf{H}_f$ are the right hand side of the differential equations when the tool is in contact with the workpiece and loses contact with the workpiece, respectively. The Heaviside function g_c determines if the tool is in contact with the workpiece based on the value of the instantaneous chip thickness h and is formulated as follows:

$$g_c = \frac{1}{2}\left\{1 + \tanh\left(\frac{h_1 \tanh\left(y_2/\varepsilon_3\right)}{\varepsilon_4}\right)\right\} \tag{6.25}$$

where h_1 is the total chip thickness of the reference tooth ($j = 1$):

$$h_1 = \mathbf{Y}_f^T \left\{\mathbf{f}_t + \mathbf{X} - \mathbf{Z}^\tau\right\} \tag{6.26}$$

$\mathbf{Y}_f$ is the flipped form of vector $\mathbf{Y}$. For the case of two cutting teeth, $N = 2$, it can be shown that $h_2 = -h_1$. Moreover, the first tooth is within the cutting range of immersion angle when $sin(\varphi) > 0$. However, the second tooth is within the range when $sin(\varphi) < 0$. This is considered in Eq. 6.25 by multiplying h_1 by the $\tanh(y_2/\varepsilon_3)$ term, which smoothly approximates the sign of $y_2 = sin(\varphi)$. The smoothing parameters ε_2, ε_3 and ε_4 are small positive values.

6.2 Results and discussions

In this section, numerical continuation is used to determine the vibration stability of the 2DOF milling model developed in the previous section. As a case-study, the KUKA KR90 robotic arm with the same posture shown in Fig. 4.1 is used. The parameters of the linear mass, stiffness, and damping matrices were identified by the experimental modal analysis of the two resonance peaks at around 17 Hz and 20 Hz shown in Fig. 4.3. To ensure the negligible effect of the structure's nonlinearities on the identified parameters, direct and cross FRF between X and Y directions were measured by applying small-amplitude shaker forces in each direction. As shown in the FRF in Fig. 4.3, the modes at around 9 Hz and 11 Hz are also equally flexible at the TCP, but the robot's vibrations are mainly dominated by the modes at 17 Hz and 20 Hz when it is operated at practical milling spindle speeds. The entries of the identified linear mass, stiffness, and damping matrices are presented in Table 6.1. The parameters of the cubic stiffness and damping terms in the equations of motion (Eq. 6.1) are identified by curve-fitting the measured higher order FRF at

the TCP. The identified parameters were presented previous chapter. The entries of the nondimensional system matrices are presented in Table 6.2.

Table 6.1: Entries of linear system matrices for the KUKA KR90 R3100 robotic milling system.

(p,q)	$\overline{m}_{pq}$ (kg)	$\overline{c}_{pq}$ ($\frac{\text{N.sec}}{\text{m}}$)	$\overline{k}_{pq}$ ($\frac{\text{N}}{\text{m}}$)
(x,x)	97	548	1.54e6
(y,y)	188	305	2.26e6
$(x,y)(y,x)$	5.94	23.85	0.17e5

The workpiece material is assumed to be high density poly ethylene with experimentally determined tangential and radial cutting force coefficients of $K_{tc} = 76$ MPa and $k_r = 0.1579$. Unless otherwise stated, nondimensional feedrate of $h_0 = 1$ and smoothing parameters of 10^{-6} are used in all of the presented results.

Both full and half-immersion cases with two cutting teeth are considered in the presented analysis. Numerical continuation of the periodic solution of equations of motion developed in section 6.1 is conducted in DDE-BIFTOOL to determine the combinations of the non-dimensional depth of cut w and the rotational speed $\frac{1}{\tau}$ at which bifurcation of forced vibrations occurs, indicating chatter. First, in section 6.2.1, the continuation results are compared with the linear stability diagrams obtained by Semi Discretization Method. Then, the effect of smoothening on the dynamics of the original nonsmooth system is investigated in section 6.2.2. In section 6.2.3, it is shown that including the feedrate term in the cutting force model is essential for the bifurcation analysis of the system with structural nonlinearity. The extent of structural nonlinearity that would cause a considerable change in the stability of the underlying linear system is studied in section 6.2.4. At the end, the new mode-locked solutions that emerge from the bifurcations of forced periodic vibrations are briefly discussed.

6.2.1 Bifurcation of forced oscillations

Numerical continuation is used in this section to study the bifurcation of the forced periodic solution of Eq. 6.21. For $\varepsilon < 0$, the oscillator in Eq. 6.13 and thus Eq. 6.21 has the trivial equilibrium point of $\mathbf{Q} = \mathbf{0}$. For a constant τ and w, this trivial solution is continued in one-dimensional ε space until it goes through a Hopf Bifurcation at $\varepsilon = 0$, generating a periodic solution at the spindle frequency, Ω. At $\varepsilon = 1$, this

Table 6.2: Entries of nondimensional system matrices for the KUKA KR90 R3100 robotic milling system.

(p,q)	c_{pq}	k_{pq}	c_{3pq}	k_{3pq}	β_{pq}
(x,x)	0.0516	1.3232	0.0118	-0.0466	1.9419
(x,y)	0.0013	-0.0614	-0.002	0.0031	-0.0614
(y,x)	-0.0005	-0.0419	-0.0004	0.0015	-0.0614
(y,y)	0.0148	1.0019	0.0333	-0.0504	1.0019

parameter is kept constant and the bifurcation of the corresponding periodic solution is studied by continuing w until the periodic solution goes through a secondary Hopf (Torus) bifurcation, saddle-node bifurcation or period doubling bifurcation. The type of bifurcation is determined by checking the eigenvalues of the monodromy operator which is obtained by integrating the variational equation over one oscillation period, T. The variational equation itself is the linearized equation of the delay differential equation around the steady state periodic solution $\mathbf{Q}^*$ [111]. Once one of these bifurcations is identified, a branch of bifurcations can be continued in the 2-dimensional space of w and τ to determine the so-called chatter stability borders.

Figure 6.2 shows the borders of Torus and period doubling bifurcations resulting from the continuation of the periodic solution. The cutting forces in Eq. 6.20 comprises two parts: The part generated by the feed motion at the feedrate $\mathbf{f}_t$, and the regenerative milling forces due to current and delayed vibrations. To enable a comparison with the stability diagrams obtained by existing methods, which neglect the effect of the forces generated by the feed motion, $h_0 = 0$ was used in the cutting forces in Eq. 6.20. Nonetheless, $h_0 = 1$ is considered in the equation of undulation height, i.e. Eq. 6.24, to account for disengagement at negative chip thickness. Note that without the feed-generated forces, the periodic vibration $\mathbf{X}$ has zero amplitude with period T (i.e. equilibrium at zero). Only the first two lobes of the diagram are computed, because the system dynamics at large τ values is affected by process damping which has been neglected here [112]. Besides, the first two lobes of the diagram cover the spindle speed range that is usually used in robotic machining. Boundaries of Torus and period doubling bifurcations are shown in Fig. 6.2 and no saddle-node bifurcation was identified. Codimension-two secondary Hopf-Hopf bifurcation occurs at the intersection of the two lobes shown in Fig. 6.2. Semi-Discretization Method (SDM) was also used to determine the stability of periodic solutions when the nonlinear terms in the equations of motion are neglected. The resulting stability diagrams

are shown in Fig.6.2, which agree with the bifurcation diagram obtained by numerical continuation. Since structural nonlinearities and disengagement at negative chip thickness are neglected in the SDM results but considered in numerical continuation, the agreement of the two diagrams shows that those factors do not influence the bifurcations of the system significantly. Nonetheless, in the next sections, it is shown that the effect of nonlinearities are negligible only when the feed-generated forces are neglected; when they are added back to the model, structural nonlinearities significantly influence chatter stability.

Figure 6.2 also shows the diagram of bifurcations when the time-periodic matrix of directional coefficients $[\alpha]$ is replaced by the first term in its Fourier expansion (i.e. its average over one principal period). This approximation, which is used in the existing methods such as Multiple Scales [97], removes the time-periodic dynamics of the system before its bifurcation and thus the possibility of period doubling bifurcation, as shown in Fig. 6.2. The bifurcations of the system with periodic coefficients match the results of SDM. However, using the average coefficients, forced solutions goes through only Torus bifurcations and the period doubling branch is missing.

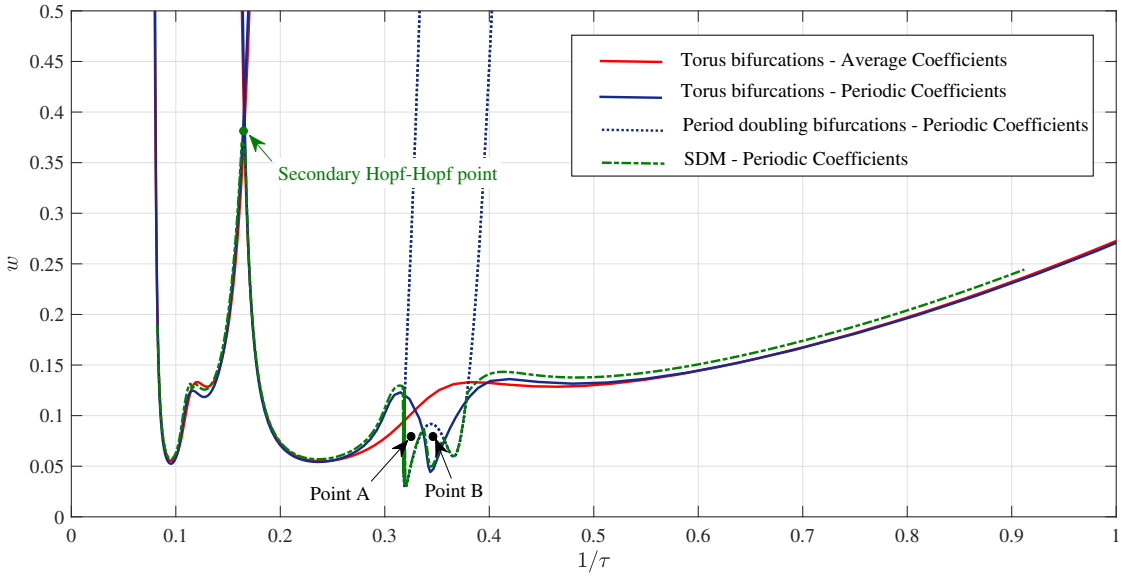

Figure 6.2: Bifurcations of solutions in parameters plane $(1/\tau, w)$ for the case of full immersion milling ($h_0 = 0$).

Numerical integration of the exact model, i.e. the model with no smoothing applied, are performed for points A and B shown in Fig. 6.2. Runge-Kutta algorithm

(ode45) is used for integration and the initial conditions $\mathbf{X} = [10^{-5}\ 0]^T$, $\mathbf{Z} = \mathbf{0}$, $y_1 = 1$ and $y_2 = 0$ are considered. Figure 6.3 shows the steady state time history and phase portrait of vibrations for these two points. The red points are sampled data at the tooth passing period, which is also equal to the system's time delay τ. At point A, where $\tau = 2.7$, the sampled points coincide two singular points on the phase portrait, indicating period doubling bifurcations. At point B, the sampled points form a closed trajectory confirming that forced vibrations have gone through Torus bifurcation at $\tau = 2.9$.

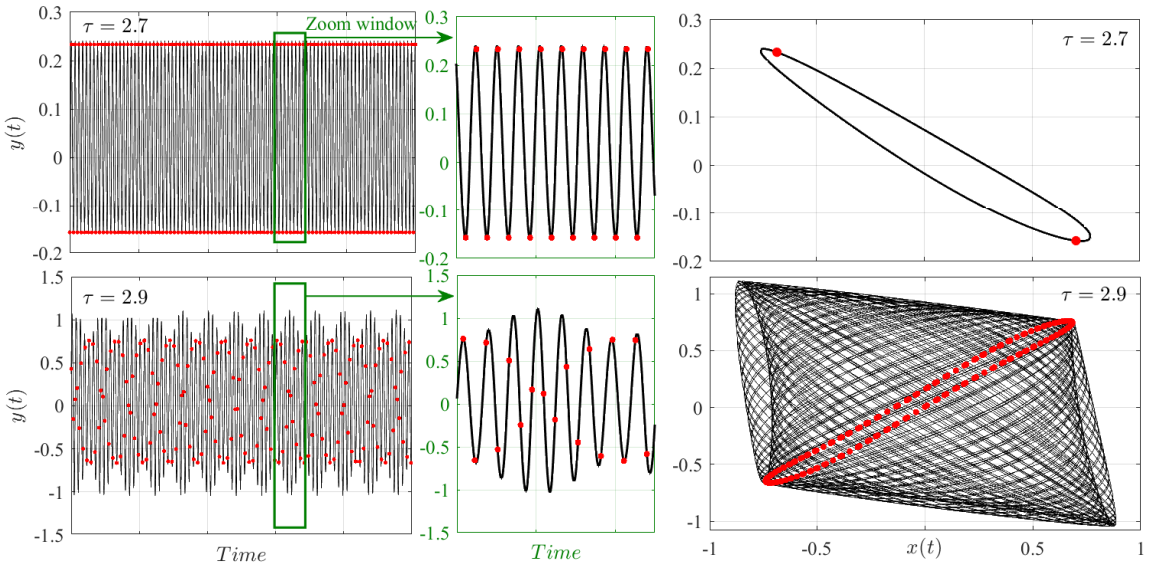

Figure 6.3: Results of numerical integration of the exact model. Time history and phase portrait of vibrations at points A and B shown in Fig. 6.2. First row: point B at $(\tau, w) = (2.7, 0.08)$; Second row: point A at $(\tau, w) = (2.9, 0.08)$. Red points show sampled data at tooth passing period.

Similarly, bifurcations of the forced periodic vibrations in the half immersion case are also studied. Figure 6.4 shows the branches of Torus and period doubling bifurcations obtained by numerical continuation for the system with periodic coefficients, as well as the stability diagram obtained from SDM. The comparison validates the bifurcation diagrams obtained from continuation method. It is notable that by reducing the radial immersion angle from full to half immersion, an island of period doubling bifurcations emerges and expands at around $1/\tau = 0.11$. For a point with coordinates $(\tau, w) = (8.7, 0.16)$, which is located inside the island of period doubling bifurcations, time history and phase portrait obtained from numerical integration of the exact model are also presented. Sampled points of the steady state solution

confirm the period doubling bifurcation inside this island.

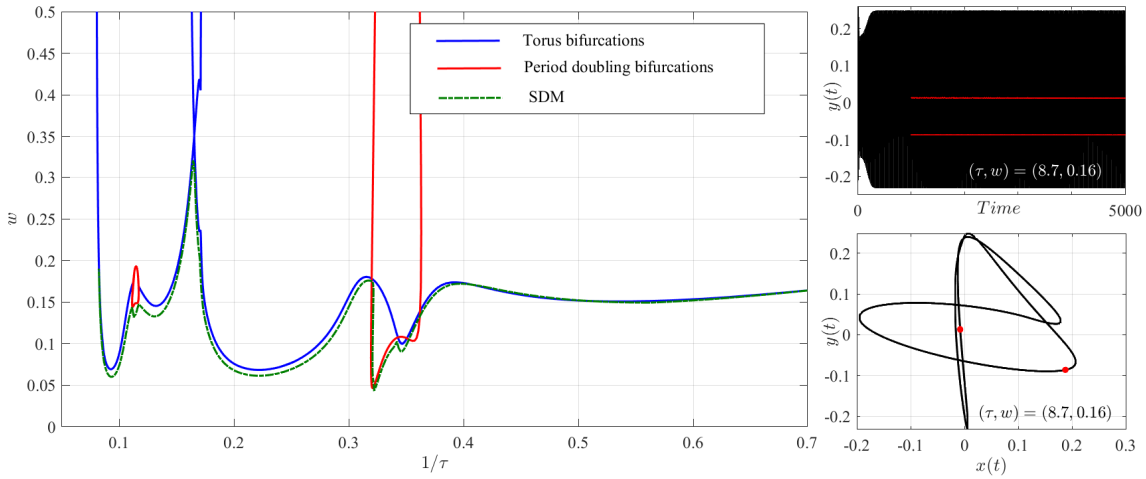

Figure 6.4: Bifurcations of forced solutions in parameters plane $(1/\tau, w)$ for the case of half immersion milling ($h_0 = 0$), and numerical integration results for the point $(\tau, w) = (8.7, 0.16)$.

Because the feedrate term is omitted from the force model in this section (to enable the comparison with SDM), numerical continuation of the nonlinear system and the SDM of the underlying linear system lead to similar results, as shown in Figs. 6.2 and 6.4. Before studying the effect of nonlinearities when the feedrate term is added back to the equations, in the next section, the effect of smoothing parameters on the resulting bifurcation diagrams is discussed.

6.2.2 Effect of smoothing parameters

In numerical continuation, a smoothed approximation of the exact non-smooth model of the milling process is used. However, this approximation can create artificial solutions or eliminate the bifurcations that are specific to non-smooth systems [113]. In this section, it is confirmed that the system dynamics in the vicinity of the bifurcation of forced solutions is not affected by the applied smoothening technique.

As discussed in section 6.1, non-smoothness in milling dynamics originates from two sources: intermittent exiting and entering of the cutting teeth into the workpiece due to rotation of the tool, and loss of contact due to large oscillations. The tool's intermittent entrance and exit from the cut does not cause non-smoothness in the full immersion case, and in the half immersion case this effect was smoothened by

introducing the smoothing parameter ε_1 in Eq. 6.19. Figure 6.5 shows the bifurcations diagram generated by using different values of ε_1 in the case of half immersion milling operation. In this figure, disengagement at negative chip thickness is neglected and therefore ε_1 is the only smoothing parameter.

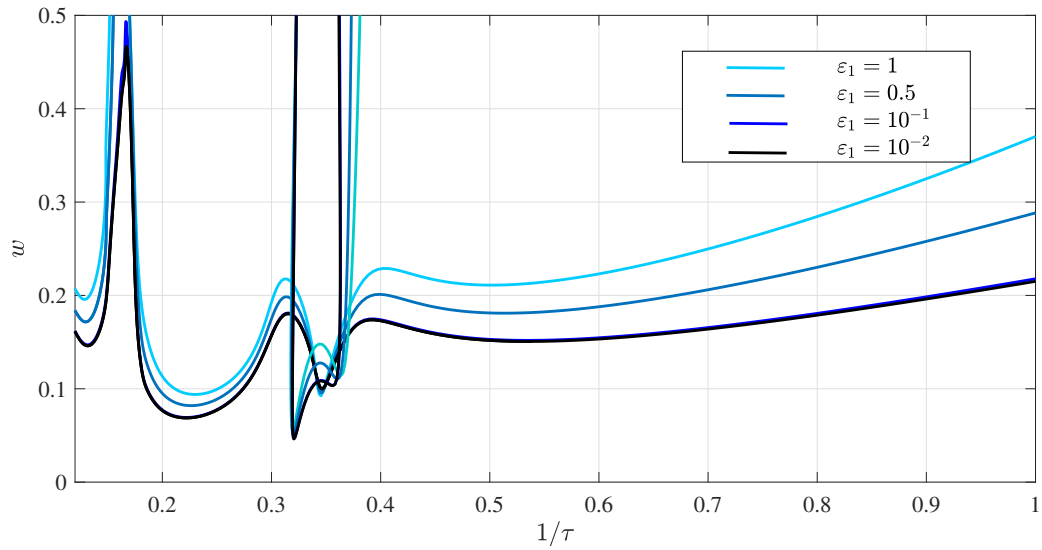

Figure 6.5: Effect of smoothing parameter ε_1 on the bifurcations of forced vibrations in half immersion milling case. $h_0 = 1$.

As shown in the figure, the convergence of bifurcation diagrams to a single curve as ε_1 tends to zero shows that smoothing by ε_1 dose not alter the dynamics near bifurcations if this parameter is selected small enough. This is also shown in Fig. 6.6 which shows the continuation of the branch of Torus bifurcations in parameters w and ε_1 at constant $\tau = 2$. The cutting depth at Torus bifurcation, w_{bif}, converges as ε_1 tends to zero.

The non-smoothness due to the loss of contact at negative chip thickness was smoothened by introducing three parameters ($\varepsilon_2, \varepsilon_3$ and ε_4) in section 6.1.3. These parameters can change the dynamics of the system significantly. However, for sufficiently small smoothing parameters, their effect on the location of the first bifurcations is negligible. Figure 6.7 shows the bifurcations diagram of half immersion milling without considering the effect of loss of contact and with considering this effect for different values of ε_2, ε_3 and ε_4. In this figure, only the Torus bifurcation of the first lobe is shown for better visibility. Similar behaviour was observed for period doubling branches. The dashed red line shows the Torus bifurcations of the system developed in section 6.1.2 (neglecting loss-of-contact) while the solid blue

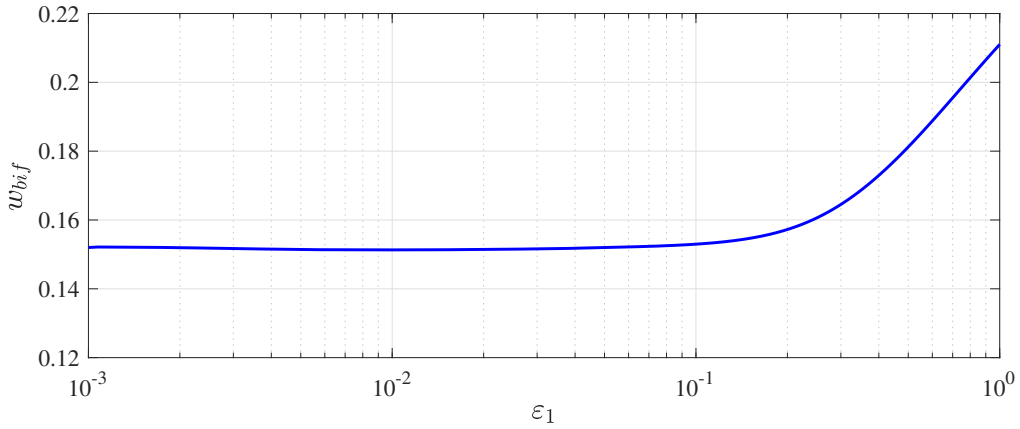

Figure 6.6: Sensitivity of the bifurcation cutting depth, w_{bif}, to the smoothing parameter ε_1 at constant $\tau = 2$ for half immersion milling case. $h_0 = 1$.

lines show the Torus bifurcations of the system developed in section 6.1.3 (considering loss-of-contact). The comparison shows that, by reducing the value of smoothing parameters, the Torus bifurcation diagrams of the smoothened system converge to the one obtained by neglecting loss of contact.

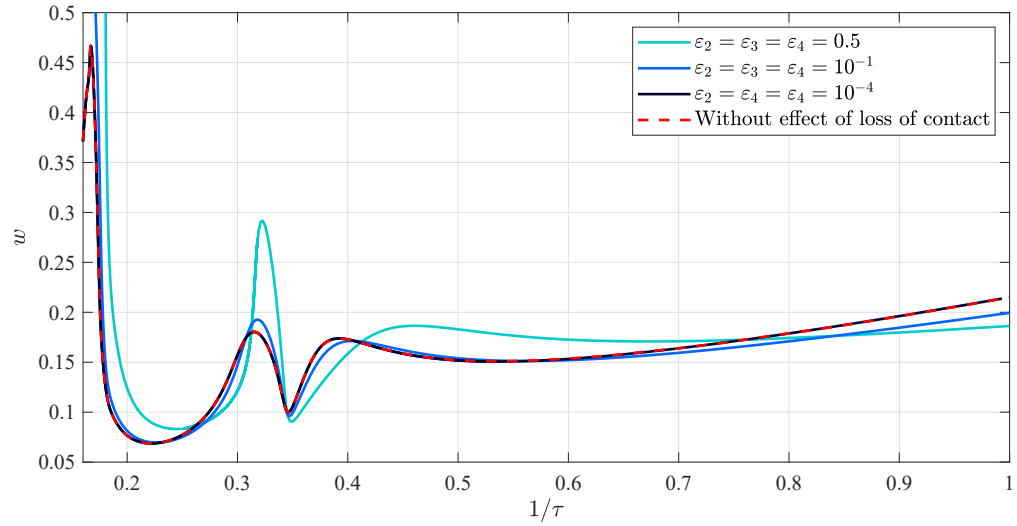

Figure 6.7: Effect of smoothing parameters ε_2, ε_3 and ε_4 on the Torus bifurcations of forced vibrations in half immersion milling case. $h_0 = 1$.

The negligible effect of loss of contact on the bifurcations of forced vibrations is explained due to the small amplitude of oscillations before the first bifurcation of the periodic solution. The amplitude of vibrations starts increasing after Torus

or period-doubling bifurcations, i.e. when the so-called chatter occurs. Therefore, we expect the smoothing parameters $\varepsilon_2, \varepsilon_3$ and ε_4 to have a significant effect on post-chatter dynamics [92]. The post-chatter bifurcations of the non-smooth system requires further investigations in future. Nonetheless, in practice, the location of the bifurcations of forced solutions is of primary interest, because the emerging high-amplitude vibrations after this point cause costly damages to the workpiece and the machine tool. Therefore, in this thesis, it is focused on the bifurcations of periodic forced vibrations; the dynamics after this bifurcation are only briefly discussed in section 6.2.5.

6.2.3 Effect of feedrate

In section 6.2.1, the forces generated by feed motion were ignored by setting $h_0 = 0$ to enable comparing continuation and SDM results. However, setting feedrate to zero eliminates forced vibrations and thereby the effect of structural nonlinearities on the dynamics during stable cuts. Consequently, the bifurcations diagram of the nonlinear system is similar to stability lobe diagrams of the underlying linear system, as shown in Figs. 6.2 and 6.4. In practice, however, structural nonlinearities become excited by the periodic feed-generated forces and distort the boundaries of the bifurcations. Figure 6.8 shows this effect for the full immersion case. In this figure, the diagrams of Torus bifurcations when the feedrate $h_0 = 1$ is considered in the force equation and when it is neglected ($h_0 = 0$) are shown. In the presence of feed-generated forces ($h_0 = 1$), periodic forced solutions in the green shaded region are stable while they are unstable in the red shaded region. The phase portrait of vibrations computed by the numerical integration of the (nonsmooth) exact equations at the two points A and B located in these two regions are also presented in Fig. 6.8. The numerical integration results validate the predictions of the bifurcation diagram obtained by considering the feed-generated forces. When the feedrate term is considered in the equations of motion, point A corresponds to stable periodic motion at the tooth-passing frequency, while point B shows a quasi-periodic motion resulting from Torus bifurcation.

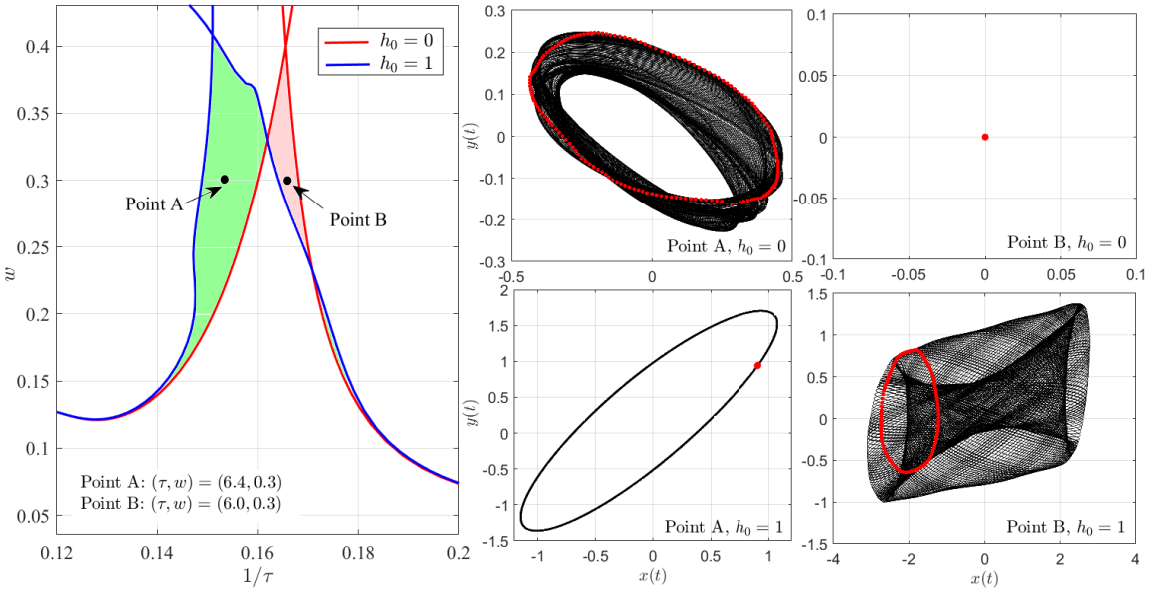

Figure 6.8: Effect of feed-generated forces on Torus bifurcation of the forced vibrations in the full immersion case. Phase portraits of points A and B are calculated by numerical integration of the exact model.

Note that at lower cutting depth values, w, the effect of feedrate on the location of Torus bifurcations is minimal because the amplitude of forced vibrations is small. Nonetheless, because inside the stability pockets the cutting depth w and thus the amplitude of forced vibrations are higher, nonlinearities are excited and the feedrate effect is prominent. This is also shown in Fig. 6.9. In this figure, the magnitudes of bifurcating depth of cut are shown for different feedrates (h_0) at constant $\tau = 6$ and $\tau = 6.4$, which are located at the two sides of the secondary Hopf-Hopf bifurcation point shown in Fig. 6.2. A similar analysis was conducted for $\tau = 4$ and $\tau = 3.13$, which respectively correspond to the points with minimum w on the Torus and period-doubling curves in Fig. 6.2. The variations of stability limit at $\tau = 4$ and $\tau = 3.13$ are negligible compared to the points inside the stability pockets.

The results of a similar analysis performed for the half immersion case are shown in Fig. 6.10. Considering the effect of feedrate, forced vibrations at any point inside the green region are stable, as validated by the numerical integration of the exact model at points A and B.

The effect of feedarate is omitted from modelling regenerative chatter in linear systems, but the results of this section confirm that it should be considered in the presence of structural nonlinearities. As shown in Figs. 6.8-6.10, changes in the

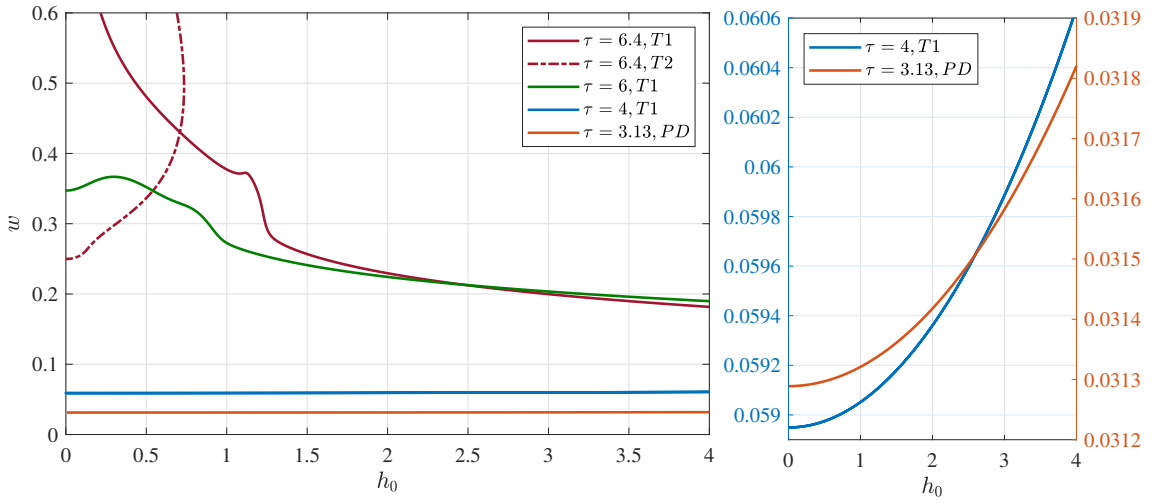

Figure 6.9: Numerical continuation of Torus and Period-Doubling bifurcations in h_0 and w parameter space for the full immersion case. $T1$ shows the first (lobe) branch of Torus bifurcation, $T2$ shows the second (lobe) branch of Torus bifurcations, and PD shows the Period Doubling branch.

chatter-free region due to feedrate can be especially significant in regions with higher feed-generated forces, i.e. inside the stability pockets where cutting depth is higher. For example, at $\tau = 6.4$ in Fig. 6.8 (the same speed as point A), the stability limit roughly doubles after considering the effect of feed-generated forces. However, at the regions near point B, stability limit decreases by about 30%. Similarly significant changes in stability are observed for the half immersion case shown in Fig. 6.10.

6.2.4 Effect of structural nonlinearities

Since the effect of feedrate on chatter stability depends on the extent of structural nonlinearities, the range of structural nonlinearities that would considerably change the stability borders is studied in this section. For this purpose, the non-dimensional feedrate is kept constant at $h_0 = 1$ and the vector of nonlinear restoring forces is rewritten in the following form:

$$\mathbf{f}_n\left(\mathbf{X}, \dot{\mathbf{X}}\right) = \upsilon \mathbf{C}_3 \dot{\mathbf{X}}^{o3} + \kappa \mathbf{K}_3 \dot{\mathbf{X}}^{o3} \tag{6.27}$$

where the non-dimensional coefficients υ and κ are introduced to study the extend of nonlinearity in damping and stiffness, respectively. For $\upsilon = \kappa = 1$, the restoring forces are as the same as the original system reported in Table 6.2. In Fig. 6.11(a), the

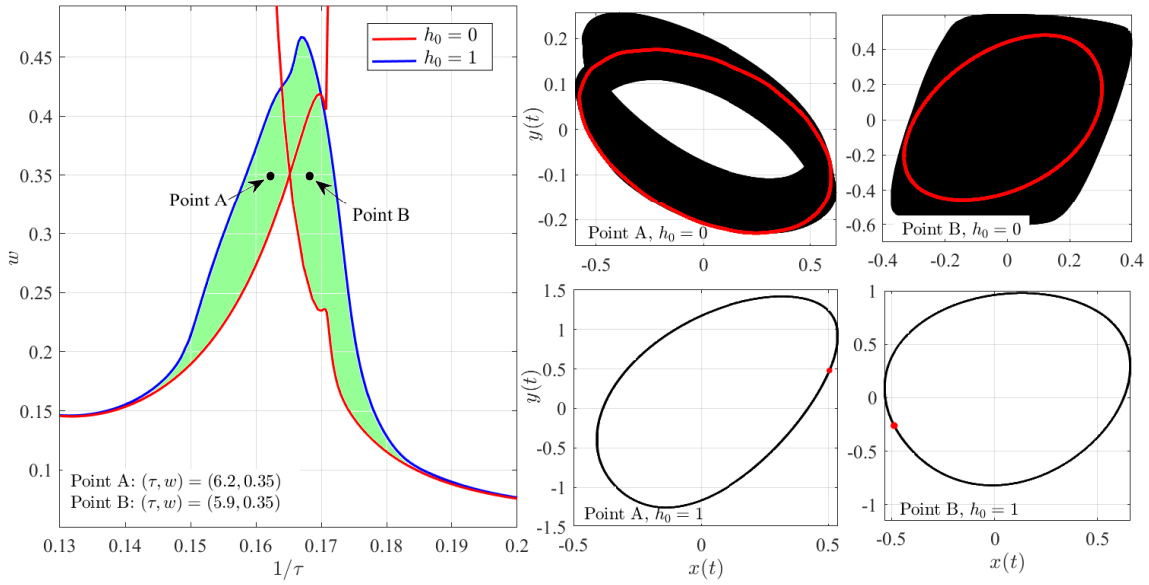

Figure 6.10: Effect of feedrate h_0 on Torus bifurcations of forced periodic solutions in case of half immersion milling. Phase portraits of points A and B are calculated by numerical integration of the exact model.

Torus bifurcation branch is continued in (w, κ), keeping $\upsilon = 1$ constant, for the full immersion case; in part (b) of the figure, continuation is performed in (w, υ) for the constant $\kappa = 1$. In this Figure, time delay is assumed to be $\tau = 4$, which corresponds to the point with minimum w on the Torus curve in Fig. 6.2. The results show that nonlinear damping has a greater effect than stiffness at this particular spindle speed. Nonlinear stiffness has an insignificant effect even at higher values of κ.

Nonlinearities cause a more considerable change in bifurcations at spindle speeds close to the secondary double Hopf point, i.e. inside the stability pockets. This is shown in Fig. 6.12, where the results of similar continuations are presented but at $\tau = 6$ and $\tau = 6.4$. The change in the bifurcation cutting depth is significant in both (w, υ) and (w, κ) continuations. Small changes in the nonlinear parameters cause a considerable variation in bifurcation cutting depth.

The nonlinear model parameters are subjected to modeling uncertainties and identification errors. While a formal robustness analysis of the presented model predictions requires a dedicated study in the future, diagrams in Figs. 6.11 and 6.12 provide an elementary understanding of the sensitivity of the model predictions to such errors. Note that all of the model parameters, including linear modal constants and the force model parameters, are susceptible to modeling and identification errors and

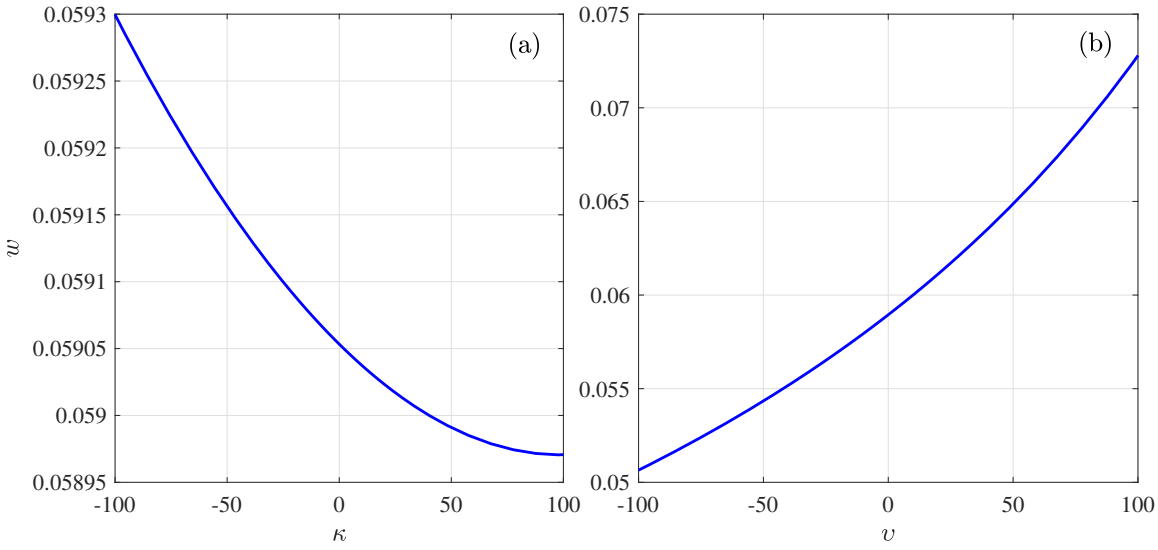

Figure 6.11: Continuation of Torus bifurcations branch for full immersion milling at $\tau = 4$ in the parameters (a) κ and w when $\upsilon = 1$ (b) υ and w when $\kappa = 1$.

also affect the robustness of the model predictions [114, 115].

6.2.5 Dynamics after bifurcation

After Torus bifurcation, the forced periodic solution loses stability and new solution emerges. The new solution can be either periodic or quasi-periodic, depending on the rotation number, which is defined as the ratio of the forcing period (here, the spindle rotation period) to the period of the new emerging solution, shown as p/q. If the rotation number is irrational, the solution after Torus bifurcation is quasi-periodic and the phase portrait of sampled data do not form a closed trajectory. If the rotation number is rational, the new solution is periodic with a period of q times of the forcing period; usually called resonant periodic or mode-locked solution and are shown with the label $p : q$. The rotation number calculated in DDE-BIFTOOL for the Torus bifurcation at the first lobe for full immersion milling is shown in Fig. 6.13. The rotation number $p : q$, with a rational ratio, are given at pints PA to PD. At these points, the time history and phase portrait of vibrations right after the Torus bifurcation are calculated by numerical integration of the exact model. Sampled data at the tooth passing frequency for steady state part of the solution are shown by yellow colour. The points with the red colour are the same but for a small time interval. According to the phase portraits, sampled vibrations at all of the points

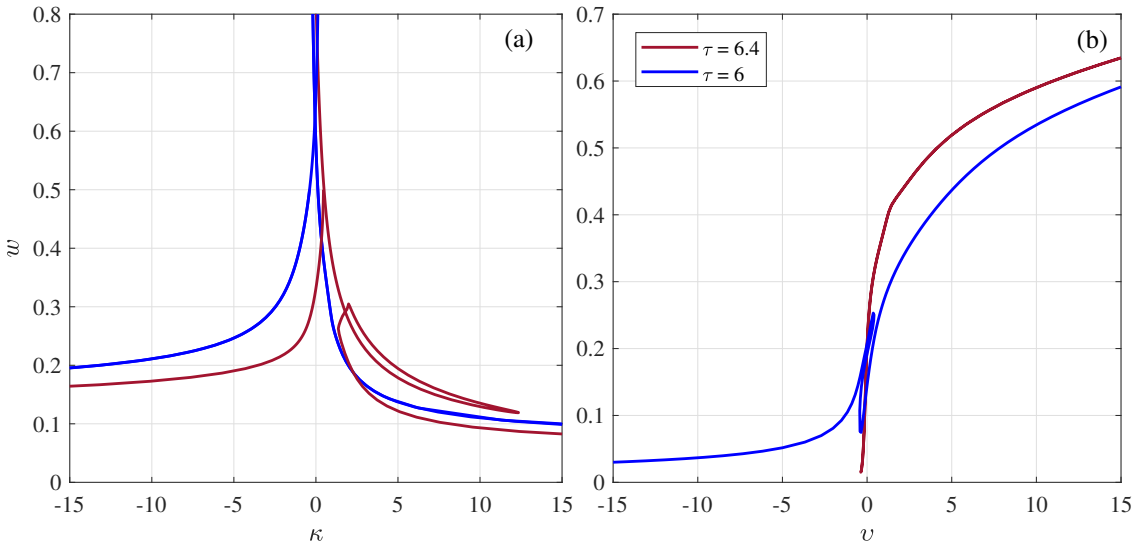

Figure 6.12: Continuation of Torus bifurcations for full immersion milling at $\tau = 6$ and $\tau = 6.4$ in the parameters (a) κ and w when $\upsilon = 1$ (b) υ and w when $\kappa = 1$.

(PA-PD) form a closed trajectory, meaning that the vibrations after bifurcation are also periodic. At points PA and PB, the denominators q are 5 and 3, respectively. It also can be seen that there are 5 and 3 lines formed by the sampled points in the time history of vibrations. At points PC and PD, the denominators q are 4 and 2, respectively. However, the number of lines formed by the sampled data are 8 and 4, respectively. The number of lines is twice the corresponding q because the data are sampled at tooth passing frequency which is twice of the forcing frequency in our formulation, i.e. spindle frequency. Since $N = 2$, for all the points with even q, the number of lines formed by sampled data in time history is twice q. This does not happen for odd q numbers.

The branch of new periodic solutions after the Torus bifurcation, with the period of q times the forcing period, can be continued in DDE-BIFTOOL. However, as discussed earlier, after Torus bifurcation, loss of contact dominates the dynamics and the approximation of the exact model with the smooth model requires careful considerations. Figure 6.14 shows the amplitude of periodic solutions at τ=4.17 in x and y directions. For cutting depths w below the bifurcation point w_{bif}, the amplitude corresponds to the amplitude of forced vibrations. After bifurcation, the graph shows the amplitude of vibrations in the branch of the 1:3 resonant periodic solutions (shown in Fig. 6.13 as point PB). The branch is continued for both cases of ignoring and considering loss of contact. In both cases, the bifurcation type is

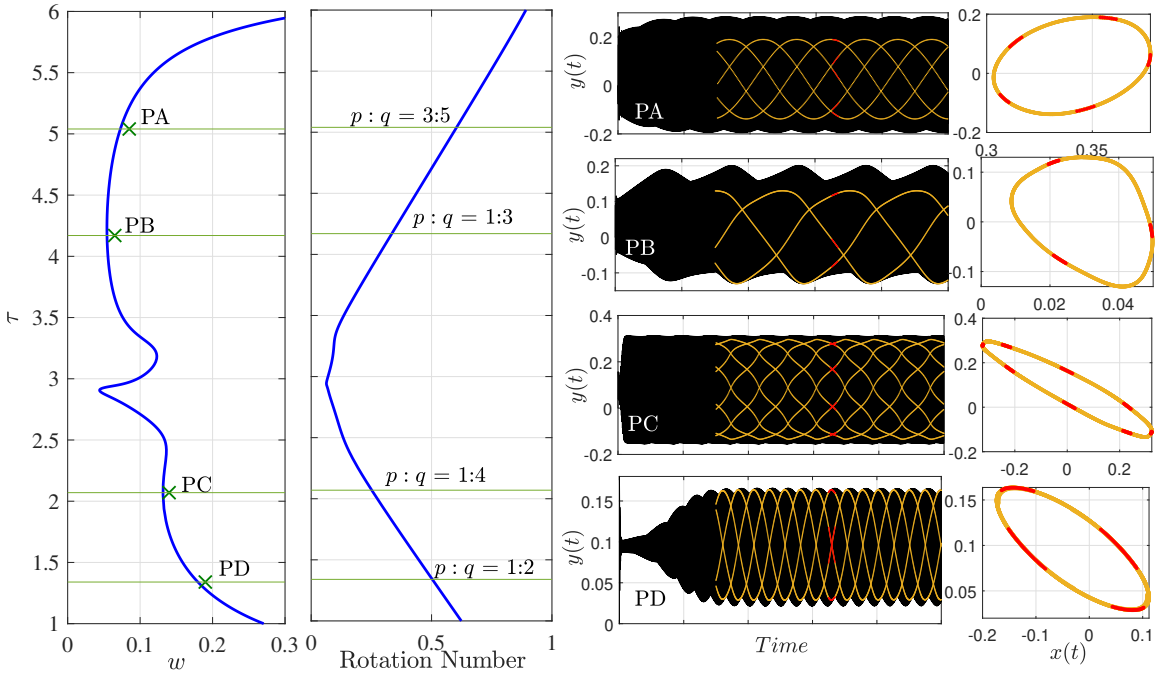

Figure 6.13: Rotation number at the Torus bifurcation of the first lobe for full immersion milling case and numerical integration results for points PA :$(\tau, w) = (5.04, 0.085)$, PB :$(\tau, w) = (4.17, 0.065)$, PC :$(\tau, w) = (2.07, 0.14)$, and PD :$(\tau, w) = (1.34, 0.19)$.

supercritical. However, when loss of contact is considered, the continuation of the new periodic branch fails as w increases. Exploring the reasons and effects of the smoothening on post-chatter vibrations requires another study and is beyond the scope of this paper.

6.2.6 Practical considerations

The bifurcation diagrams generated in previous sections provide a theoretical insight into the extent to which structural nonlinearities change the stability of forced vibrations. Nonetheless, to keep the focus of the study on the effect of structural nonlinearities, in Section 3, simplifying assumptions were considered that may be violated in practice. For example, the presence of closely-spaced modes and the nonlinear coupling between them, pose-dependent dynamics and its variation under operational conditions, un-modelled degrees of freedom (e.g. axial and torsional), cutting force nonlinearities, and runout were neglected in this study but they may offset the influence of structural nonlinearities on chatter stability in practice. Because of such

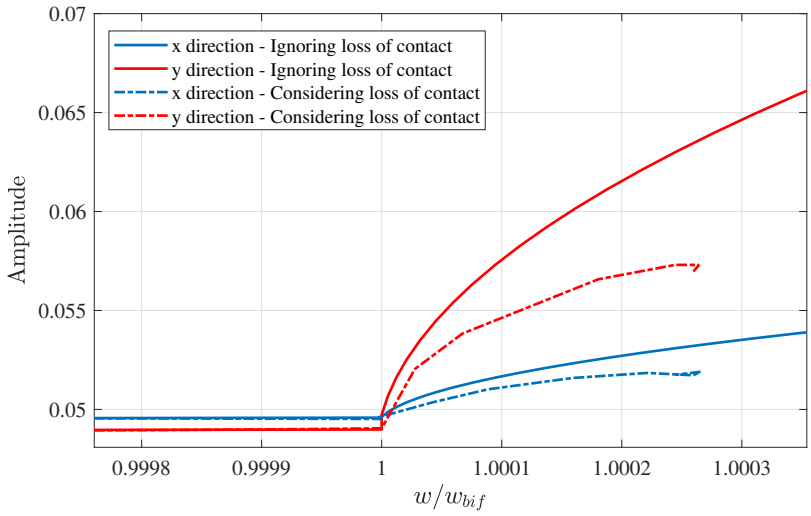

Figure 6.14: Amplitude of periodic vibrations at τ=4.17 before and after the Torus bifurcation for full immersion milling case.

factors, it is practically difficult to isolate the effect of structural nonlinearities and verify the presented results with experiments.

6.3 Conclusions

Regenerative chatter in milling with robots that exhibit structural nonlinearities was studied. Robot's dynamics at the TCP was modelled by a 2DOF vibratory system with cubic stiffness and damping. The milling forces were modelled as non-smooth time-periodic functions of the current and delayed vibrations. After smoothening the equations of motion, numerical continuation was used to study the secondary Hopf and period-doubling bifurcations of the forced periodic vibrations. A case study conducted on a KUKA KR90 R3100 robotic milling arm showed that feedrate, which does not affect chatter in machine tools with a linear structure, alters chatter stability in milling with structurally nonlinear robots. The total stiffness and damping of the studied system depend on vibration amplitude. Changing the feedrate alters the amplitude of forced vibrations and consequently the system's damping and stiffness. As a result, chatter stability changes by feedrate. In linear systems, feedrate does not affect chatter stability because the linear system's stiffness and damping are independent of vibration amplitude.

The scope of this study was limited to the secondary Hopf and the first period-

doubling bifurcations of forced vibrations. From a technological point of view, this bifurcation point determines the chatter-free cutting parameters (e.g. spindle speed and depth of cut) and thus is of the greatest importance. Nonetheless, studying the bifurcations of the new solutions that emerge after chatter is also critical for understanding the process dynamics. Post-chatter dynamics is strongly affected by loss-of-contact non-smoothness which may not be addressed efficiently by the presented method and requires further studies in future.

Chapter 7

In-process Frequency Response Function measurement for robotic milling

The bifurcation analysis presented in the previous chapter provided stability diagrams of milling process which potentially can be used for adjusting cutting strategies to improve productivity. However, employing such analysis require the accurate modelling of structural dynamics as shown in Chapters 4 and 5. From an industrial point of view, this procedure is indeed expensive and requires plenty of time and effort. In addition, the simplifying assumptions such as ignoring the nonlinear coupling of the vibrations modes (especially closely-spaced modes), the effect of feed motion [74] and runout in cutting forces [109], which each can affect the dynamic response, can be violated in practice. To address these issues, a different approach is considered in this chapter in order to predict accurate stability diagrams of robotic milling systems with less effort and time. The proposed approach is based on measuring FRF of the robotic milling system during the process and then employing linear chatter analysis. The FRF that are measured during the process represent dynamics of the nonlinear system linearized about the operational condition and account for the effects of structural nonlinearities, feed motion, and any other unknown sources that may affect the system dynamics during machining. In this chapter, two new methods for measuring in-process FRF of the Multi-Input Multi-Output (MIMO) milling system are presented. The presented methods are applied to measure the in-process FRF of the machining robot and construct the corresponding SLD.

7.1 Dynamics

The dynamics of milling process was introduced in the previous chapters. However, a brief summary is repeated here for ease of reading. Consider the 6-DOF articulated robotic arm performing milling operation shown in Fig.7.1. The robot is subjected to milling forces generated at its TCP (tool-tip) in the feed (X), normal (Y), and axial (Z) directions. Milling forces are modeled by linear model as a combination of periodic forces proportional to feedrate and transient forces proportional to the TCP's present and past elastic oscillations [116]:

$$\mathbf{F}(t) = \mathbf{F}_p(t) + aK_{tc}[\alpha(t)]\left\{\mathbf{X} - \mathbf{X}^{\tau}\right\} \tag{7.1}$$

where $\mathbf{F}(t)$ is the total forces applied at the TCP, and $\mathbf{F}_p(t) = \mathbf{F}_p(t+\tau)$ represents periodic forces with tooth-passing period, τ, as the principal period. Tooth-passing period, $\tau = 2\pi/N\Omega$, is inversely proportional to spindle speed (Ω) and the number of the cutting edges of the tool (N). The second term in Eq.7.1 represent the transient regenerative forces. Regenerative forces are proportional to the elastic displacement of the TCP in Cartesian frame, $\mathbf{X} = [x(t) \;\; y(t) \;\; z(t)]^T$, and its value one tooth-passing period prior, $\mathbf{X}^{\tau} = [x(t-\tau) \;\; y(t-\tau) \;\; z(t-\tau)]^T$. The constant K_{tc} is the force coefficient in the tangential direction [83] and a is the axial cutting depth, as shown in Fig.7.1(d). The matrix $[\alpha(t)] = [\alpha(t+\tau)]$ represents the periodic variation of the regenerative forces and their directions as the spindle rotates; therefore, its entries are periodic at the tooth-passing period, τ:

$$[\alpha(t)] = \begin{bmatrix} \alpha_{xx} & \alpha_{xy} & \alpha_{xz} \\ \alpha_{yx} & \alpha_{yy} & \alpha_{yz} \\ \alpha_{zx} & \alpha_{zy} & \alpha_{zz} \end{bmatrix} \tag{7.2}$$

where

$$\alpha_{xx} = \sum_{j=1}^{N} g(\varphi_j)\sin\varphi_j \sin\gamma\,(-\cos\varphi_j - k_{rc}\sin\varphi_j\sin\gamma - k_{ac}\sin\varphi_j\cos\gamma),$$

$$\alpha_{xy} = \sum_{j=1}^{N} g(\varphi_j)\cos\varphi_j \sin\gamma\,(-\cos\varphi_j - k_{rc}\sin\varphi_j\sin\gamma - k_{ac}\sin\varphi_j\cos\gamma),$$

$$\alpha_{xz} = \sum_{j=1}^{N} -g(\varphi_j)\cos\gamma\,(-\cos\varphi_j - k_{rc}\sin\varphi_j\sin\gamma - k_{ac}\sin\varphi_j\cos\gamma),$$

$$\alpha_{yx} = \sum_{j=1}^{N} g(\varphi_j)\sin\varphi_j \sin\gamma\,(\sin\varphi_j - k_{rc}\cos\varphi_j\sin\gamma - k_{ac}\cos\varphi_j\cos\gamma),$$

$$\alpha_{yy} = \sum_{j=1}^{N} g(\varphi_j) \cos\varphi_j \sin\gamma \left(\sin\varphi_j - k_{rc} \cos\varphi_j \sin\gamma - k_{ac} \cos\varphi_j \cos\gamma\right),$$

$$\alpha_{yz} = \sum_{j=1}^{N} -g(\varphi_j) \cos\gamma \left(\sin\varphi_j - k_{rc} \cos\varphi_j \sin\gamma - k_{ac} \cos\varphi_j \cos\gamma\right),$$

$$\alpha_{zx} = \sum_{j=1}^{N} g(\varphi_j) \sin\varphi_j \sin\gamma \left(-k_{rc} \cos\gamma - k_{ac} \sin\gamma\right),$$

$$\alpha_{zy} = \sum_{j=1}^{N} g(\varphi_j) \cos\varphi_j \sin\gamma \left(-k_{rc} \cos\gamma - k_{ac} \sin\gamma\right),$$

$$\alpha_{zz} = \sum_{j=1}^{N} -g(\varphi_j) \cos\gamma \left(-k_{rc} \cos\gamma - k_{ac} \sin\gamma\right).$$

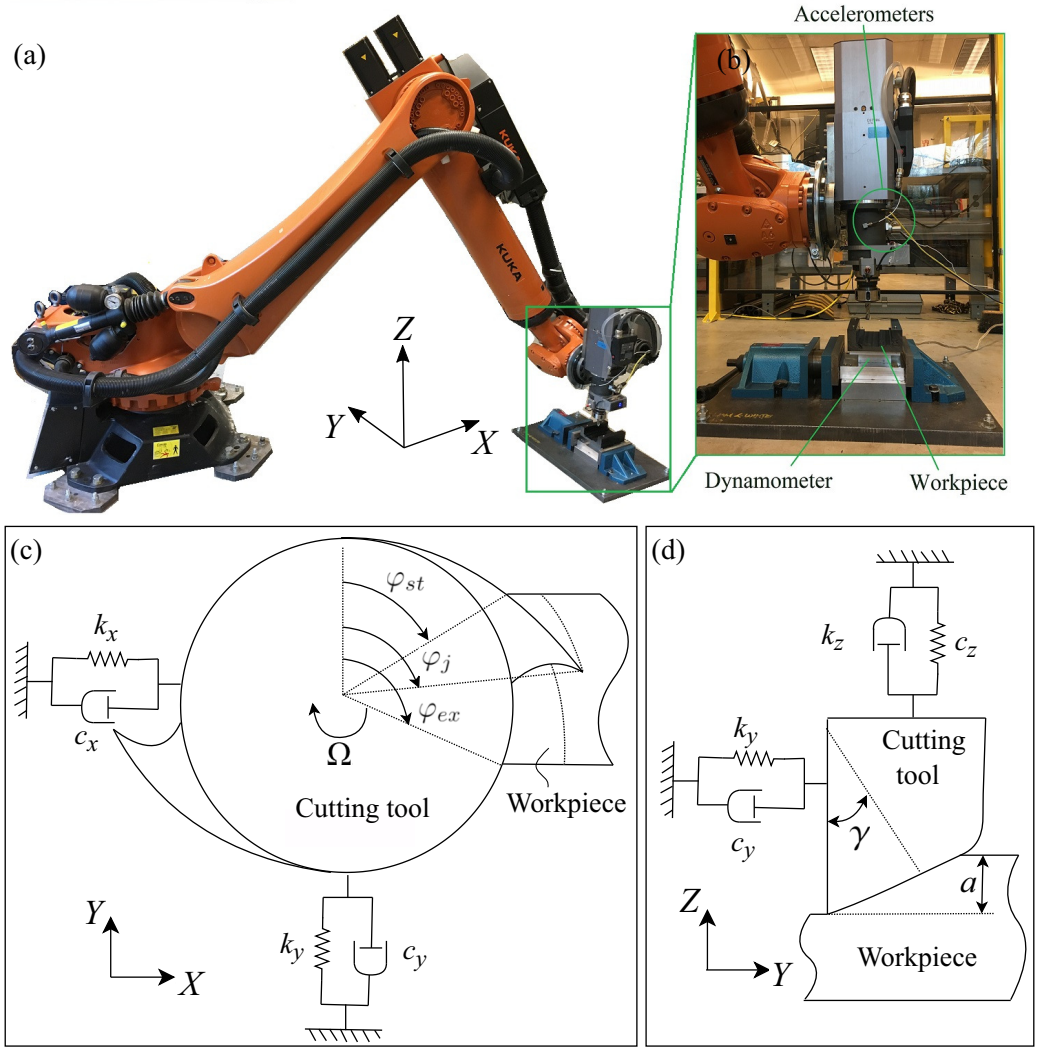

Figure 7.1: (a) Configuration of the KUKA KR90 R3100 robotic milling system. (b) the experimental setup used to measure in-process FRF. (c) and (d) 3DoF model of milling system.

The parameters k_{rc} and k_{ac} are force coefficients in the radial and axial directions, respectively, γ is the cutting edge angle, and $\varphi_j = \Omega t + (j-1)\frac{2\pi}{N}$ is the immersion angle of tooth j, as shown in Fig.7.1(c). The Heaviside function $g(\varphi_j)$ determines whether this angle is within the cutting immersion angle range bounded by the start and exit angles, φ_{st} and φ_{ex}, respectively:

$$g(\varphi_j) = u(\varphi_j - \varphi_{st}) - u(\varphi_j - \varphi_{ex}) \tag{7.3}$$

with $u(\cdot)$ being unit step function.

Following ZOA chatter analysis method, the periodic $[\alpha(t)]$ is approximated by $[\alpha_0]$, its average over one principal period[117]. Assuminga Linear-Time-Invariant system; the milling forces and the resulting oscillations in the Laplace domain can be mapped to one another via the system transfer function, as follows:

$$\mathbf{X}(s) = \mathbf{H}(s)\mathbf{F}(s) \tag{7.4}$$

where $\mathbf{H}(s)$ is the transfer function between Cartesian forces and oscillations at the TCP, assuming the system is linearized about its periodic response. Transforming Eq.7.1 to Laplace domain and substituting $\mathbf{X}(s)$ from Eq.7.4 leads to the following characteristic equation:

$$\det\left[\mathbf{I} - aK_{tc}[\alpha_0]\left(1 - e^{-s\tau}\right)\mathbf{H}(s)\right] = 0 \tag{7.5}$$

For any given axial depth of cut, a, and spindle speed $\Omega = 2\pi/N\tau$, stability of regenerative vibrations are determined according to Nyquist criterion applied to the characteristic equation.

In addition to the frequency domain approach, the Semi-Discretization Method (SDM) is also used. As explained in Cahpter 2, in SDM, the continuous-time equation is discretizied and the distributed-parameter system in Eq.7.1 is approximated by a lumped-parameter system described by its state transition matrix, $\mathbf{\Phi}$, as follows:

$$\mathbf{u}_{k+1} = \mathbf{\Phi}\mathbf{u}_k; k = 1, 2, .. \tag{7.6}$$

where $\mathbf{u}_k$ is the state vector of the lumped-parameter system. This system is asymptotically stable if and only if all of the eigenvalues of $\mathbf{\Phi}$ are inside the unit circle on the complex plane. In the frequency domain method, because the periodic coefficients are approximated by their average, Hopf-bifurcation is the only type of

stability loss that is predicted by this method. However, using SDM, both Hopf and period-doubling bifurcations of the system dynamics can be identified.

Both of the discussed frequency domain (ZOA) and discrete-time domain (SDM) approaches for predicting chatter stability require the TCP FRF or the modal parameters extracted from them. The transfer function $\mathbf{H}(s)$, or equivalently the Frequency Response Function $\mathbf{H}(i\omega)$, is usually determined by impulse hammer tests at the TCP while the machine tool or the robot is idle. While the TCP FRF measured in idle conditions remains relatively unchanged under operational (machining) loads in machine tools, it varies significantly in robotic machining, leading to inaccurate predictions of chatter stability. New in-process FRF measurement methods are presented in the next section to enhance the accuracy of chatter predictions by incorporating the true in-process dynamics of the robot in stability analysis.

7.2 In-process FRF measurement

The robotic milling setup, a KUKA KR90 R3100 robotic arm equipped by a Powertech 400 Hiteco milling spindle with HSK 63F holder interface, is shown in Fig.7.1. Figure 7.2 shows the FRF measured by impulse hammer tests in Cartesian coordinates at the robot's TCP (tool-tip) in the posture shown in Fig. 7.1. Excitation force was applied by a Kistler instrumented hammer and the resulting accelerations were measured using PCB piezoelectric accelerometers. This method of measuring TCP FRF has been adopted from machine tools where the FRF measured by hammer tests remain relatively unchanged under operational loads. However, these FRF could lead to incorrect stability prediction since, unlike in machine tools, FRF of the robot vary significantly by operational conditions as shown in Chapters 4 and 5. Figure 7.3, borrowed from Chapter 4, shows an example of FRF variations by operational conditions (i.e. excitation force). The TCP FRF in this figure are measured using sinusoidal excitation forces with different force amplitudes applied by a shaker, which are then compared to the FRF measured by transient forces applied by an instrumented hammer. Because the sinusoidal excitation forces excite the structural nonlinearities in the robot joints, the FRF peaks are systematically distorted by increasing the force amplitude. Considering such nonlinearities, it is expected that the robot FRF also change during the milling process where high amplitude periodic cutting forces replace the shaker forces.

Considering the FRF variation due to structural nonlinearities, feed motion or

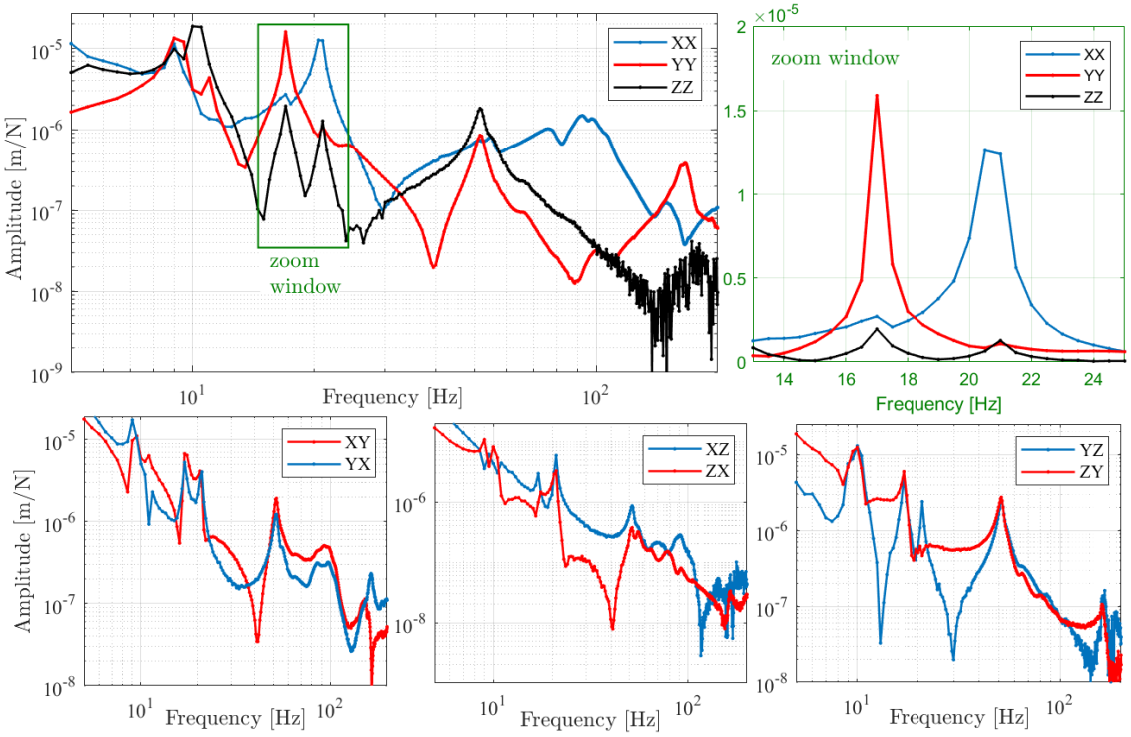

Figure 7.2: Measured FRF of the KUKA robotic milling system using impulse hammer tests in idle condition.

other unknown factors, it is aimed to predict the stability diagrams using the FRF that are measured during the milling operation, rather than in idle conditions. The milling forces are used as excitation forces and the corresponding vibrations are measured to determine the in-process FRF. Because chatter-free milling forces are periodic at the tooth-passing frequency ($\mathbf{F}_p(t)$ in Eq.7.1), they only excite the tooth-passing frequency and a few of its harmonics. Therefore, the resolution of the FRF estimated by those forces would be limited to the first few harmonics of tooth-passing frequency. Two approaches are considered to increase the bandwidth and resolution of the estimated FRF: i) milling porous material, and ii) milling homogeneous materials with varying spindle speed. In milling of porous materials, the random distribution of the pores adds a strong random component to the periodic milling forces, extending the bandwidth and resolution of excitation. In the second approach, the periodic content of the milling force at the tooth passing frequency is used for excitation, but the spindle rotation frequency is gradually swept across the frequency range where the flexible modes are located. The implementation of these two approaches are presented in the following sections. In the conducted experiments, cutting forces and the

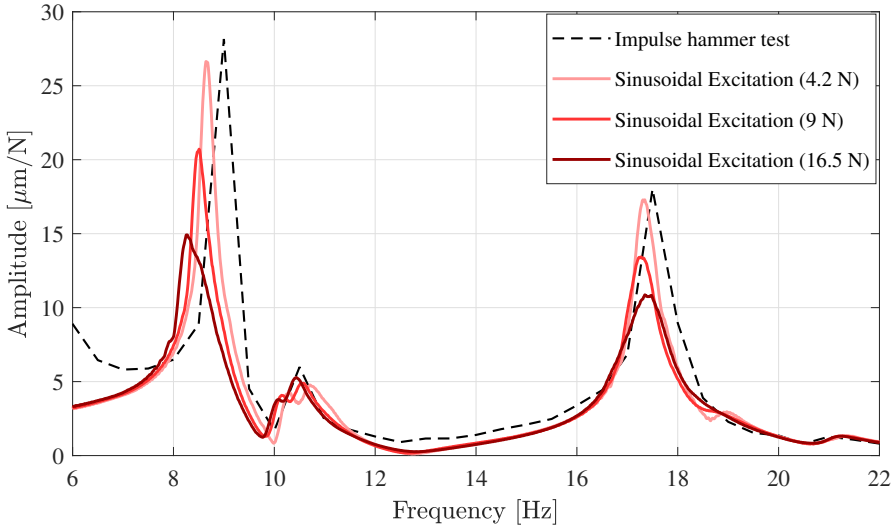

Figure 7.3: Variation of FRF measured using impulse hammer test and sinusoidal excitation force with different amplitudes [10].

resulting vibrations in feed, normal and axial directions were measured using a table dynamometer beneath the workpiece and accelerometers located at the non-rotating part of the spindle, respectively, as shown in Fig. 7.1. The data acquisition was carried out using CompactDAQ NI-9234 modules and the sampling rate was set to 10240 Hz.

7.2.1 Milling of porous material

The porous material used in this work is an Aluminum foam workpiece shown in Fig. 7.4. The random distribution of pores with random sizes enriches the frequency spectra of the periodic machining forces by superimposing a strong random content on them. The frequency spectra of cutting forces in milling of Aluminum foam and a homogeneous material (Acetal Copolymer) in similar conditions are shown in Fig. 7.4. Although the periodic content of the two signals have similar amplitudes, the average level of cutting forces at non-harmonic frequencies is considerably increased in the case of Aluminum foam.

Full immersion ($\varphi_{st} = 0$, $\varphi_{ex} = \pi$) milling was performed on the Aluminum foam with an endmill that had diameter of 12.7 mm and two cutting teeth (with $\gamma = \pi/2$). Axial cutting depth was a =2 mm and the feed motion was at the rate of 0.1 mm/tooth in X direction. The spindle speed was kept constant at 820 rev/min. This spindle speed was selected to prevent aligning the spindle rotation frequency

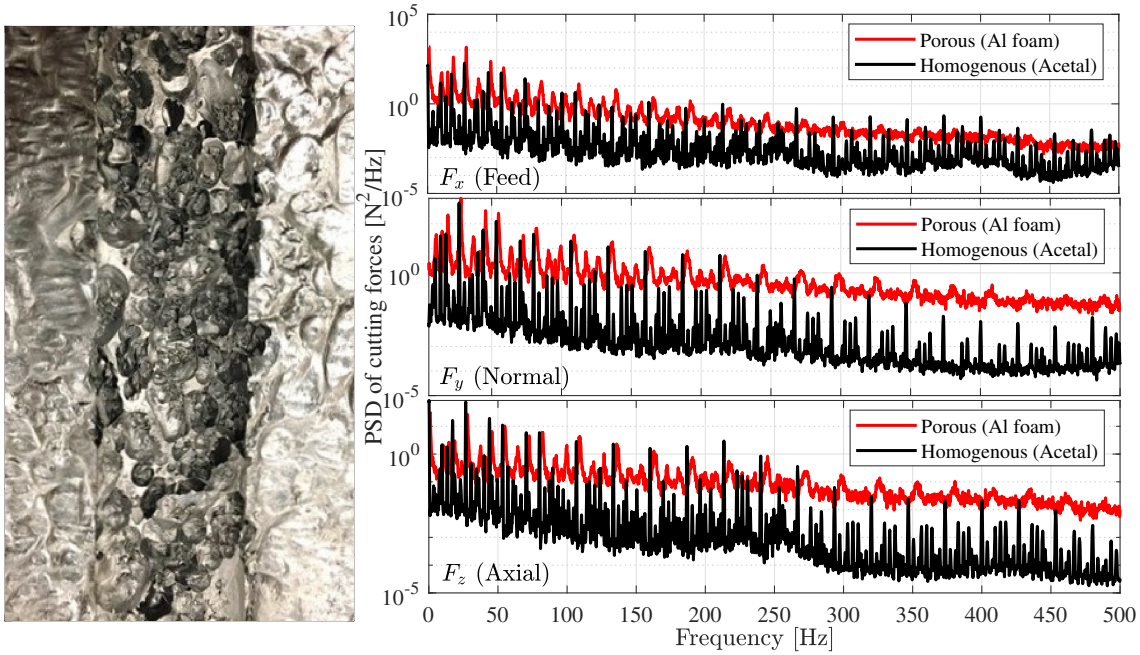

Figure 7.4: Left: Aluminum foam sample with density 0.36 g/cm^3. The middle channel shows the surface after machining.
Right: PSD of cutting forces in Aluminum foam milling (820 rev/min -0.1 mm/tooth -2 mm depth of cut) compared to Acetal milling (800 rev/min - 0.15 mm/tooth - 2 mm depth of cut).

(13.7 Hz) and its harmonics with the flexible modes of the robot. Note, since the flexible modes are below 30 Hz, a higher spindle speed could also be used to bypass all the flexible modes. However, 820 rev/min was selected to measure data for a longer time (considering the feedrate) while the change in robot's posture throughout the cut is minimum. The measured cutting forces are shown in Fig. 7.5(a) to (c). The Power Spectral Density (PSD) of the forces are shown in Fig. 7.4.

The FRF matrix between the vector of inputs $\mathbf{F} = [F_x \quad F_y \quad Fz]^T$ and the vector of outputs $\mathbf{X} = [x \quad y \quad z]^T$ of the MIMO system is calculated as follows [118]:

$$\mathbf{H}(\omega) = \mathbf{S_{XF}}(\omega)\mathbf{S_{FF}^{-1}}(\omega) \tag{7.7}$$

where

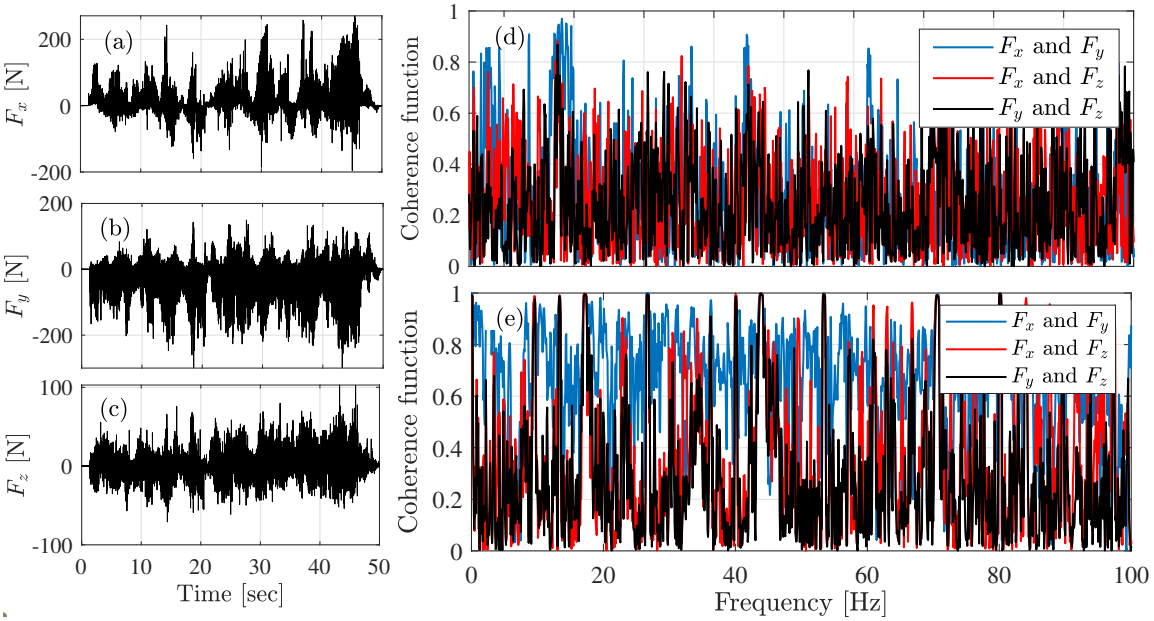

Figure 7.5: (a)-(c): Measured cutting forces in full-immersion milling of Aluminum foam, in feed, normal and axial directions, respectively. (d)-(e) The correlation between cutting forces in foam and Acetal milling tests, respectively.

$$\mathbf{H}(\omega) = \begin{bmatrix} H_{xx}(\omega) & H_{xy}(\omega) & H_{xz}(\omega) \\ H_{yx}(\omega) & H_{yy}(\omega) & H_{yz}(\omega) \\ H_{zx}(\omega) & H_{zy}(\omega) & H_{zz}(\omega) \end{bmatrix}, \mathbf{S_{XF}}(\omega) = \begin{bmatrix} S_{x,F_x}(\omega) & S_{x,F_y}(\omega) & S_{x,F_z}(\omega) \\ S_{y,F_x}(\omega) & S_{y,F_y}(\omega) & S_{y,F_z}(\omega) \\ S_{z,F_x}(\omega) & S_{z,F_y}(\omega) & S_{z,F_z}(\omega) \end{bmatrix}$$

$$\mathbf{S_{FF}}(\omega) = \begin{bmatrix} S_{F_x,F_x}(\omega) & S_{F_x,F_y}(\omega) & S_{F_x,F_z}(\omega) \\ S_{F_y,F_x}(\omega) & S_{F_y,F_y}(\omega) & S_{F_y,F_z}(\omega) \\ S_{F_z,F_x}(\omega) & S_{F_z,F_y}(\omega) & S_{F_z,F_z}(\omega) \end{bmatrix} \tag{7.8}$$

$H_{p,q}(\omega)$ is the frequency response function between the output p and the input q, and $S_{p,q}(\omega)$ is the cross PSD between signals p and q. The PSD, $S_{p,q}(\omega)$, was estimated by Welch's method and Hamming window with 50% overlap for averaging. In order to estimate the FRF matrix from Eq.7.7, the input signals (excitation forces) must to be linearly independent to avoid singularity of the inputs matrix $\mathbf{S_{FF}}$. This condition is confirmed by calculating the coherence between the cutting forces. The coherence function between two forces F_m and F_n is calculated as follows [118]:

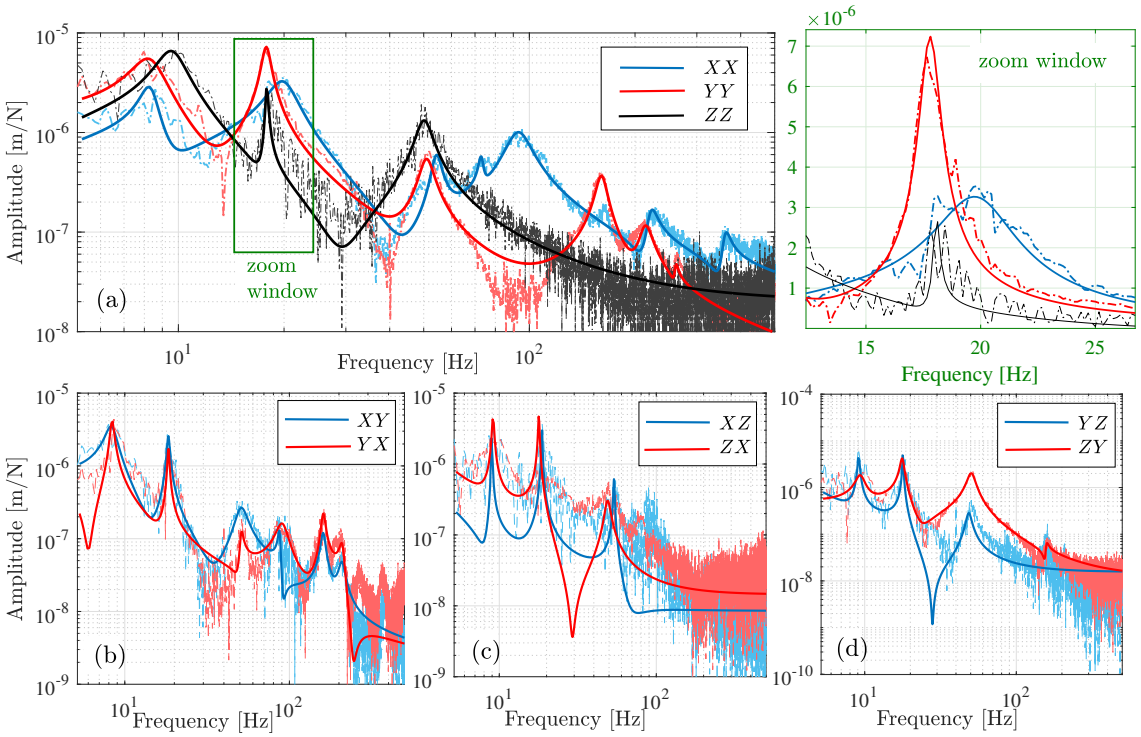

Figure 7.6: Calculated FRF in Cartesian coordinates using the signals obtained from milling of Aluminum foam.

$$C_{F_m,F_n}(\omega) = \frac{|S_{F_m,F_n}(\omega)|^2}{S_{F_m,F_m}(\omega)S_{F_n,F_n}(\omega)}, \quad m,n = x,y,z \tag{7.9}$$

The coherence between foam milling forces are shown in Fig. 7.5(d), which indicate that the forces are largely uncorrelated and therefore suitable for identification in Eq.7.7. In Fig. 7.5, for comparison, the coherence between milling forces in homogeneous material (Acetal) are also shown in part (e). Homogeneous material milling forces are linearly dependent at tooth passing frequency and its harmonics. Even at other frequencies, the lateral forces have higher correlation compared to the forces in foam milling. According to the coherence plots in Fig. 7.5(e) and Fig. 7.4, foam milling provides less correlated forces with higher amplitude random content. The force and acceleration signals measured during milling Aluminum foam were used in Eq.7.7 to estimate the in-process FRF shown in Fig. 7.6. The dashed lines show the identified FRF and the solid lines are the FRF fitted by modal analysis. The zoom window shows the most flexible modes in feed (X) and normal (Y) directions. It will be shown in Section 7.3 that these modes become unstable during machining and

cause chatter; therefore, we are mainly interested in the accurate estimation of the FRF in the vicinity of these modes.

As shown in Fig. 7.6, the frequencies of the most flexible modes of the robot are below 30 Hz. Variance of the estimated FRF in this range is studied using the multiple coherence function between the output p and the inputs $\mathbf{F}$ defined as follows [119]:

$$C_{p,\mathbf{F}}(\omega) = \frac{\mathbf{S}_{p,\mathbf{F}}^{H}(\omega)\mathbf{S}_{\mathbf{FF}}^{-1}(\omega)\mathbf{S}_{p,\mathbf{F}}(\omega)}{S_{pp}(\omega)}, \qquad p = x, y, z \tag{7.10}$$

where

$$\mathbf{S}_{p,\mathbf{F}}(\omega) = \begin{bmatrix} S_{p,F_x} & S_{p,F_y} & S_{p,F_z} \end{bmatrix}^T \tag{7.11}$$

The superscript H stands for Hermitian transpose. The calculated multiple coherence function, between the x, y and z vibrations and the input forces, are shown in Fig. 7.7. The coherence function is close to unity in the vicinity of the flexible modes, confirming the acceptable variance of the estimated FRF in this range. Because the axial machining forces are usually significantly smaller than the lateral forces, the measured signals in z direction have a lower Signal to Noise Ratio and consequently the coherence in that direction is lower than lateral directions.

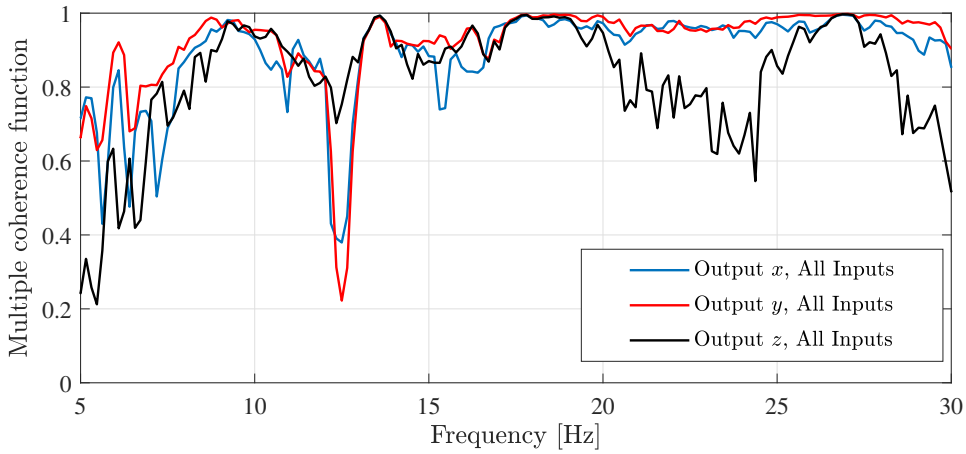

Figure 7.7: Multiple coherence functions corresponding to the FRF measured in foam milling test.

7.2.2 Speed-sweep milling of homogeneous materials

In the previous section, the in-process FRF were estimated during milling porous materials. Using this approach, all of the flexible modes of the system can be identified with a single test. However, since the excitation energy is distributed over a wide range of frequencies, variance of the estimated FRF close to the less flexible modes may be poor. Spindle speed sweep tests proposed in this section enable concentrating the excitation energy in the frequency range of interest to improve the estimation variance in the vicinity of the specific mode(s) that are more prone to chatter. In this approach, the periodic component of the cutting forces ($\mathbf{F}_p(t)$ in Eq.7.1) is used for excitation by sweeping the tooth-passing frequency across the frequency range of interest, i.e. where the flexible mode(s) of the system are located. To remove the correlation between the periodic milling forces in various directions, multiple (minimum three) cutting tests with different radial engagement conditions are conducted to form a full-rank matrix of inputs in Eq. 7.7. In this approach, the MIMO FRF are estimated using the same equation as Eq. 7.7, except that the $\mathbf{S_{FX}}$ and $\mathbf{S_{FF}}$ are defined as follows:

$$\begin{aligned} \mathbf{S_{XF}} &= \begin{bmatrix} \mathbf{S_{XF},1} & \mathbf{S_{XF},2} & \mathbf{S_{XF},3} \end{bmatrix}, \\ \mathbf{S_{FF}} &= \begin{bmatrix} \mathbf{S_{FF},1} & \mathbf{S_{FF},2} & \mathbf{S_{FF},3} \end{bmatrix} \end{aligned} \tag{7.12}$$

where the digits in the subscript denote the index of the conducted test. We used three different milling modes (i.e. radial engagements) that generate cutting forces with a different phase and/or amplitude in each test. The three milling tests were 1) central-milling ($\varphi_{st} = 0.38\pi$, $\varphi_{ex} = 0.61\pi$), 2) down-milling ($\varphi_{st} = 0.77\pi$, $\varphi_{ex} = \pi$) and 3) up-milling ($\varphi_{st} = 0$, $\varphi_{ex} = 0.23\pi$). The axial cutting depth was 2 mm in all of the tests. The workpiece was Acetal Copolymer. The spindle speed in each test swept from 450 rev/min to 690 rev/min over nearly 60 seconds, which corresponds to the tooth passing frequency increasing from 15 to 23 Hz. This is the range in which the flexible chatter-prone modes of the system are located, as will be shown in Section 7.3. Figure 7.8 shows the spectrogram (using short-time Fourier transform) of the cutting forces in test 2, i.e. the down-milling test. As expected, most of the excitation energy is concentrated between 15 and 23 Hz and its harmonics. The high energy at the spindle rotation frequencies are due to runout. The measured cutting forces in the three milling modes are shown in Fig. 7.9. The PSD of the cutting forces are also shown in the same figure. It can be seen that excitation power is uniformly distributed across the frequency range of interest.

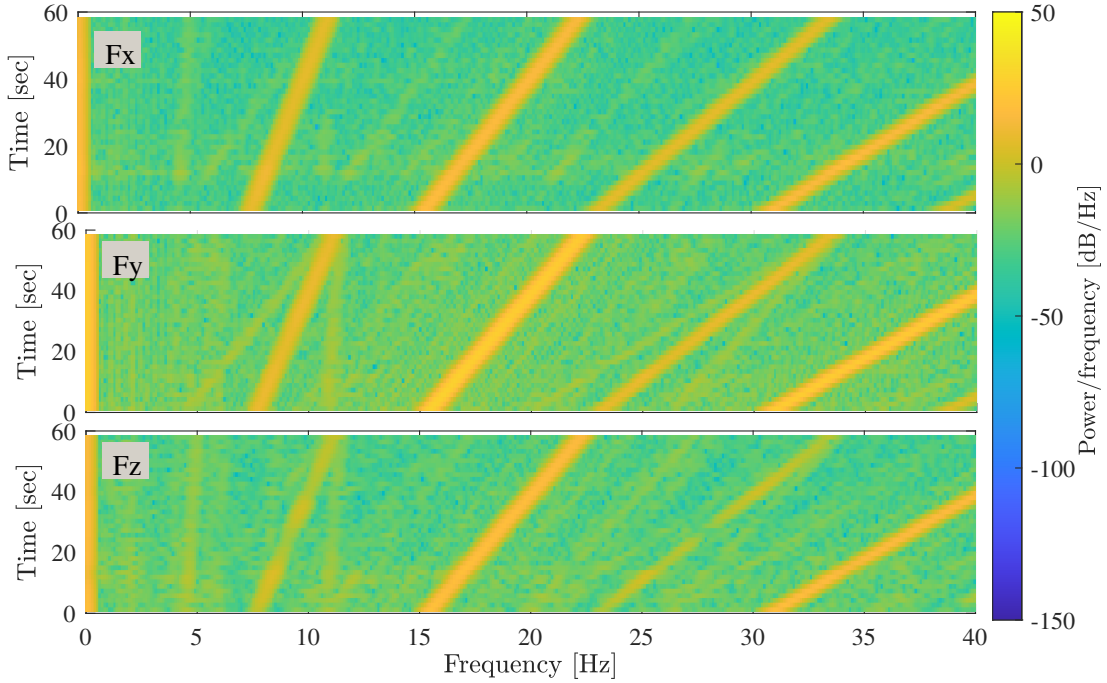

Figure 7.8: Spectrogram of the cutting forces in down-milling (test 2) speed-sweep test.

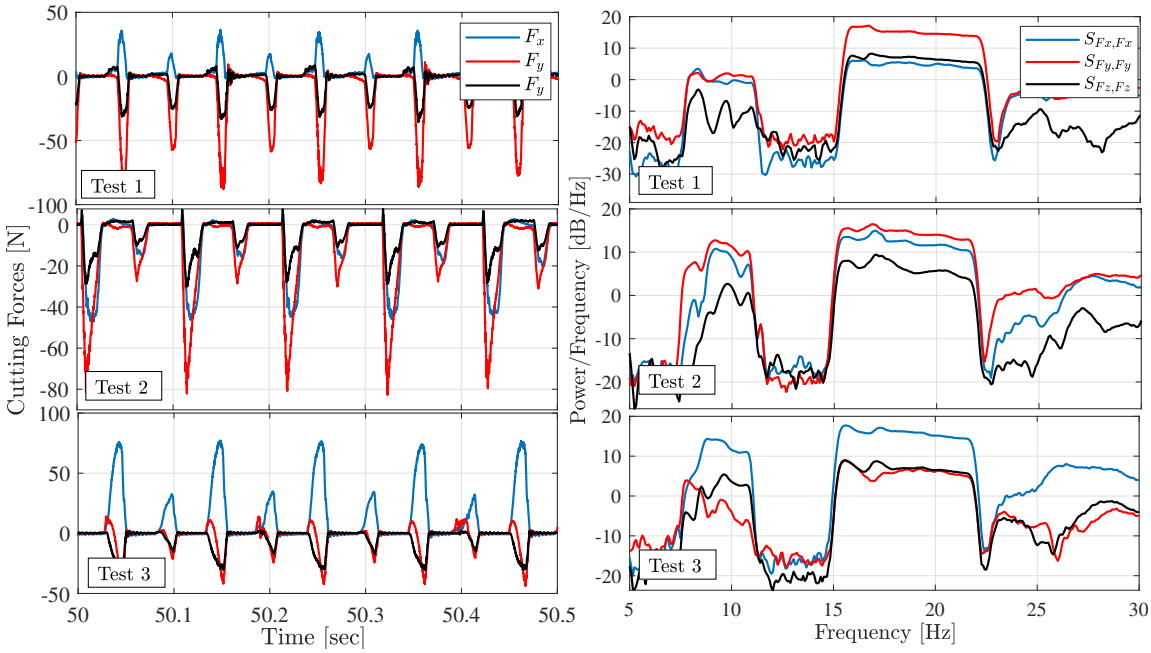

Figure 7.9: Measured cutting forces and their power spectral densities in speed sweep tests.

The coherence functions between the cutting forces are shown in Fig. 7.10, which indicates that the forces in each test are totally correlated, as expected for milling of a homogeneous material. However, since three different milling modes are used, the matrix of inputs $\mathbf{S_{FF}}$ in Eq. 7.12 has three significant (non-zero) singular values, therefore it is full-rank and the FRF of the MIMO system can be estimated. The in-process FRF estimated in speed-sweep tests are presented in Fig. 7.11. As shown in this figure, the modes in the target range are well-identified. The results of two series of speed sweep tests with the same cutting parameters are presented in Fig.7.11 to confirm the repeatability of FRF estimations. Note that the multiple coherence function as defined in Eq. 7.10 cannot be used for the speed sweep tests, because signals from different tests are being used.

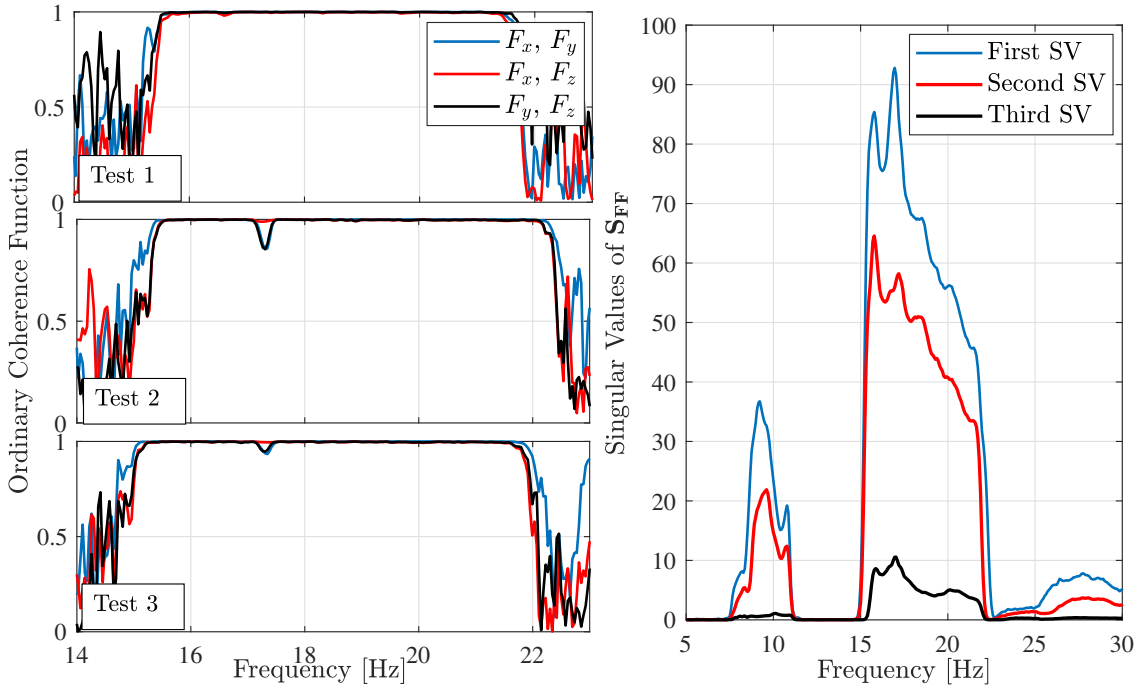

Figure 7.10: Coherence of measured cutting forces in speed sweep tests, and the singular values of the the matrix of input forces $\mathbf{S_{FF}}$.

7.2.3 Calibration of TCP FRF

The FRF estimated in the previous sections were based on input forces at the tool-tip (TCP) and the vibrations response at the spindle housing. However, the transfer function $\mathbf{H}(s)$ in Eq. 7.5 maps the forces at the tool-tip to the vibration response at the tool-tip as well. Considering that the flexible modes of the robot are mainly

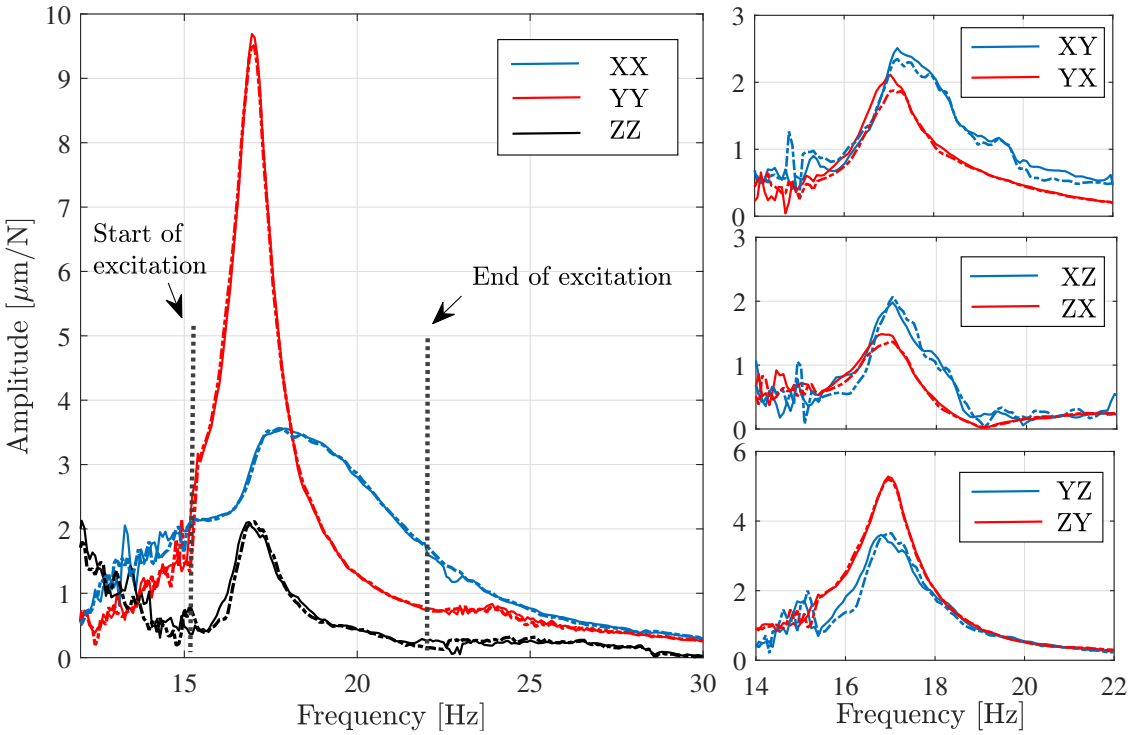

Figure 7.11: Measured in-process FRF using speed sweep tests. Solid lines: first series, Dashed lines: second series.

associated with the flexibility of the robot's joints, it can be assumed that the vibration of the spindle-holder-tool assembly at these modes is a rigid-body motion. With this assumption, we can multiply the resulting in-process FRF by a constant coefficient to calibrate them to represent the TCP FRF. Fig. 7.12(a) illustrates the rigid body motion of the assembly. It is assumed that the joints of the robot have small rotational displacements. Due to the joints' displacement, the rigid body motion of the assembly includes translational and rotational displacements. As a result, the absolute displacements at the tool-tip and sensor locations are different. With reference to Fig. 7.12, the calibration coefficient for the FRF in the vicinity of each mode is determined as follows:

1. The two FRF H_{ST} and H_{TT} are measured by applying hammer impulse at the tool-tip (point T) and measuring the response at the sensor's location (point S) and tool-tip, respectively (Fig. 7.12(a)).

2. Modal fitting is applied to the measured FRF, H_{ST} and H_{TT}, to find the corre-

sponding mode shape between points S and T (Fig. 7.12(c)):

$$H_{pq}(\omega) = \frac{\phi_p \phi_q}{\omega_n^2 - \omega^2 + i2\xi\omega\omega_n} \quad \text{for} \quad p, q = S, T \tag{7.13}$$

3. The FRF H_{ST} is calibrated by the mode shape ratio such that the calibrated H_{ST} matches H_{TT}, and as a result, the total displacement of the two points is equal (Fig. 7.12(d)):

$$H_{TT}(\omega) \simeq H_{ST}^{calibrated}(\omega) = \frac{\phi_T}{\phi_S} H_{ST}(\omega) \tag{7.14}$$

The same coefficient, $\frac{\phi_T}{\phi_S}$, is used to calibrate the in-process FRF obtained in the previous sections. The calibrated in-process FRF are used in frequency and discrete-time chatter analysis methods to develop the robot's stability lobe diagrams in the next section.

7.3 Stability Lobe Diagrams with In-Process FRF

Acetal Copolymer workpiece was milled with an end mill that has diameter of 12.7 mm and two cutting teeth with $\gamma = \pi/2$. The cutting force coefficients were determined experimentally at $K_{tc} = 119$ MPa and $k_{rc} = 0.17$ and $k_{ac} = 0.33$ [83]. Stability of vibrations during machining is determined by monitoring the cutting forces and the spindle vibrations. Both types of Hopf and period-doubling bifurcations are checked in each test. Hopf bifurcation was identified according to the Fast Fourier Transformation (FFT) of the cutting forces and spindle vibrations, and period-doubling was identified according to the time-history of the measured signals.

At each tested spindle speed, the cutting depth was increased incrementally until a dominating peak that is not a harmonic of spindle rotation frequency was observed in the signals' FFT. This cutting depth was then determined as the border of Hopf bifurcation at the tested spindle speed. An example of Hopf bifurcation detection is shown in Fig. 7.13. The measured force and vibration signals in feed direction and their frequency spectra at axial cutting depths of 1.5 and 2 mm are shown in Fig.7.13. The displacement was obtained by numerically integrating the measured accelerations. At 1.5 mm depth, the FFT plots show peaks at the harmonics of spindle and tooth passing frequencies, i.e. $f_t/2$ and f_t, respectively. However, at 2 mm depth,

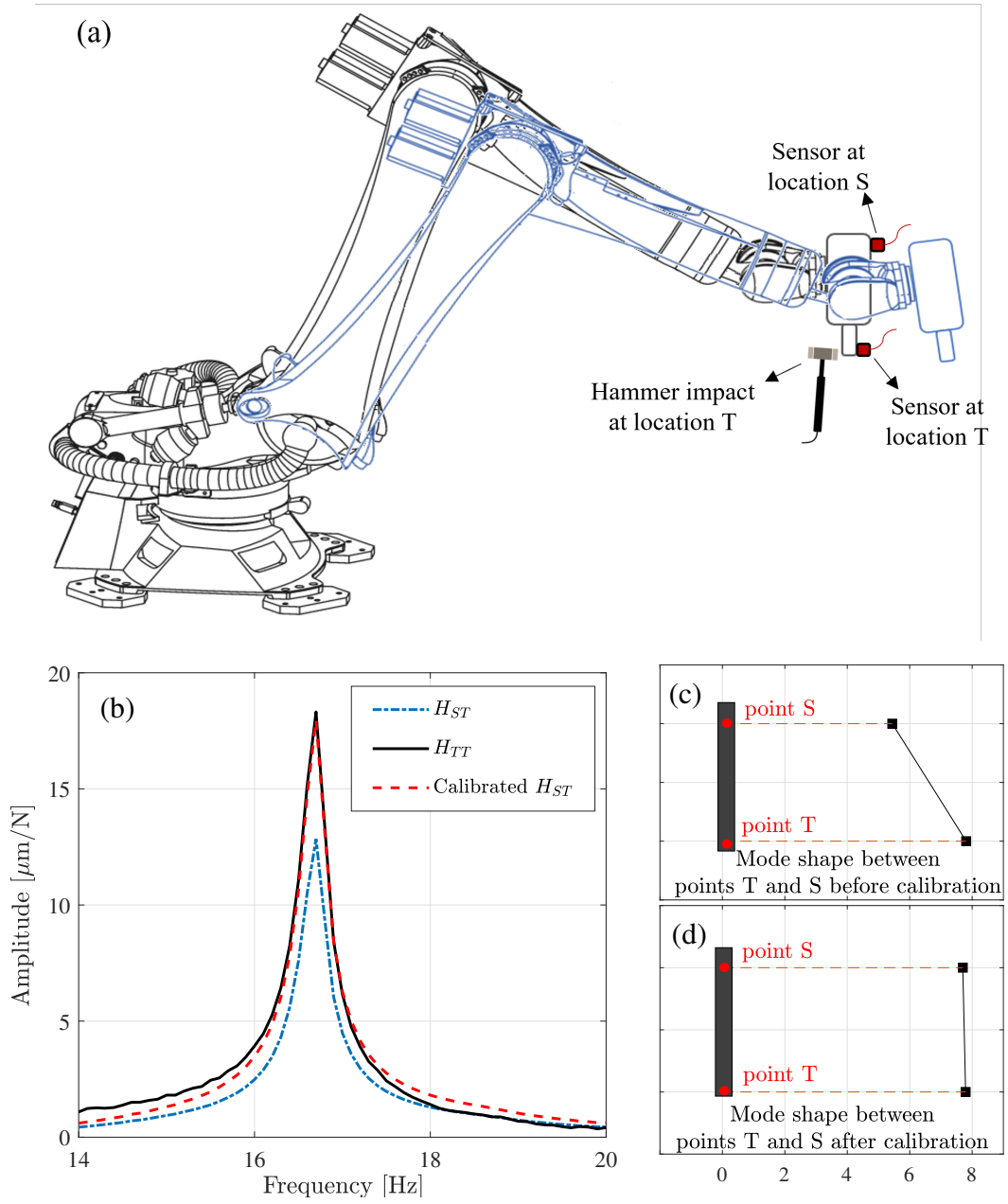

Figure 7.12: Calibration of identified in-process FRF. (a) illustration of the rigid body motion of the spindle-holder-tool assembly due to rotational displacements at the joints, (b) measured and calibrated FRFs, (c) mode-shape before calibration and (d) after calibration.

the amplitude of force and vibration signals grow and the FFT plots (specially the FFT of vibrations) show a dominant peak at the chatter frequency $f_c \approx 18$ Hz. This point is identified as chatter emanating from Hopf bifurcation. Stable and unstable

cuts were primarily distinguished by their corresponding vibration and force signals measured by accelerometers and the dynamometer, respectively. Nonetheless, the machined surface was also inspected visually for further confirmation of vibration stability/instability. Figure 7.14 shows examples of the surfaces machined under stable and unstable conditions. Cases (a) and (b) correspond to stable conditions as only feed marks are observed on the surface. When the system is unstable, the feed marks are distorted by unstable vibrations as shown in cases (c) and (d).

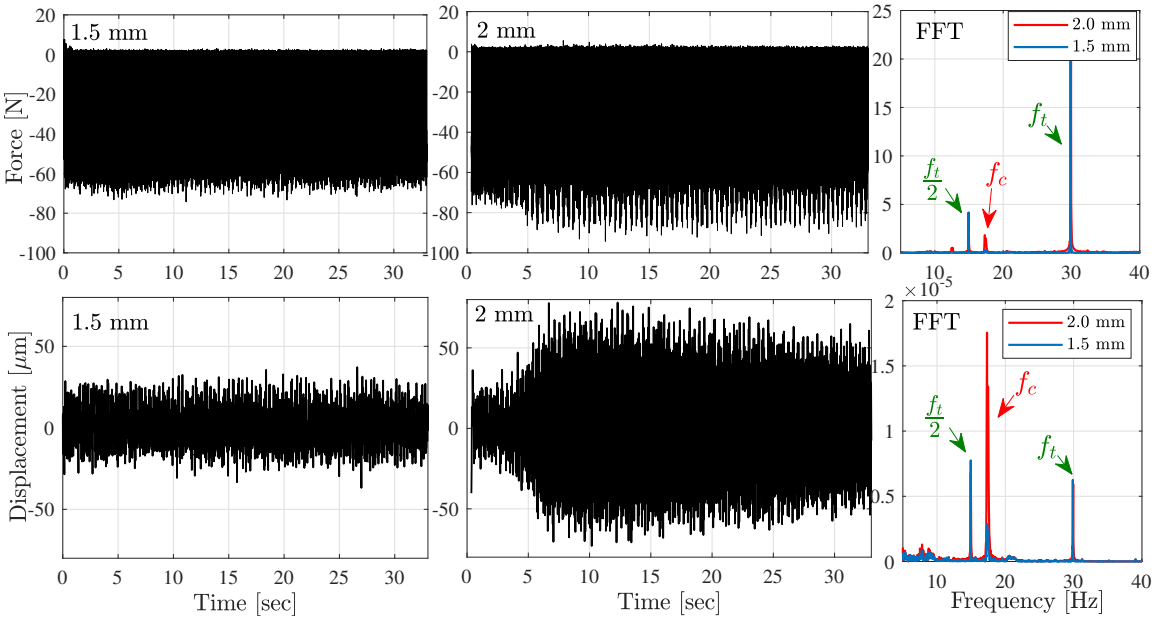

Figure 7.13: Detection of Hopf bifurcations using measured force and vibrations signals (in feed direction). Half-immersion down-milling at spindle speed of 900 rev/min and feedrate of 0.15 mm/tooth.

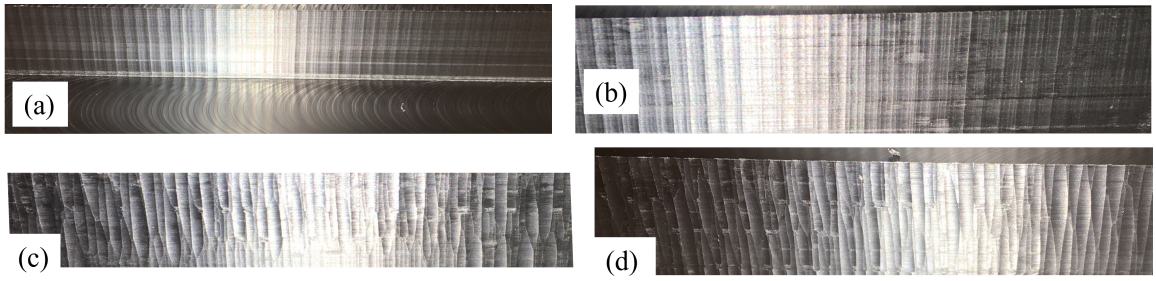

Figure 7.14: Cutting surfaces of Acetal Copolymer workpiece. (a) stable, 800 rev/min, 1.5 mm. (b) stable, 1200 rev/min, 2 mm. (c) unstable, 800 rev/min, 2 mm. (d) unstable, 900 rev/min, 2.5 mm.

For period doubling bifurcations, the time history of displacement is observed.

Figure 7.15 shows samples of chatter as a result of period doubling bifurcation compared to Hopf bifurcation. The orange dots are the same signal sampled at tooth passing frequency. At 1100 rev/min spindle speed, the system is stable at 0.5 mm depth, but at 2.5 mm depth, the sampled signals forms two parallel branches indicating period doubling [120]. Note that the two branches are expected to be straight in the time history of the signals. However, the branches are not straight during the cut. This could be due to i) small variations in spindle speed during operation, and ii) small variations in natural frequency as the robot's posture changes during the cut. Periodic oscillations emanating from period-doubling bifurcation were observed until 4 mm depth of cut, at which point they loose stability. On the contrary, at 1200 rev/min the system goes through Hopf bifurcation without observing any period doubling bifurcations.

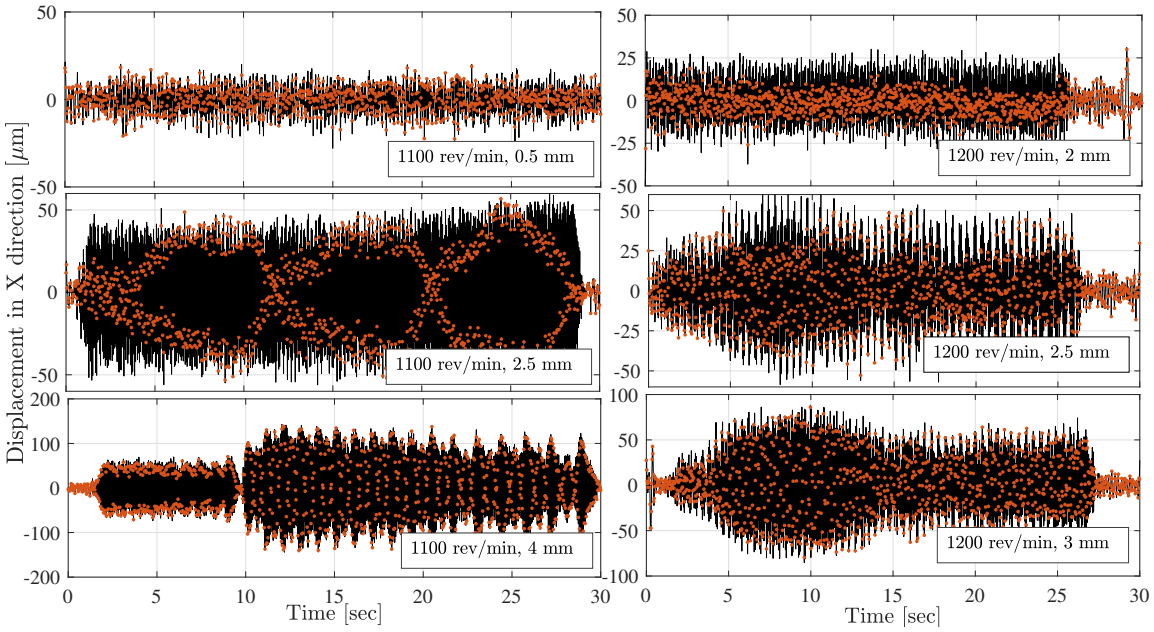

Figure 7.15: Displacements at the spindle speeds 1100 rev/min and 1200 rev/min. Orange dots represents sampled signals at the tooth passing frequency.

Similar chatter tests are conducted at several speeds and axial depth of cut values and the summary of results is shown in Fig. 7.16. The circles and crosses stand for stable and chatter due to Hopf bifurcation, respectively. The square signs shows chatter due to period doubling bifurcation. In Fig. 7.16, the stability diagrams calculated based on Nyquist criteria using idle (hammer test) FRF and in-process FRF are also shown. The experimental results agree with SLD obtained from in-process

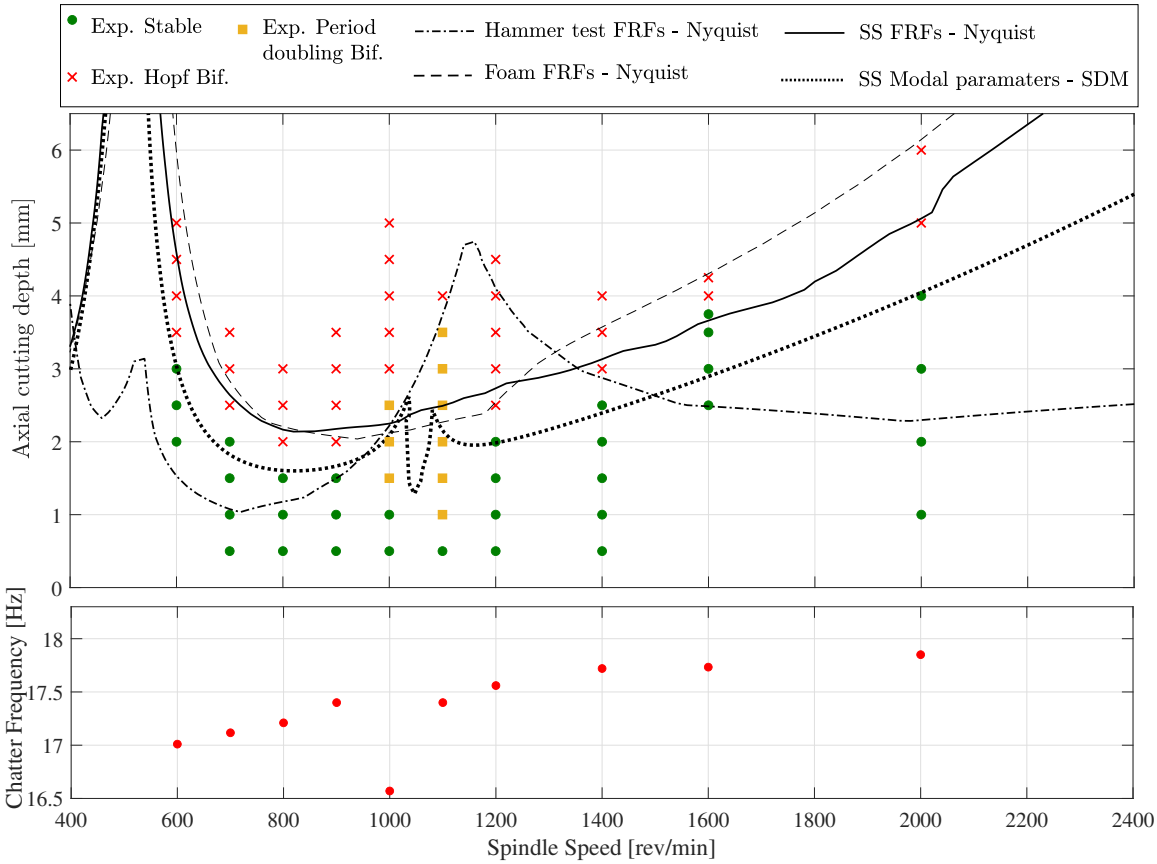

Figure 7.16: Stability diagram of half-immersion down-milling of Acetal workpiece using a tool with 12.7 mm diameter and two teeth. The abbreviation SS stands for speed sweep tests.

FRF but there are considerable discrepancies between them and the SLD developed by hammer test FRF. The rightmost lobe in the SLD associated with hammer FRF show the Hopf bifurcation limit of the mode at 20 Hz, which is lightly damped in the hammer test FRF but heavily damped in the in-process FRF. The experimental results clearly show that this mode is indeed stable during the process and it does not cause chatter. The force and acceleration signals (in normal direction) measured under 1600 and 2000 rev/min are presented in Figs. 7.17 and 7.18, respectively. The SLD with idle FRF suggests that, at these spindle speeds, the system is unstable at cutting depth of 3 mm. However, the measured signals indicate that chatter occurs at a higher cutting depth. The FFTs of vibration signals at 1600 and 2000 rev/min are also presented in Fig. 7.19. Chatter and tooth passing frequencies are shown as f_c and f_t, respectively. In both cases, it can be seen that the chatter frequencies are

between 17.5-18 Hz which correspond to the mode in normal direction (Y). There is no peak in the vicinity of 20 Hz, confirming that this mode is mostly damped and does not cause chatter.

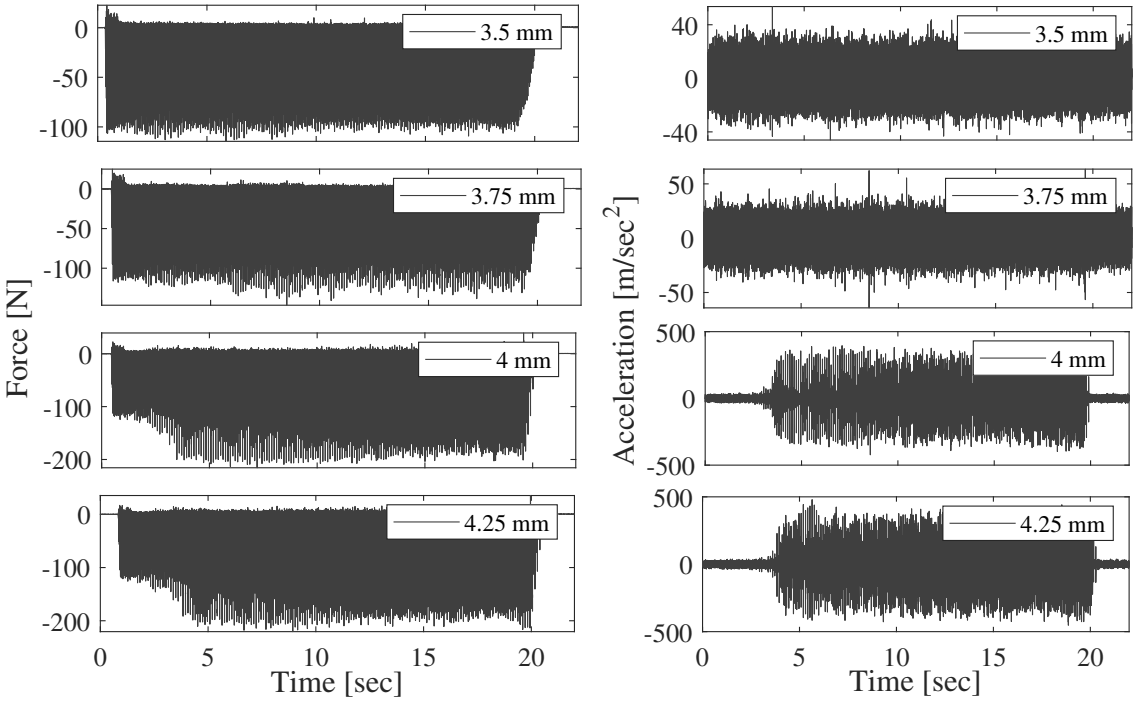

Figure 7.17: Measured cutting force and acceleration in normal direction at spindle speed of 1600 rev/min.

As shown in Fig. 7.16, period doubling bifurcations are not predicted by the ZOA method and Nyquist criterion, because the average values of directional coefficients are used. Semi-discretization Method (SDM) considers the periodicity of the directional coefficients and therefore is able to predict period-doubling bifurcation, however SDM requires modal fitting of the measured FRF. Considering non-proportional damping in the system, the modal decomposition of the FRF is expressed as follows [121]:

$$H_{pq}(\omega) = \sum_{r=1}^{n} \left(\frac{\Psi_{pr}^{\mathrm{R}} \Psi_{qr}^{\mathrm{L}}}{i\omega - \lambda_r} + \frac{\bar{\Psi}_{pr}^{\mathrm{R}} \bar{\Psi}_{qr}^{\mathrm{L}}}{i\omega - \bar{\lambda}_r} \right) , \ \lambda_r = -\omega_{\mathrm{n},r}\zeta_r \pm i\omega_{\mathrm{n},r}\sqrt{1-\zeta_r^2} \tag{7.15}$$

where ω_n is the natural frequency, ζ_r is the damping ratio, Ψ^{R} is the normalized right eigenvector, and Ψ^{L} is the normalized left eigenvector and n is the number of modes. The procedure in [54] was followed to identify these modal parameters

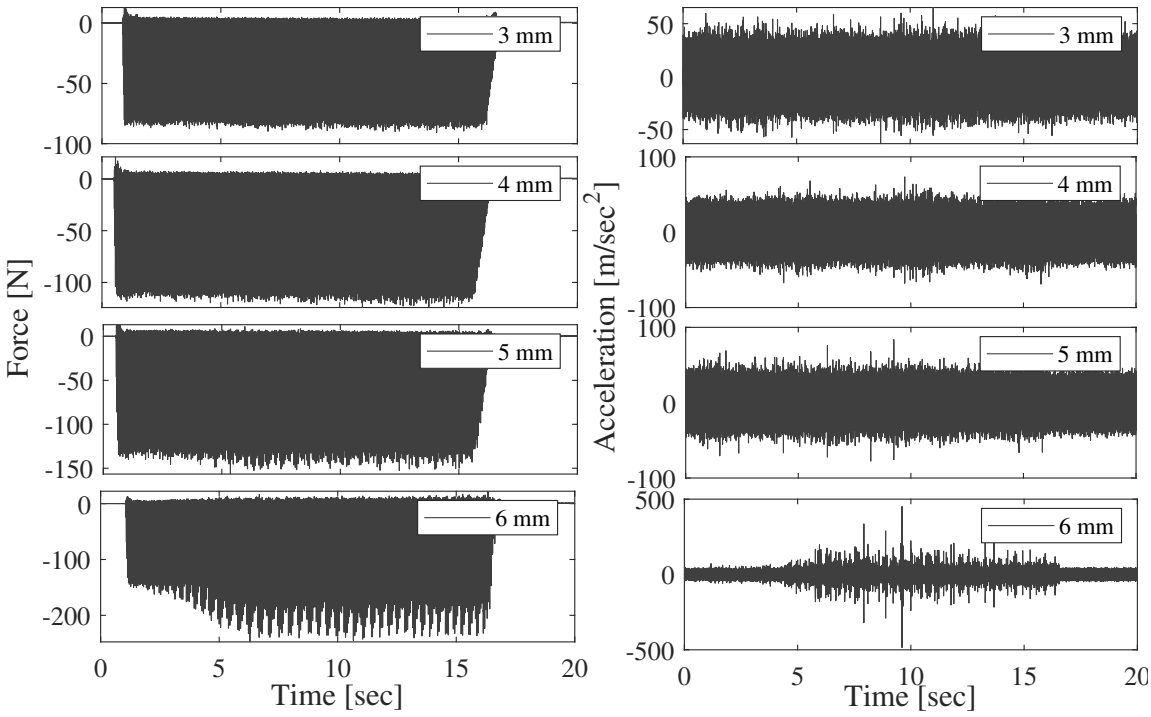

Figure 7.18: Measured cutting force and acceleration in normal direction at spindle speed of 2000 rev/min.

from in-process FRF. The fitting procedure was applied to the FRF measured in speed sweep tests. Two flexible modes were assumed to be present in the frequency range of interest. The identified parameters of these mode are presented in Table 7.1. Figure 7.20 shows the fitted FRF, calculated using the identified modal parameters in Table 7.1, and compares them against the measured FRF.

Table 7.1: Identified modal parameters of the system flexible modes.

Mode	f_n (Hz)	$\zeta_n(\%)$	$\Psi^L(\times 10^4)$	$\Psi^R(\times 10^4)$
			-18.34-5.34i	-20.57-7.18i
1	16.99	2.85	-51.47+48.61i	-39.21+55.05i
			-17.10+16.37i	-13.93+14.31i
			32.31-76.26i	50.46-17.77i
2	18.48	9.96	-28.53+3.08i	-23.99-13.26i
			-5.08+6.72i	-2.78+ 6.96i

The modal parameters shown in Table 7.1 are used in SDM method [54, 33] to predict the SLD shown by the dotted line in Fig. 7.16. Except around 1100 rev/min, the SLD agrees with the ones obtained from ZOA and Nyquist method with in-

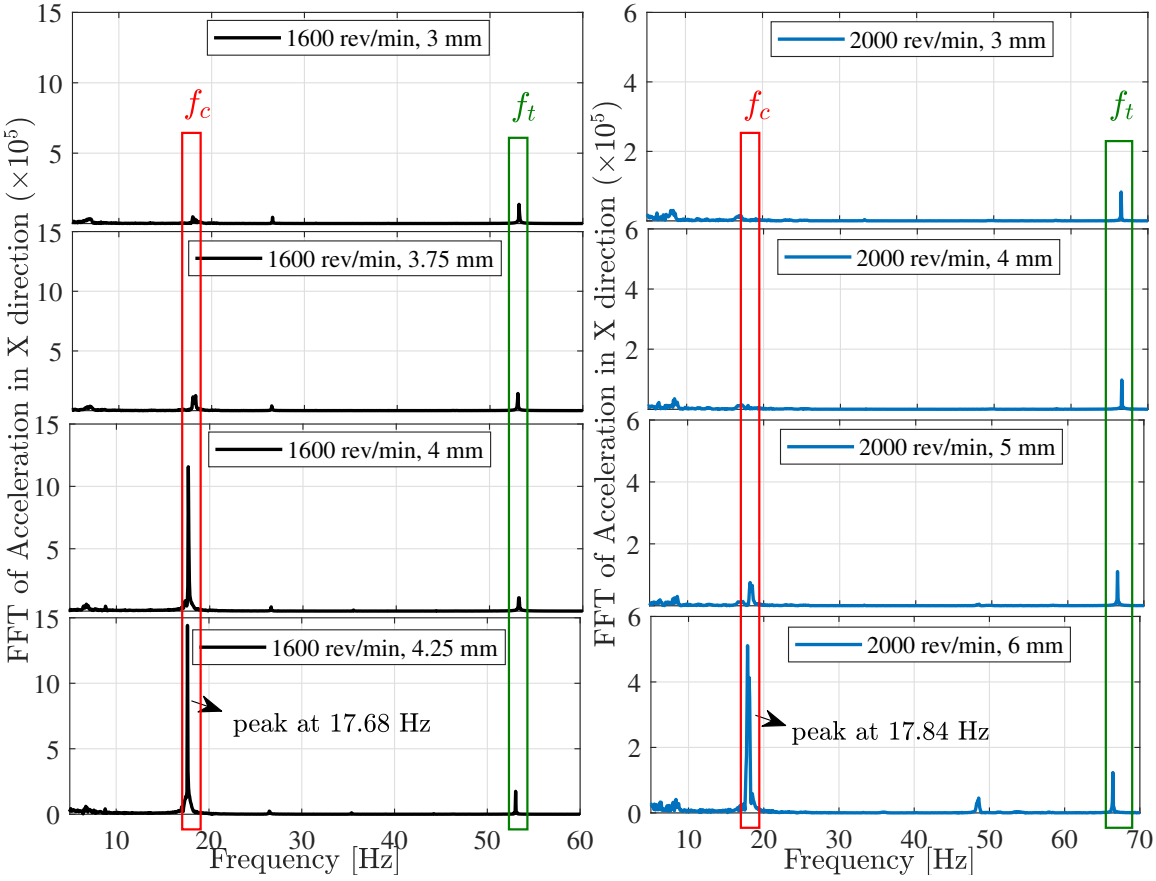

Figure 7.19: FFT of vibrations signal in chatter tests at 1600 and 2000 rev/min.

process FRF. The notch close to 1100 rev/min in the SLD from SDM is the period-doubling bifurcations limit, which is not predicted by the ZOA method. Consistent with the SLD from SDM, period doubling was observed around 1100 rev/min in the experiments, although the experimental results suggest a wider region of period doubling bifurcation.

Overall, compared to idle FRF, the stability diagrams associated with the in-process FRF agree better with the experimental results. The discrepancies between the experimental results and the SLD are mainly because of the different cutting speed and depth values that were used in FRF estimation and chatter tests. The FRF were measured under fixed spindle speed and cutting depth, but those values are different at each one of the tested points shown in Fig.7.16.

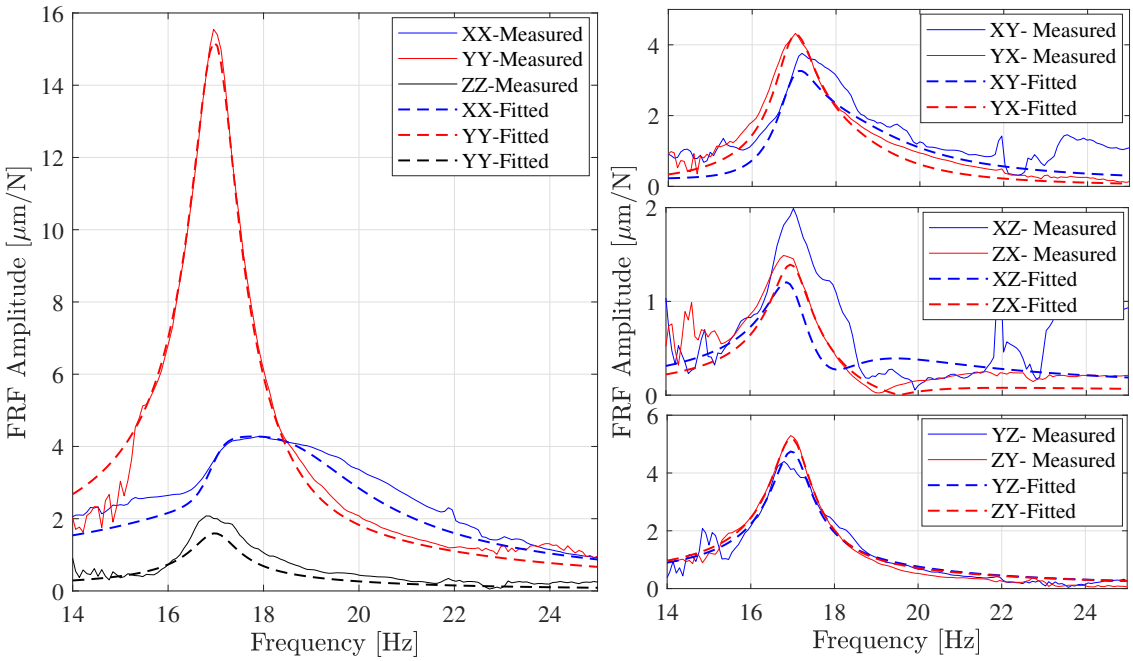

Figure 7.20: Amplitude of fitted and measured FRF in the speed sweep tests (FRF are calibrated to represent the dynamics at the tool tip).

7.4 Conclusions

Two new methods were presented for in-process measurement of TCP FRF in machining robots. The presented methods leverage the machining forces as the input to the system and estimate the FRF from the force and vibrations measured during the process. The application of porous materials to randomize the machining forces and spindle speed sweep technique are shown to be effective in achieving broadband and uncorrelated excitation. The measured in-process FRF yield more accurate predictions of chatter-free machining parameters than the FRF measured by impulse hammer test when the robot is idle.

When a table dynamometer was used to measure the input (machining) forces, this method can only measure the FRF in the posture that positions the TCP at the dynamometer. Nonetheless, if the machining robot is equipped with a wrist force sensors or a rotary dynamometer, the presented method can be applied in arbitrary postures as well.

Chapter 8

Conclusion

This thesis focused on the fundamental differences between the structural dynamics of robotic and CNC machining systems. The distinct characteristics of structural dynamics of robotic machining systems are i) pose-dependency, ii) high axial flexibility, and iii) nonlinearities. Posture dependency of robot dynamics is a well-investigated topic in literature and comprehensive models are available. The last two features, however, are less-studied which were the primary focus of this thesis. The effects of high axial flexibility and nonlinearities on chatter vibrations were studied. The main contributions and recommendations for future work are presented in the following.

8.1 Contributions

1. *Effect of axial vibrations on cutting forces in robotic milling*

   Although flexibility in axial direction was included in the chatter model in literature, its effect on the modulation of axial cutting depth was ignored. To address this gap, in the first chapter of the thesis, a three-dimensional force model was developed considering the modulation of axial cutting depth with vibrations in the same direction. The new model introduced feed and edge components to the dynamic cutting forces, as well as nonlinear terms. The effects of these additional components in the cutting forces on chatter stability were studied using the ZOA method. Although the effects of nonlinear forces on chatter could be ignored, the feed and edge forces considerably altered the corresponding SLD, especially at high feedrates.

   The results of this study were published in [122].

2. *Detection of nonlinearity in structural dynamics of robotic milling system*

   The existing vibration models of robotic milling in the literature assume linear structural dynamics. The validity of this assumption was investigated in this thesis by examining the compliance of the dynamic response with linearity principles. The first-order frequency response functions of the robot under different excitation conditions were measured and it was found that the measured first-order FRF are not unique. The results of experimental modal analysis and nonlinear complex mode analysis revealed a systematic change in the receptance of the system with the level of harmonic excitation force, indicating violation of the linearity assumption. By developing SLD, it was shown that the variation of FRF at higher excitation force amplitudes changes the stability limit considerably. The amplitude of the harmonic excitation forces was at the level of milling forces, meaning that the milling forces can effectively excite the nonlinearities in the structural dynamics of robots during the process.

   The results of this study were published in [123].

3. *Modeling of structural nonlinearities*

   A comprehensive experimental procedure was developed to model and identify the structural nonlinearity of robotic machining systems. Firstly, the nonlinear restoring forces of the structure and their variation with dynamic displacement and velocity of the robot TCP were experimentally determined to classify the type of nonlinearity. Results showed that hardening and softening are the governing nonlinear effects and can be characterized by cubic stiffness and damping models.

   Subsequently, the higher-order frequency response functions of the system were estimated from measurements with step-wise harmonic excitations; the parameters of the nonlinear model of stiffness and damping were identified by applying least-square curve-fitting on the estimated higher-order frequency response functions. The accuracy of the developed nonlinear model in capturing the nonlinear behavior of the system in the vicinity of well-separated modes was verified experimentally.

   The modeling and identification approach was applied to a machining robot with revolute joints, however, it can be used for robots with different configurations and applications as well.

The results of this study were published in [10].

4. *Bifucation analysis of vibrations in nonlinear robotic milling system*

   The developed nonlinear model of structural dynamics was combined with the cutting force model to derive the equations of motion. The system was described by a set of non-autonomous nonlinear delayed differential equations with periodic coefficients and non-smooth terms. The non-smoothness was introduced to the equations because of considering the intermittent engagement of the tool with the workpiece and loss of contact at high amplitude vibrations. Bifurcation of the forced periodic oscillations of the milling system was studied using the numerical continuation method. For this purpose, smoothing techniques were applied and the periodic coefficients were estimated by an appended oscillator described by an autonomous differential equation.

   Both secondary Hopf and period-doubling bifurcations of the periodic oscillations were identified. The effect of nonlinear parameters on the bifurcation diagrams was studied. It was also shown that, unlike linear milling systems, the feedrate can affect the stability limits in nonlinear milling systems. Since feedrate directly influences the amplitude of forced oscillations, the nonlinear system's damping and stiffness and consequently its chatter stability change by feedrate.

   The results of this study were published in [124].

5. *Measurement of in-process frequency response functions in robotic milling and employing them in chatter stability analysis*

   A different approach was applied to consider the effect of structural nonlinearities on chatter stability while using linear models. This way, the complexity of nonlinear modeling and bifurcation analysis is avoided. In this approach, the frequency response functions are measured during the milling process. Therefore, they represent the nonlinear dynamics linearized about the applied operational conditions. The in-process FRF include not only the nonlinear stiffness and damping effects, but also the effects of feed motion. Two methods of in-process FRF measurement were proposed: i) milling of porous material, ii) speed varying milling of homogenous material. Both methods can be used for identification of the FRF of the MIMO system, i.e. the cross-coupling between FRF can be considered.

The measured in-process FRF were employed in linear frequency and time domain chatter analysis methods to predict SLD. Compared to SLD using idle FRF (FRF that are measured at the idle state of the robot), the SLD using in-process FRF agreed better with the experimental chatter test results.

The results of this study were published in [125].

8.2 Future work

The following ideas can be followed for future research studies:

- *Multi-mode modeling of structural nonlinearities*

  The developed single degree of freedom model in this thesis could accurately predict the dynamic response of well-separated vibrations modes. However, lower accuracy of the model predictions was observed for closely-spaced modes. Multi degrees of freedom models considering the nonlinear coupling between vibration modes need to be considered to accurately predict the system's nonlinear behavior in the vicinity of all vibration modes.

- *Integration of nonlinear model of the joints' flexibility with MBD model*

  The modeling approach presented in this thesis is suitable for milling with a limited workspace, in which the variation of the robot's posture is negligible. It is known that the structural flexibility of robots, including the nonlinear effects, is associated with the joints' flexibility. Therefore, to be able to predict the dynamic response at any given posture, the nonlinear behavior of each joint should be modeled and identified separately, and then integrated with the MBD model of the robot.

- *Other approaches for in-process measurement of FRF*

  The in-process FRF identification methods introduced in this thesis require measurement of the input, i.e. cutting forces. This can be done by table (for fixed posture) or rotary (for variable posture) dynamometers. Other approaches such as operational modal analysis, inverse stability or machine learning-based methods can be used for which only the measurement of output is required.

- *Effect of feedrate in linear chatter model*

It was shown that the value of feedrate can change the chatter stability of the robotic milling process in two ways: i) the effect on feed-dependent components of dynamic cutting forces, ii) the effect on nonlinear stiffness and damping of the joints. During the in-process FRF measurements and chatter tests, in the last chapter of this thesis, the same value of feedrate was used. It would be valuable to model the effect of feedrate values and integrate it with the linear model of chatter stability.

- *Study of uncertainties in nonlinear robotic milling*

  Several sources of uncertainties in the mechanics and dynamics of the machining process are presented throughout the real operations that affect the stability of the vibration. Although an elementary sensitivity analysis for the parameters of the nonlinear terms in structural dynamics was presented in Chapter 6, an investigation into a robust model of robotic milling and probability distributions to develop credibility bounds around the stability lobe diagrams is a subject for future study.

Bibliography

[1] Hw machine tools co. ltd. http://hwmachine.ie/mazak-3, Accessed 25 May 2022.

[2] Bg robots. http://bgrobots.com, Accessed 25 May 2022.

[3] Dalian sansheng precision machinery co. ltd. https://www.sansmachining.com, Accessed 25 May 2022.

[4] Imeche (institution of mechanical engineers). https://www.imeche.org/news/news-article/feature-robots-take-on-more-aerospace-tasks-thanks-to-accuracy-boost, Accessed 25 May 2022.

[5] Stäubli international ag. https://www.staubli.com/cn/en/robotics/industries/metal/metal-processing/robot-assisted-machining-of-molds.html, Accessed 25 May 2022.

[6] Vogel communications group. https://www.maschinenmarkt.international/oversized-plastic-pipes-milled-to-perfection-gal-569061/?p=1, Accessed 25 May 2022.

[7] Empowering technologies. https://empowering-technologies.com/composite-manufacturing/robotic-sanding/automated-solution, Accessed 25 May 2022.

[8] Hoai Nam Huynh, Hamed Assadi, Edouard Rivière-Lorphèvre, Olivier Verlinden, and Keivan Ahmadi. Modelling the dynamics of industrial robots for milling operations. *Robotics and Computer-Integrated Manufacturing*, 61:101852, 2020.

[9] J Tlusty and F Ismail. Basic non-linearity in machining chatter. *CIRP Annals*, 30(1):299–304, 1981.

[10] Yaser Mohammadi and Keivan Ahmadi. Single degree-of-freedom modeling of the nonlinear vibration response of a machining robot. *Journal of Manufacturing Science and Engineering*, 143(5), 2020.

[11] I Iglesias, MA Sebastián, and JE Ares. Overview of the state of robotic machining: Current situation and future potential. *Procedia engineering*, 132:911–917, 2015.

[12] Christian Lehmann, Marcello Pellicciari, Manuel Drust, and Jan Willem Gunnink. Machining with industrial robots: the comet project approach. In *International Workshop on Robotics in Smart Manufacturing*, pages 27–36. Springer, 2013.

[13] EU COMET. Fp7-project: Plug-and-produce components and methods for adaptive control of industrial robots enabling cost effective, high precision manufacturing in factories of the future (http://www.cometproject.eu). 2011.

[14] Yonghua Chen and Fenghua Dong. Robot machining: recent development and future research issues. *The International Journal of Advanced Manufacturing Technology*, 66(9):1489–1497, 2013.

[15] Alexander Verl, Anna Valente, Shreyes Melkote, Christian Brecher, Erdem Ozturk, and Lutfi Taner Tunc. Robots in machining. *CIRP Annals*, 68(2):799–822, 2019.

[16] Mesanori Kunieda and Takeo Nakagawa. Robot-polishing of curved surface with magneto-pressed tool and magnetic force sensor. In *Proceedings of the Twenty-Fifth International Machine Tool Design and Research Conference*, pages 193–200. Springer, 1985.

[17] X Ren, B Kuhlenkötter, and H Müller. Simulation and verification of belt grinding with industrial robots. *International journal of machine tools and manufacture*, 46(7-8):708–716, 2006.

[18] J Norberto Pires, John Ramming, Stephen Rauch, and Ricardo Araújo. Force/torque sensing applied to industrial robotic deburring. *Sensor Review*, 22(3):232–241, 2002.

[19] Alexander Verl, Anna Valente, Shreyes Melkote, Christian Brecher, Erdem Ozturk, and Lutfi Taner Tunc. Robots in machining. *CIRP Annals*, 68:799–822, 2019.

[20] Y Altintas and M Weck. Chatter stability of metal cutting and grinding. *CIRP annals*, 53(2):619–642, 2004.

[21] Jiri Tlusty. *Manufacturing processes and equipment*. Pearson, 2000.

[22] Yusuf Altintas and AA Ber. Manufacturing automation: metal cutting mechanics, machine tool vibrations, and cnc design. *Appl. Mech. Rev.*, 54(5):B84–B84, 2001.

[23] Stephen Albert Tobias. *Machine-tool vibration*. J. Wiley, 1965.

[24] Jiri Tlusty. The stability of machine tools against self-excited vibrations in machining. *International research in production engineering*, 1963.

[25] HE Merrit. Theory of self-excited machine-tool chatter. *Trans. ASME, J. Eng. Ind.*, 87(4):447, 1965.

[26] F Koenisberger and J Tlusty. Machine tool structures-vol. i: Stability against chatter. *Per-gamon Press, Englewood Cliffs, NJ*, 1967.

[27] H Opitz. Chatter behaviour of heavy machine tools, quarterly technical report no 2 af 61 (052)-916. *Research and Technology Division, Wright-Patterson Air Force Base, Ohio*, 1968.

[28] H Opitz. Investigation and calculation of the chatter behavior of: Lathes and milling machines. *Annals of the CIRP*, 18:335–342, 1979.

[29] R Sridhar, RE Hohn, and GW Long. A stability algorithm for the general milling process: contribution to machine tool chatter research—7. 1968.

[30] Ioannis Minis, Rafael Yanushevsky, Abel Tembo, and Robert Hocken. Analysis of linear and nonlinear chatter in milling. *CIRP annals*, 39(1):459–462, 1990.

[31] I Minis and R Yanushevsky. A new theoretical approach for the prediction of machine tool chatter in milling. *Journal of Engineering for Industry*, 115:1, 1993.

[32] Erhan Budak and Yusuf Altintas. Analytical prediction of chatter stability in milling—part i: general formulation. *Journal of dynamic systems, measurement, and control*, 120(1):22–30, 1998.

[33] Tamás Insperger and Gábor Stépán. Semi-discretization method for delayed systems. *International Journal for numerical methods in engineering*, 55(5):503–518, 2002.

[34] Ye Ding, LiMin Zhu, XiaoJian Zhang, and Han Ding. A full-discretization method for prediction of milling stability. *International Journal of Machine Tools and Manufacture*, 50(5):502–509, 2010.

[35] Seifeddine Mejri, Vincent Gagnol, Thien-Phu Le, Laurent Sabourin, Pascal Ray, and Patrick Paultre. Dynamic characterization of machining robot and stability analysis. *The International Journal of Advanced Manufacturing Technology*, 82(1-4):351–359, 2016.

[36] Lutfi Taner Tunca and Omer Faruk Sapmaza. Challenges for industrial robots towards milling applications. *Dynamics*, 2:4, 2017.

[37] Ulrich Schneider, Matteo Ansaloni, Manuel Drust, Francesco Leali, and Alexander Verl. Experimental investigation of sources of error in robot machining. In *International Workshop on Robotics in Smart Manufacturing*, pages 14–26. Springer, 2013.

[38] J Kenneth Salisbury. Active stiffness control of a manipulator in cartesian coordinates. In *Decision and Control including the Symposium on Adaptive Processes, 1980 19th IEEE Conference on*, volume 19, pages 95–100. IEEE, 1980.

[39] Shih-Feng Chen and Imin Kao. Conservative congruence transformation for joint and cartesian stiffness matrices of robotic hands and fingers. *The International Journal of Robotics Research*, 19(9):835–847, 2000.

[40] E Abele, M Weigold, and S Rothenbücher. Modeling and identification of an industrial robot for machining applications. *CIRP Annals-Manufacturing Technology*, 56(1):387–390, 2007.

[41] E Abele, J Baer, and M Pischan. Prediction of the tool displacement for robot milling applications using coupled models of an industrial robot and removal simulation. In *Proc. CIRP 2nd Inter Conf on Process Machine Interactions, Vancouver, Canada*, 2010.

[42] Claire Dumas, Stéphane Caro, Sébastien Garnier, and Benoît Furet. Joint stiffness identification of six-revolute industrial serial robots. *Robotics and Computer-Integrated Manufacturing*, 27(4):881–888, 2011.

[43] Mark W Spong. Modeling and control of elastic joint robots. *Journal of dynamic systems, measurement, and control*, 109(4):310–318, 1987.

[44] Stefano Baglioni, Filippo Cianetti, Claudio Braccesi, and Denis Mattia De Micheli. Multibody modelling of n dof robot arm assigned to milling manufacturing. dynamic analysis and position errors evaluation. *Journal of Mechanical Science and Technology*, 30(1):405–420, 2016.

[45] Hoai Nam Huynh, Edouard Rivière-Lorphèvre, and Olivier Verlinden. Integration of machining simulation within a multibody framework: application to milling. In *IMSD: The 4th Joint International Conference on Multibody System Dynamics*, 2016.

[46] Said Mousavi, Vincent Gagnol, Belhassen C Bouzgarrou, and Pascal Ray. Dynamic modeling and stability prediction in robotic machining. *The International Journal of Advanced Manufacturing Technology*, 88(9):3053–3065, 2017.

[47] Stig Moberg, Erik Wernholt, Sven Hanssen, and Torgny Brogårdh. Modeling and parameter estimation of robot manipulators using extended flexible joint models. *Journal of Dynamic Systems, Measurement, and Control*, 136(3):031005, 2014.

[48] Vinh Nguyen, Toni Cvitanic, and Shreyes Melkote. Data-driven modeling of the modal properties of a six-degrees-of-freedom industrial robot and its application to robotic milling. *Journal of Manufacturing Science and Engineering*, 141(12):121006, 2019.

[49] Maximilian Busch, Florian Schnoes, Thomas Semm, Michael F Zaeh, Birgit Obst, and Dirk Hartmann. Probabilistic information fusion to model the pose-

dependent dynamics of milling robots. *Production Engineering*, 14(4):435–444, 2020.

[50] Vinh Nguyen and Shreyes Melkote. Hybrid statistical modelling of the frequency response function of industrial robots. *Robotics and Computer-Integrated Manufacturing*, 70:102134, 2021.

[51] DJ Ewins. Modal testing: theory, practice and application (mechanical engineering research studies: engineering dynamics series). *Research studies Pre, 2nd ed., ISBN-13*, pages 978–0863802188, 2000.

[52] P Elosegui. Measurement of the dynamic model of a puma 560 robot using experimental modal analysis. *Journal of Mechanical Design*, 116(1):75–79, 1994.

[53] Jing Li, Biao Li, NanYan Shen, Hui Qian, and ZiMeng Guo. Effect of the cutter path and the workpiece clamping position on the stability of the robotic milling system. *The International Journal of Advanced Manufacturing Technology*, 89(9-12):2919–2933, 2017.

[54] Marcel Cordes, Wolfgang Hintze, and Yusuf Altintas. Chatter stability in robotic milling. *Robotics and Computer-Integrated Manufacturing*, 55:11–18, 2019.

[55] C Eksioglu, ZM Kilic, and Y Altintas. Discrete-time prediction of chatter stability, cutting forces, and surface location errors in flexible milling systems. *Journal of Manufacturing Science and Engineering*, 134(6), 2012.

[56] Yun Yang, Wei-Hong Zhang, Ying-Chao Ma, and Min Wan. Chatter prediction for the peripheral milling of thin-walled workpieces with curved surfaces. *International Journal of Machine Tools and Manufacture*, 109:36–48, 2016.

[57] Lutfi Taner Tunc and Jay Shaw. Experimental study on investigation of dynamics of hexapod robot for mobile machining. *The International Journal of Advanced Manufacturing Technology*, 84(5-8):817–830, 2016.

[58] Imed Zaghbani and Victor Songmene. Estimation of machine-tool dynamic parameters during machining operation through operational modal analysis. *International Journal of Machine Tools and Manufacture*, 49(12-13):947–957, 2009.

[59] S Kim and K Ahmadi. Estimation of vibration stability in turning using operational modal analysis. *Mechanical Systems and Signal Processing*, 130:315–332, 2019.

[60] Adam K Kiss, David Hajdu, Daniel Bachrathy, and Gabor Stepan. Operational stability prediction in milling based on impact tests. *Mechanical Systems and Signal Processing*, 103:327–339, 2018.

[61] H Opitz and M Weck. Determination of the transfer function by means of spectral density measurements and its application to the dynamic investigation of machine tools under machining conditions. In *Advances in Machine Tool Design and Research 1969*, pages 349–378. Elsevier, 1970.

[62] IE Minis, EB Magrab, and IO Pandelidis. Improved methods for the prediction of chatter in turning, part 1: determination of structural response parameters. *Journal of Engineering for Industry*, 1990.

[63] Orkun Özşahin, Erhan Budak, and HN Özgüven. Investigating dynamics of machine tool spindles under operational conditions. In *Advanced Materials Research*, volume 223, pages 610–621. Trans Tech Publ, 2011.

[64] Gorka Aguirre, Alexander Iglesias, Jokin Munoa, Asier Astarloa, and Joaquim Ciurana. Real milling force based dynamic parameter extraction method. In *ISMA 2014-International Conference on Noise and Vibration Engineering*, 2014.

[65] Alexander Iglesias, J Munoa, C Ramírez, J Ciurana, and Zoltán Dombóvári. Frf estimation through sweep milling force excitation (smfe). *Procedia CIRP*, 46:504–507, 2016.

[66] Keigo Takasugi, Tetsuya Fukuda, Ryota Kito, Naoki Asakawa, and Yoshitaka Morimoto. Fast swept sine cutting test for cnc lathes. *Journal of Advanced Mechanical Design, Systems, and Manufacturing*, 14(6):JAMDSM0092–JAMDSM0092, 2020.

[67] Orkun Özşahin, Erhan Budak, and H Nevzat Özgüven. In-process tool point frf identification under operational conditions using inverse stability solution. *International Journal of Machine Tools and Manufacture*, 89:64–73, 2015.

[68] N Grossi, L Sallese, A Scippa, and G Campatelli. Improved experimental-analytical approach to compute speed-varying tool-tip frf. *Precision Engineering*, 48:114–122, 2017.

[69] Martin Postel, Bircan Bugdayci, Fredy Kuster, and Konrad Wegener. Neural network supported inverse parameter identification for stability predictions in milling. *CIRP Journal of Manufacturing Science and Technology*, 29:71–87, 2020.

[70] Nenad M Kircanski and Andrew A Goldenberg. An experimental study of nonlinear stiffness, hysteresis, and friction effects in robot joints with harmonic drives and torque sensors. *The International Journal of Robotics Research*, 16(2):214–239, 1997.

[71] Michael Ruderman, Frank Hoffmann, and Torsten Bertram. Modeling and identification of elastic robot joints with hysteresis and backlash. *IEEE Transactions on Industrial Electronics*, 56(10):3840–3847, 2009.

[72] Irina Trendafilova and Hendrik Van Brussel. Non-linear dynamics tools for the motion analysis and condition monitoring of robot joints. *Mechanical Systems and Signal Processing*, 15(6):1141–1164, 2001.

[73] Marcel Cordes and Wolfgang Hintze. Offline simulation of path deviation due to joint compliance and hysteresis for robot machining. *The International Journal of Advanced Manufacturing Technology*, 90(1-4):1075–1083, 2017.

[74] Lutfi Taner Tunc and Bora Gonul. Effect of quasi-static motion on the dynamics and stability of robotic milling. *CIRP Annals*, 2021.

[75] Alessandro Gasparetto. A system theory approach to mode coupling chatter in machining. *Journal of dynamic systems, measurement, and control*, 1998.

[76] Guillem Quintana and Joaquim Ciurana. Chatter in machining processes: A review. *International Journal of Machine Tools and Manufacture*, 51(5):363–376, 2011.

[77] Lei Yuan, Zengxi Pan, Donghong Ding, Shuai Sun, and Weihua MCPS Li. A review on chatter in robotic machining process regarding both regenerative and mode coupling mechanism. *IEEE/ASME Transactions on Mechatronics*, 2018.

[78] J Tlusty and M Polacek. The stability of machine tools against self-excited vibrations in machining. *Proceedings of the ASME International*, 1963.

[79] Jianjun Wang, Hui Zhang, and Zengxi Pan. Machining with flexible manipulators: Critical issues and solutions. In *Industrial Robotics: Programming, Simulation and Applications*. IntechOpen, 2006.

[80] Zengxi Pan, Hui Zhang, Zhenqi Zhu, and Jianjun Wang. Chatter analysis of robotic machining process. *Journal of materials processing technology*, 173(3):301–309, 2006.

[81] Lejun Cen and Shreyes N Melkote. Cct-based mode coupling chatter avoidance in robotic milling. *Journal of Manufacturing Processes*, 29:50–61, 2017.

[82] Ehsan Jafarzadeh and Mohammad R Movahhedy. Numerical simulation of interaction of mode-coupling and regenerative chatter in machining. *Journal of Manufacturing Processes*, 27:252–260, 2017.

[83] Yusuf Altintas. *Manufacturing automation: metal cutting mechanics, machine tool vibrations, and CNC design*. Cambridge university press, 2012.

[84] M Cordes, W Hintze, and Y Altintas. Chatter stability in robotic milling. *Robotics and Computer-Integrated Manufacturing*, 55:11–18, 2019.

[85] Marian Wiercigroch and Erhan Budak. Sources of nonlinearities, chatter generation and suppression in metal cutting. *Philosophical Transactions of the Royal Society of London. Series A: Mathematical, Physical and Engineering Sciences*, 359(1781):663–693, 2001.

[86] Francis C Moon and Tamas Kalmar-Nagy. Nonlinear models for complex dynamics in cutting materials. *Philosophical Transactions of the Royal Society of London A: Mathematical, Physical and Engineering Sciences*, 359(1781):695–711, 2001.

[87] NH Hanna and SA Tobias. A theory of nonlinear regenerative chatter. *Journal of Engineering for Industry*, 1974.

[88] HM Shi and SA Tobias. Theory of finite amplitude machine tool instability. *International Journal of Machine Tool Design and Research*, 24(1):45–69, 1984.

[89] Ali H Nayfeh, Char-Ming Chin, and Jon Pratt. Perturbation methods in nonlinear dynamics—applications to machining dynamics. *Journal of Manufacturing Science and Engineering*, 1997.

[90] MS Fofana. Delay dynamical systems and applications to nonlinear machine-tool chatter. *Chaos, Solitons & Fractals*, 17(4):731–747, 2003.

[91] JS Lin and CI Weng. A nonlinear dynamic model of cutting. *International Journal of Machine Tools and Manufacture*, 30(1):53–64, 1990.

[92] Zoltan Dombovari, David AW Barton, R Eddie Wilson, and Gabor Stepan. On the global dynamics of chatter in the orthogonal cuttingmodel. *International Journal of Non-Linear Mechanics*, 46(1):330–338, 2011.

[93] Naren Deshpande and MS Fofana. Nonlinear regenerative chatter in turning. *Robotics and Computer-Integrated Manufacturing*, 17(1-2):107–112, 2001.

[94] Alfredo Bellen, Nicola Guglielmi, and Marino Zennaro. Numerical stability of nonlinear delay differential equations of neutral type. *Journal of Computational and Applied Mathematics*, 125(1-2):251–263, 2000.

[95] Tamás Kalmár-Nagy, Gábor Stépán, and Francis C Moon. Subcritical hopf bifurcation in the delay equation model for machine tool vibrations. *Nonlinear Dynamics*, 26(2):121–142, 2001.

[96] Andrew Honeycutt and Tony Schmitz. Milling bifurcations for strongly asymmetric, symmetric, and weakly asymmetric system dynamics. *Precision Engineering*, 55:1–13, 2019.

[97] Hamed Moradi, Mohammad R Movahhedy, and Gholamreza Vossoughi. Dynamics of regenerative chatter and internal resonance in milling process with structural and cutting force nonlinearities. *Journal of Sound and Vibration*, 331(16):3844–3865, 2012.

[98] Mahdi Eynian. *Chatter stability of turning and milling with process damping*. PhD thesis, University of British Columbia Vancouver, Canada, 2010.

[99] Bruno Siciliano and Oussama Khatib. Robotics and the handbook. In *Springer Handbook of Robotics*, pages 1–6. Springer, 2016.

[100] Jacob Pieter Den Hartog. *Mechanical vibrations*. Courier Corporation, 1985.

[101] Nuno Manuel Mendes Maia and Júlio Martins Montalvao e Silva. *Theoretical and experimental modal analysis*. Research Studies Press, 1997.

[102] G Gloth and M Sinapius. Analysis of swept-sine runs during modal identification. *Mechanical systems and signal processing*, 18(6):1421–1441, 2004.

[103] Julius S Bendat and Allan G Piersol. Engineering applications of correlation and spectral analysis. *New York, Wiley-Interscience, 1980. 315 p.*, 1980.

[104] Keith Worden. *Nonlinearity in structural dynamics: detection, identification and modelling*. CRC Press, 2019.

[105] Gaetan Kerschen, Keith Worden, Alexander F Vakakis, and Jean-Claude Golinval. Past, present and future of nonlinear system identification in structural dynamics. *Mechanical systems and signal processing*, 20(3):505–592, 2006.

[106] David J Ewins. *Modal testing: theory and practice*, volume 15. Research studies press Letchworth, 1984.

[107] K Worden and G R Tomlinson. Nonlinearity in structural dynamics: detection, identification and modelling. *Inst. of Physics Publ. Bristol and Philadelphia. IOP*, 2001.

[108] G-M Lee. Estimation of non-linear system parameters using higher-order frequency response functions. *Mechanical Systems and Signal Processing*, 11(2):219–228, 1997.

[109] Tony L Schmitz, Jeremiah Couey, Eric Marsh, Nathan Mauntler, and Duke Hughes. Runout effects in milling: Surface finish, surface location error, and stability. *International Journal of Machine Tools and Manufacture*, 47(5):841–851, 2007.

[110] M Farhadmanesh and K Ahmadi. Online identification of mechanistic milling force models. *Mechanical Systems and Signal Processing*, 149:107318, 2021.

[111] Koen Engelborghs, Tatyana Luzyanina, and Dirk Roose. Numerical bifurcation analysis of delay differential equations using dde-biftool. *ACM Transactions on Mathematical Software (TOMS)*, 28(1):1–21, 2002.

[112] Keivan Ahmadi. Analytical investigation of machining chatter by considering the nonlinearity of process damping. *Journal of Sound and Vibration*, 393:252–264, 2017.

[113] Mario Bernardo, Chris Budd, Alan Richard Champneys, and Piotr Kowalczyk. *Piecewise-smooth dynamical systems: theory and applications*, volume 163. Springer Science & Business Media, 2008.

[114] E Graham, M Mehrpouya, R Nagamune, and SS Park. Robust prediction of chatter stability in micro milling comparing edge theorem and lmi. *CIRP Journal of Manufacturing Science and Technology*, 7(1):29–39, 2014.

[115] David Hajdu, Francesco Borgioli, Wim Michiels, Tamas Insperger, and Gabor Stepan. Robust stability of milling operations based on pseudospectral approach. *International Journal of Machine Tools and Manufacture*, 149:103516, 2020.

[116] Yusuf Altintas. Analytical prediction of three dimensional chatter stability in milling. *JSME International Journal Series C Mechanical Systems, Machine Elements and Manufacturing*, 44(3):717–723, 2001.

[117] Y Altintaş and Erhan Budak. Analytical prediction of stability lobes in milling. *CIRP annals*, 44(1):357–362, 1995.

[118] David J Ewins. *Modal testing: theory, practice and application*. John Wiley & Sons, 2009.

[119] Zhi-Fang Fu and Jimin He. *Modal analysis*. Elsevier, 2001.

[120] Andrew Honeycutt and Tony L Schmitz. A new metric for automated stability identification in time domain milling simulation. *Journal of Manufacturing Science and Engineering*, 138(7), 2016.

[121] David Hajdu, Tamas Insperger, and Gabor Stepan. The effect of non-symmetric frf on machining: A case study. In *International Design Engineering Technical Conferences and Computers and Information in Engineering Conference*, volume 57168, page V006T10A062. American Society of Mechanical Engineers, 2015.

[122] Yaser Mohammadi and Keivan Ahmadi. Effect of axial vibrations on regenerative chatter in robotic milling. *Procedia CIRP*, 82:503–508, 2019.

[123] Yaser Mohammadi and Keivan Ahmadi. Structural nonlinearity of robotic machining systems. In *ASME 2020 15th International Manufacturing Science and Engineering Conference*. American Society of Mechanical Engineers Digital Collection, 2020.

[124] Yaser Mohammadi and Keivan Ahmadi. Chatter in milling with robots with structural nonlinearity. *Mechanical Systems and Signal Processing*, 167:108523, 2022.

[125] Y Mohammadi and K Ahmadi. In-process frequency response function measurement for robotic milling. *Experimental Techniques*, pages 1–20, 2022.

Appendix A

Smooth Heaviside function of g_j

For a general case of milling with start and exit immersion angles of φ_{st} and φ_{ex}, respectively, the Heaviside function g_j is described as follows:

$$g_j = \begin{cases} 1 & \text{if} \quad \varphi_{st} \leqslant \varphi_{j,\,\mathrm{mod}} \leqslant \varphi_{ex} \\ 0 & \text{otherwise} \end{cases} \tag{A.1}$$

where

$$\varphi_{j,\,\mathrm{mod}} = \mathrm{mod}(\varphi_j, 2\pi) \tag{A.2}$$

In the above equations, both g_j and $\varphi_{j,\,\mathrm{mod}}$ are non-smooth and should be replaced by smooth functions. $\varphi_{j,\,\mathrm{mod}}$ can be approximated by the following smooth function:

$$\varphi_{j,\,\mathrm{mod}} = \pi - 2\tan^{-1}\left(\frac{\cos(\varphi_j/2)\sin(\varphi_j/2)}{\sin^2(\varphi_j/2)+\varepsilon_5}\right) \tag{A.3}$$

Approximating $\varphi_{j,\,\mathrm{mod}}$ using Eq. A.3 requires $\sin(\varphi_j/2)$ and $\cos(\varphi_j/2)$. Therefore, one may use $\omega = \frac{\Omega}{2}$ instead of $\omega = \Omega$ in Eq. 6.13. Then, the solution of the appended oscillator will be $y_1 = \cos\left(\frac{\omega t}{2}\right)$ and $y_2 = \sin\left(\frac{\omega t}{2}\right)$. The functions $\cos(\omega t)$ and $\sin(\omega t)$ can be calculated using trigonometric identities as follows:

$$\cos(\omega t) = 1 - 2y_2^2 \quad , \qquad \sin(\omega t) = 2y_1 y_2 \tag{A.4}$$

Equation A.1 is then approximated using the following smooth function:

$$g_j = \frac{1}{2}\tanh\left(\frac{\varphi_{\mathrm{j,mod}} - \varphi_{st}}{\varepsilon_6}\right) - \frac{1}{2}\tanh\left(\frac{\varphi_{\mathrm{j,mod}} - \varphi_{\mathrm{ex}}}{\varepsilon_6}\right) \tag{A.5}$$